

Electrochemical Dynamics and Electrokinetic Particle Motion in Concentrated Electrolytes

Submitted in partial fulfillment of the requirements for
the degree of

Doctor of Philosophy

in

Chemical Engineering

Robert F. Stout

B.S., Chemical Engineering, Purdue University

Carnegie Mellon University
Pittsburgh, PA

May 2017

© 2017 Robert F. Stout.
All rights reserved.

Acknowledgements

I'd like to thank my advisor, Aditya Khair, for his patience and persistence in helping to improve my ability as a researcher. I'd also like to thank my thesis committee, Dennis Prieve, Paul Sides, and Venkat Viswanathan.

The research presented within this thesis was funded by the following:

Chapter 2: Moderately nonlinear diffuse charge dynamics under an AC voltage

Donors of the American Chemical Society Petroleum Research Fund and NSF CAREER Award CBET-1350647

Chapter 3: Diffuse-charge dynamics in ionic thermo-electrochemical systems

NSF CAREER Award CBET-1350647

Chapter 4: A continuum approach to predicting electrophoretic mobility reversals

The Charles E. Kaufman Foundation of the Pittsburgh Foundation and NSF CAREER Award CBET-1350647

Chapter 5: Influence of ion sterics on diffusiophoresis and electrophoresis in concentrated electrolytes

NSF CAREER Award CBET-1350647

Abstract

Using the Poisson-Nernst-Planck (PNP) equations and modifications thereof, we consider two distinct systems under different conditions: an electrochemical and thermo-electric cell, and a colloidal particle in a concentrated electrolyte solution. For an electrochemical cell, we examine the response to a moderately nonlinear AC voltage and quantify the nonlinear impedance of the system, thus generalizing the concept of Electrochemical Impedance Spectroscopy beyond the low-voltage regime. With the same system, we study the response to a weak temperature gradient and quantify the charging dynamics of a model thermo-electric generator, yielding insights to the timescales over which such devices develop a thermo-voltage. We also study the electrophoresis (motion under an applied electric field) and diffusiophoresis (motion under a solute concentration gradient) of a model colloidal particle in concentrated electrolytes. In the former case, we consider the effect that direct ion-ion electrostatic interactions has on particle mobility and achieve good agreement with experiments, including prediction of a reversal in the direction of particle migration. In the latter case, we examine the effect of steric repulsion between ions and predict a significant effect on the particle mobility. Our results suggest diffusiophoresis could be a useful method for mobilizing particles in concentrated electrolytes.

Table of Contents

List of Figures and Illustrations	xi
1 Introduction	1
2 Moderately Nonlinear Diffuse-Charge Dynamics under an AC Voltage	7
2.1 Introduction	7
2.2 Mathematical Model	11
2.3 Results	20
2.4 Weakly Nonlinear Impedance	29
2.5 Conclusions	32
3 Diffuse-Charge Dynamics in Ionic Thermo-Electrochemical Systems	35
3.1 Introduction	35
3.2 Problem Formulation	38
3.3 Evolution of Charge, Salt, and Electrostatic Potential	50
3.4 Conclusions	52
4 A Continuum Approach to Predicting Electrophoretic Mobility Reversals	55
4.1 Introduction	55
4.2 Electrophoretic Mobility: Small Zeta Potentials	59

4.3	Mobility at Larger Zeta Potentials	65
4.4	Conclusions	68
5	Influence of Ion Sterics on Diffusiophoresis and Electrophoresis in Concentrated Electrolytes	71
5.1	Introduction	71
5.2	Equilibrium Diffuse Layer and Modified Electrochemical Potentials	76
5.3	Calculating Phoretic Mobility	81
5.4	Phoretic Mobility: For Varying Zeta Potential at Fixed Concentration	90
5.5	Phoretic Mobility: For Varying Concentration at Fixed Surface Charge Density	102
5.6	Conclusion	107
5.7	Appendix	111
6	Conclusion	115
	Bibliography	121

List of Figures and Illustrations

1.1	Electrochemical (a) and thermo-electric cell (b) depicting the response of charge carriers to an applied voltage and temperature gradient, respectively. A charged colloidal particle (c) in an electrolyte solution. In all three cases, a diffuse layer of charge develops near the electrodes or particle surfaces with a characteristic length scale of the Debye length, $1/\kappa$	3
2.1	Ions are initially uniformly dispersed in a dielectric liquid between two perfectly blocking electrodes. A voltage $V(t) = V_o \cos(\omega t)$ is applied across the cell and charge transport occurs normal to the electrode surface.	8
2.2	Plot of voltage amplitude in excess of thermal voltage, $\mathcal{V}_o - 1$, versus the driving frequency, ω . The solid line is the critical voltage \mathcal{V}_c for linearity predicted by (2.20) and the dotted line indicates the RC frequency. As the driving frequency increases, a larger voltage amplitude is required to yield a nonlinear response.	19

- 2.3 Total individual harmonic modes of electrostatic potential (solid line), positive ion density (dashed line), and negative ion density (dotted line) for $\omega = 0.01$, $\epsilon = 0.025$, and $t = 0$ throughout the cell. Symbols in (a)-(c) are used to show data that is hidden behind other lines; they indicate electrostatic potential (a), positive ion density (b) and (c). The odd harmonics (a), (d), and (e) are anti-symmetric about $x = 0$ and the ion densities are equal and opposite. In (a), the dimensionless negative ion density is equal to the electrostatic potential. The even harmonics (b) and (c) are symmetric and the ion densities are equal due to the symmetry of the electrolyte. An interesting result of this symmetry is that the even harmonics of the potential are uniformly zero. 21
- 2.4 Pipkin diagram for $\epsilon = 0.025$. On each plot, the horizontal axis is voltage and the vertical axis is current, both scaled to be in the range $[-1, 1]$. The solid lines are the result from our moderately nonlinear expansion and the dashed lines are numerical solutions to the PNP equations. The frequency, ω , increases to the right and the total applied voltage difference increases down. The color is based upon the linearity fraction, f , defined in equation (2.21) with two distinct regions: $f=[1, 0.9]$ the color changes from green to yellow; $f=[0.9, 0.53]$ the color changes from yellow to red and a linear theory captures relatively little of the dynamics. Also labeled on the color bar is $f = 0.77$, which is the value corresponding to $2\mathcal{V}_o = 6$ and $\omega = 0.01$ 24

- 2.5 Pipkin diagram for $\epsilon = 0.25$. The solid and dashed lines represent the moderately nonlinear calculations and the numerical solutions, respectively. The color legend is the same as in figure 2.4. Also labeled on the color bar is $f = 0.93$, which is the value corresponding to $2\mathcal{V}_o = 6$ and $\omega = 0.01$ 26
- 2.6 Dependence of current on frequency. Solid lines are linear dynamics ($\mathcal{V}_o = 0.1$), dashed lines are moderately nonlinear ($\mathcal{V}_o = 3$), and dotted lines are the applied voltage. The “double-peak” visible in (a) and the “bow-tie” in (b) are due to the third harmonic of current. This harmonic gradually loses amplitude relative to the linear contribution as frequency increases. 27
- 2.7 Total cation density for $\omega = 0.01$ and $t = 0$ at three voltages: $\mathcal{V}_o = 0.1$ (solid), $\mathcal{V}_o = 1$ (dashed), and $\mathcal{V}_o = 2$ (dotted). As the voltage increases, the ion density becomes less antisymmetric and for $\mathcal{V}_o = 2$ attains a negative value at $x = 1$ 29
- 2.8 Imaginary (a) and real (b) parts of the generalized impedance defined in (2.23) versus frequency of applied voltage for $\epsilon = 0.025$ and 0.25. The voltages plotted are $\mathcal{V}_o = 0.1$ (solid) and $\mathcal{V}_o = 3$ (dashed). 31
- 3.1 Sketch of the model problem. The initial, isothermal state is depicted in figure (a); the charges are uniformly distributed. Upon heating the an electrode to a temperature $T_H > T_0$, the charges migrate towards the colder regions of the cell, shown in figure (b). Two effects are depicted in (b): the concentration gradient and the regions of net charge near the electrodes. 39

- 3.2 Dimensionless time scales for charge density, τ_ρ (solid), salt concentration, τ_c , (dashed) at the cold electrode (the hot electrode exhibits identical timescales) as well as voltage, τ_ϕ , (dot-dashed) versus κL . For $\kappa L \ll 1$, all time scales increase with a slope of 2. However, for $\kappa L \gg 1$, the charge density and voltage time scales reach a constant value of 1/2 and 1, respectively, but the concentration time scale continues to increase at the same rate. 47
- 3.3 Salt concentration (a) and charge density (b) at the cold electrode ($x = -L$) along with the Seebeck coefficient (c), $Se(t) = -V(t)/\Delta T$, versus time at $\kappa L = 0.1, 1, 10$ and 100. Numerical Laplace transform inversion of (3.20) are shown as solid lines; dashed lines are the long time solutions (3.22). For (a), at early times, salt concentration exponentially increases until the steady-state level is reached. The time to achieve steady-state increases as κL increases since the appropriate time scale for concentration evolution is L^2/D . For (b), at early times, charge density increases but achieves progressively lower charge densities at equilibrium. For (c), the Seebeck coefficient increases at approximately the same rate at early times but achieves progressively greater values, indicating larger thermo-voltages, as κL increases. The vertical dashed line in (b) and (c) indicate the thin diffuse layer limit of the respective time scales. 48
- 3.4 Salt concentration (a), charge density (b), and electrostatic potential (c), across the cell at $tD\kappa^2 = 0.01, 0.1, 1$, and 1000 at $\kappa L = 5$. The heated electrode is located at $x/L = 1$ and the cold electrode at $x/L = -1$. At steady state ($tD\kappa^2 \approx 1000$), the neutral salt has a linear profile and the electrostatic potential is linear only in the bulk solution, away from the net charge of the diffuse layers. 51

- 4.1 Dimensionless charge density, $\tilde{\rho}$, calculated from (4.1) for a monovalent electrolyte around a negatively-charged sphere with $|\tilde{\zeta}| \lesssim 1$. Ion-ion electrostatic correlations ($\delta_c = 5$) lead to overscreening and charge oscillations. 61
- 4.2 Electrophoretic mobility, $\tilde{M}_e = 3\eta M_e / 2\varepsilon\zeta$, versus κR for various δ_c at small $\tilde{\zeta}$. Insets illustrate direction and relative magnitudes of electrical (\mathbf{F}_E), electro-osmotic (\mathbf{F}_O), and drag (\mathbf{F}_D) forces on a spherical colloid for $\tilde{M}_e > 0$ and $\tilde{M}_e < 0$ (reversals). At point (*) along the $\delta_c = 2.5$ curve, $\kappa R = 2.92$, and the mobility is close to zero, $\tilde{M}_e = 0.00020$, while the charge is of order unity $Q/4\pi R\varepsilon\zeta = 2.72$. Thus, the points of zero charge and zero mobility do not coincide. 64
- 4.3 Theoretical predictions compared with experimental data taken from figure 5a of [35] (squares). 65
- 4.4 Dimensionless charge density $\tilde{\rho}$ of a monovalent electrolyte around a negatively-charged sphere with $\kappa R = 10$ and bulk volume fraction $\nu = 0.1$. The counter-ions form an overscreening condensed layer, followed by a region of charge inversion due to co-ions. The extents of both grow with $|\tilde{\zeta}|$ 66
- 4.5 Dimensionless electrophoretic mobility, $\tilde{M}_e = \eta M_e / \varepsilon(k_B T / e)$, versus $\tilde{\zeta}$ for various δ_c with $\kappa R = 100$ and $\nu = 0.1$. Symbols are from solution of the large $\tilde{\zeta}$ model (4.7) - (4.8), and the lines are from the small $\tilde{\zeta}$ formulae (4.5)-(4.6) with $\delta_c = 0$ (top) and 2.5 (bottom). 67

- 5.1 Equilibrium ion density within the diffuse layer on a positively charged flat plate ($\zeta = 10$) for a 1 M solution of KCl. Shown are the ion densities from the Poisson-Boltzmann (PB), Bikerman (Bik), Carnahan-Starling (CS), and Boublik-Mansoori-Carnahan-Starling-Leland (BMCSL) models. The counterions increase in concentration near the surface while the coions are excluded. The Bik model achieves a saturation of counterions whereas the PB model predicts an unbounded concentration near the surface. The CS and BMCSL models predict lower concentrations of counterions but a more gradual decrease to the electroneutral bulk solution.
- (b) Equilibrium electrostatic potential within the diffuse layer. As the ion densities extend further away from the surface, so too do the electrostatic potentials. 80
- 5.2 Phoretic mobility for a 1 M solution of KCl with $\epsilon = 0.01$ for all four models of ion size: Electrophoretic mobility (a) and corresponding Dukhin number (c) versus zeta potential; diffusiophoretic mobility (b) and corresponding Dukhin number (d) versus zeta potential. Diffusiophoretic plots (b and d) assume equal diffusivities for the cation and anion, $D_+ = D_-$, leading to $\beta^{\text{id}} = 0$ 93
- 5.3 Streamlines of the electric field (a) and concentration flux (b) for electrophoresis using the PB model for $\zeta \rightarrow +\infty$ and ϵ fixed, such that $Du \rightarrow +\infty$ 95

5.4 Streamlines of concentration flux (a-c) and electric field (d-f) for diffusiophoresis using the PB model for three representative values of β^{id} as $\zeta \rightarrow +\infty$ and ϵ fixed such that $|Du| \rightarrow \infty$. The varying tangential component of the concentration flux gives rise to a surface conduction induced local electric field for all three values of β^{id} , which provides field lines along which charge can be exchanged between the diffuse layer and the electroneutral bulk. Far from the particle, away from the local electric field, the induced electric field \mathbf{E}^∞ is recovered for $\beta^{id} \neq 0$ 99

5.5 Diffusiophoretic mobility versus zeta potential for different salts using (a) PNP, (b) Bik, (c) CS, and (d) BMCSL. The salts have the following values for β^{id} : NaOH (-0.5962), NaCl (-0.2074), KCl (-0.0188), KBrO3 (0.2618), and HCl (0.6417). All concentrations are 1 M and $\epsilon = 0.01$. The dashed and solid lines are to aid readability. 100

5.6 The phoretic mobility for a colloid with constant surface charge density $\Gamma^* = 3 \mu\text{C}/\text{cm}^2$ in a solution of KCl (where $D_+ = D_-$) (a, b) and NaCl (c, d). The electrophoretic mobility (a, c) shows essentially no difference between the four models while the diffusiophoretic mobility (b, d) has significant variation at large concentrations due to the rapidly increasing induced electric field. The BMCSL model deviates in KCl (b) because it retains a non-zero β^{ex} when $D_+ = D_-$ 104

- 5.7 A colloid of constant surface charge density in a solution of NaCl. The zeta potential (a) calculated using the four models for surface charge densities of $\Gamma^* = 3$ and $6 \mu\text{C}/\text{cm}^2$. Also shown is the critical zeta potential, ζ_c ; above which ion steric effects are expected to be important. Despite slight deviation from the classic PB model result for $6 \mu\text{C}/\text{cm}^2$, all models predict zeta potentials below the critical value. The induced electric field (b) increases with increasing concentration in all models except the PB model which does not account for ion size. The rate at which the electric field increases is greater than the rate at which the zeta potential decreases. Figures (c) and (d) are for $\Gamma^* = 3\mu\text{C}/\text{cm}^2$ and $c^\infty = 2 \text{ M}$. All four models predict essentially the same structure of the diffuse layer in terms of both the equilibrium ion densities (c) and the electrostatic potential (d) despite the large concentration. 106

Chapter 1

Introduction

We apply continuum physico-chemical models, analyzed via perturbation methods, to quantify the dynamics of ions and colloidal particles in non-ideal conditions. We investigate non-idealities within two distinct systems: an electrochemical cell to study the effects of applying moderate amplitude AC voltages or a temperature gradient, and a colloidal particle in a concentrated electrolyte solution of either uniform or non-uniform concentration. Our motivation to study moderate amplitude AC voltages arises from modern microfluidic devices, such as AC electro-osmotic pumps [1, 2, 3, 4, 5], and electrochemical super capacitors [6, 7], which utilize time-dependent potentials on the order of a few volts. We were prompted to study the transient dynamics of electrolytes subjected to a temperature gradient from recent interest in thermoelectric devices with ionic charge carriers such as ionic liquids [8, 9, 10] and mixed ionic-electronic conducting polymers [11, 12, 13, 14, 15]. Finally, concentrated electrolyte solutions with salt concentrations on the order of one molar, and gradients thereof, can be encountered in enhanced oil recovery methods [16, 17], mineral replacement reactions [18], and many naturally occurring systems [18].

When an external stimulus is applied to an electrochemical system, the

charge carriers are induced to migrate from their initial distribution. This migration is referred to as electromigration when in response to an electric field [19] and thermo-migration when in response to an applied temperature gradient [20, 21]. Whatever the source of the migration, it is always balanced, at least in part, by the Brownian diffusion of the charge carriers. Thus, when ions accumulate near a surface they form a diffuse layer of charge referred to as a Debye layer, or simply diffuse layer, as depicted in figure 1.1 [19]. The characteristic length scale of the diffuse layer in dilute solution theory is the Debye length,

$$\frac{1}{\kappa} = \sqrt{\frac{\varepsilon k_B T}{2e^2 z^2 c_o}}, \quad (1.1)$$

where ε is the permittivity of the solution, k_B is Boltzmann's constant, T is absolute temperature, e is the fundamental charge, and c_o is the concentration of charge carriers at some reference point - usually an electroneutral region of the solution or initial concentration. We have assumed in (1.1) a binary, symmetric electrolyte with charge number z . As an example, an aqueous 1 mM solution of such ions at room temperature will have a Debye length $\kappa^{-1} \approx 10$ nm.

For our purposes, an ideal solution is one which can be described by the classical Poisson-Nernst-Planck (PNP) equations, a set of nonlinear, partial differential equations. These consist of Poisson's equation relating electrostatic potential to charge carrier concentration and a conservation equation governing the flux of charge carriers in the solution[19]. Ideal solutions are subject to two primary assumptions: that the charge carriers are merely point charges with no size and that they do not interact with one another. This second assumption requires that ions respond only to the mean electrostatic field generated throughout the solution, rather than local interactions between individual charges over short length scales [22, 23, 24]. Both of these conditions

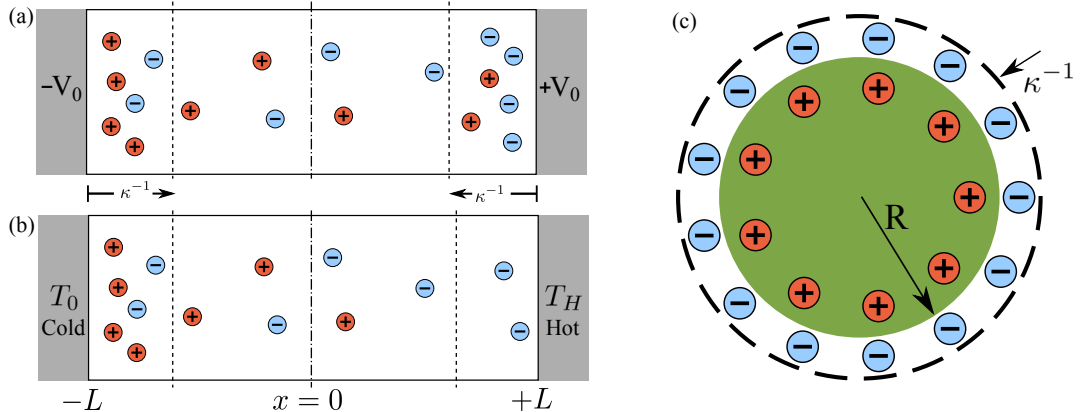


Figure 1.1: Electrochemical (a) and thermo-electric cell (b) depicting the response of charge carriers to an applied voltage and temperature gradient, respectively. A charged colloidal particle (c) in an electrolyte solution. In all three cases, a diffuse layer of charge develops near the electrodes or particle surfaces with a characteristic length scale of the Debye length, $1/\kappa$.

break down in highly concentrated solutions or regions of high concentration such as near a surface with a large potential [25, 26]. Mathematical modeling of non-ideal solutions therefore requires modifications to the PNP equations to account for these additional interactions [22, 27, 28]. In this thesis, we also consider ideal solutions subject to non-ideal conditions: moderately non-linear voltages and temperature gradients. In both of these latter scenarios, the ideal solution PNP equations can be used, but require perturbation methods to obtain detailed insights of the charge dynamics.

In chapters 2 and 3 we focus on a prototypical electrochemical cell, as depicted in figure 1.1(a) and (b), consisting of an electrolyte solution between two parallel, blocking electrodes. In chapter 2, we consider the application of a moderate amplitude AC voltage and model the charge dynamics via perturbations to the linear response in terms of the applied voltage amplitude. We show that the electrolyte response is essentially linear in voltage for frequencies greater than the RC frequency, $D\kappa/L$, where D is the charge carrier diffusivity and L is the length scale of the distance between the electrodes. At lower frequencies, the response becomes increasingly nonlinear and neutral salt

from the bulk solution is adsorbed into the diffuse layers at even orders of the voltage magnitude. We characterize the electrolyte response by extending linear Electrochemical Impedance Spectroscopy [29, 30] to moderately nonlinear voltages and find that the diffuse layer capacitance increases with increasing voltage amplitude. In contrast, the resistance of the bulk solution to current flow increases with increasing voltage due to the above mentioned adsorption of neutral salt. Perhaps the major contribution of this work is to demonstrate that a meaningful notion of electrical impedance can be constructed outside the linear-response regime of small-amplitude voltages.

Thermo-electrics are increasingly being studied as promising electrical generators in the ongoing search for alternative energy sources [14, 15, 31]; however, the majority of mathematical modeling up to this point has been focused on their steady state behavior [20, 21, 32, 33], leaving the charging dynamics largely speculative. In chapter 3, we model a prototypical ionic thermo-electric device by applying a temperature gradient to the cell depicted in figure 1.1(b). This problem is challenging in that all the physical parameters of the solution are temperature dependent. As a first approximation, we model the electrolyte response as a perturbation to the initial conditions in terms of a weak temperature gradient. Our results indicate that the steady-state thermo-voltage is achieved on the order of the Debye time, $1/D\kappa$, whereas the bulk of ion migration occurs on the order of the diffusion time, L^2/D . The Debye time is typically very short, $O(10^{-6} \mu\text{s})$ [34], which contrasts with the $O(100 - 1000 \text{ s})$ charging times reported in experiments [13, 14, 15]. This suggests that the observed charging times may not be a result of ion charging dynamics, but rather be limited by the heating rate of the electrode itself.

In chapter 4, we focus on a colloidal particle in an electrolyte solution, as depicted in figure 1.1(c). In chapter 4, we account for the electrostatic interactions between the ions as well as their finite size using modified PNP

equations. We model the electrophoresis of the particle, i.e., its motion due to an applied electric field, using asymptotic analysis to consider the experimentally relevant limit where the Debye length is small compared to the size of the particle. This work was motivated by anomalous results in concentrated solutions wherein a particle is observed to migrate in a direction opposite to that predicted by ideal solution theories [35, 36, 37, 38]. Explanations offered by previous modeling are that adsorption of ions to the particle surface as well as short range ion-ion correlations is responsible [39]. Our results, which do not account for ion adsorption, are not only capable of predicting these reversals in particle migration but agree well with experiments, indicating that ion adsorption may not be a necessary component to the observed reversals.

In chapter 5, we again consider a colloidal particle in an electrolyte solution, but rather than an electric field to drive the particle's motion, a gradient in electrolyte concentration is applied. This is referred to as diffusiophoresis and is a naturally occurring phenomenon that has earned a growing appreciation for its role in many diverse systems [18]. Diffusiophoresis is not only driven by a concentration gradient, but an electric field induced by unequal diffusion of ions down the concentration gradient [40, 41]. In our analysis, we employ three different models which account for the steric repulsion between finite sized ions, but neglect the electrostatic correlations that were the focus of chapter 4. We once again consider the limit of small Debye lengths relative to particle size and predict a large increase in the induced electric field as concentration increases, which we attribute to the non-ideality of a gradient in steric repulsion between ions. This in turn leads to an increase in the magnitude of the diffusiophoretic migration of a particle, with a fixed surface charge density, as the concentration of an asymmetric electrolyte increases. Our results, therefore, go against the common notion that phoretic motion vanishes at large electrolyte concentration. Moreover, our results suggest that

diffusiophoresis could be a useful transport mechanism for colloidal particles in concentrated electrolytes.

Most of the work within this thesis has been published in journals: chapter 2 in Physical Review E [42], chapter 4 in Journal of Fluid Mechanics [43], and chapter 5 in Physical Review Fluids [44]. Chapters 2-5 are self-contained works and can be read in isolation from the rest of the thesis. In chapter 6, we offer a concluding summary of the primary outcomes of this thesis research and suggest future extensions of this work.

Chapter 2

Moderately Nonlinear Diffuse-Charge Dynamics under an AC Voltage

2.1 Introduction

The dynamics of electrolyte solutions exposed to an applied or induced time-dependent electric potential is exploited in desalination and deionization[45, 46, 47, 48], microfluidics[49, 50, 51, 52], and the manipulation of colloidal particles[53, 54, 55, 56] and biological cells[57, 58], among other applications. The abundant historical work indicates diffuse charge dynamics of electrolytes is well understood for applied potentials below the thermal voltage, $k_B T/e$, where k_B is the Boltzmann constant, T is temperature, and e is the fundamental charge (see [59] and references therein). For reference, $k_B T/e \approx 25$ mV at $T = 298$ K. For instance, the majority of work in electrokinetics over the last century has considered fluid flow or particle motion driven by weak applied potentials, $V < k_B T/e$ [60], for which the equilibrium diffuse screening layer, or ‘Debye layer,’ around a charged surface or particle is only slightly perturbed. In contrast, modern applications such as AC, induced-charge, or second-kind, electro-osmotic pumps [1, 2, 3, 4, 5], and electrochemical supercapacitors[6, 7]

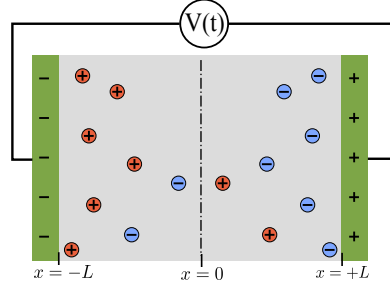


Figure 2.1: Ions are initially uniformly dispersed in a dielectric liquid between two perfectly blocking electrodes. A voltage $V(t) = V_o \cos(\omega t)$ is applied across the cell and charge transport occurs normal to the electrode surface.

use time-dependent potentials on the order of a few volts, well above the thermal voltage. The relative scarcity of theoretical treatment for such larger voltages creates a need to study diffuse charge dynamics in this regime, where the Debye layer can be driven strongly out of equilibrium.

Perhaps the simplest model system for which nonlinear diffuse charge dynamics can be analyzed is a dielectric solvent containing a symmetric, binary, monovalent electrolyte between two perfectly blocking (non-reactive) electrodes a distance $2L$ apart (figure 2.1). A voltage is applied across this electrochemical cell and the ions form Debye layers near the electrodes to screen the resulting surface charge. For the purposes of the present chapter, we take this voltage to be $V(t) = V_o \cos(\omega t)$, where V_o is the voltage amplitude, ω is the frequency, and t is time. For dilute solutions, the characteristic size of the Debye layer is given by the Debye length, $\lambda_D = \sqrt{\epsilon k_B T / 2e^2 n_0}$, where ϵ is the dielectric permittivity of the solvent and n_0 is the initial (uniform) ion number density.

The Poisson-Nernst-Planck (PNP) equations for point-sized, non-interacting ions are conventionally used to model the charge transport in this system. These equations are nonlinear and cannot be solved analytically, in general. For small voltages, $V(t) < k_B T / e$, the equations can be linearized and analytical solutions can be derived[59]. Solutions to the linearized PNP

equations are useful in electrochemical impedance spectroscopy (EIS), which is a technique used to measure electrical properties of a charge carrying system such as capacitance and conductivity[29].

EIS is primarily based on the assumption that an oscillating voltage $V(t) = V_o \cos(\omega t)$ will generate a current, $I(t)$, through an external circuit that is linear in the voltage amplitude, V_o . An impedance is then defined as $Z = V(t)/I(t)$ and will be a function of frequency only. The linearized PNP equations can be used to derive an analytical formula for the impedance[29, 30, 61]. Expressed as a complex number, the real (in-phase) part of the impedance corresponds to the resistive nature of the electrolyte via its conductivity; the complex (out-of-phase) part corresponds to the capacitive nature of the Debye layers and the dielectric solvent. At large voltages, $V_o > k_B T/e$, the diffuse charge dynamics are no longer linear; hence the current contains harmonic overtones and its amplitude is not linearly proportional to V_o [30, 61, 62, 63]. Thus, large voltages are typically avoided when measuring impedance.

A handful of works have focused on the nonlinear response of electrolytes to AC voltages. Freire *et al.* [61] numerically solved the PNP equations and showed that the electrolyte response becomes increasingly linear as ω increases, regardless of V_o . That is, as ω increases for a fixed V_o , the external current eventually loses harmonic overtones and simply oscillates with the frequency of the driving voltage. Olesen *et al.*[63] examined the long-time periodic response to a voltage oscillating near the RC frequency, $\omega \approx D/\lambda_D L$, where D is the diffusivity of the ions. They solved the PNP equations numerically and also performed asymptotic analysis in the thin-Debye-layer limit $\lambda_D/L \rightarrow 0$. They define a “weakly-nonlinear” regime where the electroneutral bulk electrolyte (outside the Debye layers) retains a uniform “neutral salt” concentration (total ion concentration), and the nonlinear response is driven solely by the nonlinear

capacitance of the Debye layers. Schnitzer and Yariv[62] derived an asymptotic current-voltage relationship for this regime as $V_o \rightarrow \infty$. Olesen *et al.*[63] also analyzed “strongly-nonlinear” response at very large voltages. Here, there is significant ion depletion adjacent to the Debye layers, which leads to “AC capacitive desalination” as a net flux of salt is transferred from the bulk to the Debye layer during an oscillation period. Furthermore, at such large voltages the Debye layers can attain a non-equilibrium structure, characterized by the periodic growth and shrinkage of transient space-charge layers.

In this work, we consider electrolyte dynamics under an AC field with amplitude $V_o \sim 1 - 10k_B T/e$, at arbitrary Debye layer thickness λ_D/L and across a wide range of frequencies ω . We refer to this as the “moderately nonlinear” regime of diffuse charge dynamics, to distinguish our work from the articles mentioned above. Notably, the thin-Debye-layer limit $\lambda_D/L \ll 1$ is commonly assumed in mathematical analysis of electrolyte dynamics. However, this can be violated in nano-scale electrochemical systems, where the electrode separation L approaches the Debye length λ_D : e.g., in nanometer wide thin-layer cells used to probe fast electron-transfer kinetics [64]. We use a complex Fourier series to decompose the electrolyte dynamics into its component harmonics and a perturbation expansion in voltage for the Fourier coefficients. A similar approach was recently utilized by Bandopadhyay *et al.*[65]; however, their expansion stopped at $O(V_o^2)$. We proceed to $O(V_o^3)$, which is necessary to predict a nonlinear current response for a symmetric, binary electrolyte. We also derive a first approximation to a voltage dependent impedance that is $O(V_o^2)$.

The chapter is organized as follows: in section 2.2 we present the mathematical model to calculate the moderately nonlinear dynamics. In section 2.3, we present the results for the ion dynamics and external current. In section 2.4, we calculate a voltage-dependent “impedance” as the current first

becomes nonlinear in V_o . Conclusions are offered in section 2.5.

2.2 Mathematical Model

We consider the prototypical situation (figure 1) of two parallel, perfectly blocking electrodes separated by a dielectric solvent containing an ideal solution of monovalent, point-like charge carriers. We assume that the electrodes are spaced sufficiently close such that the charge transport persists perpendicular to the electrode surface. The one dimensional PNP equations are

$$\varepsilon \frac{\partial^2 \phi}{\partial x^2} = -\rho = -e(n_+ - n_-), \quad (2.1a)$$

$$\frac{\partial n_r}{\partial t} = -\frac{\partial j_r}{\partial x} = D \left[\frac{\partial^2 n_r}{\partial x^2} + r \frac{e}{k_B T} \frac{\partial}{\partial x} \left(n_r \frac{\partial \phi}{\partial x} \right) \right]. \quad (2.1b)$$

Equation (2.1a) is Poisson's equation describing the electrostatic potential, ϕ , in response to the ionic charge density, ρ , which undergoes changes in time and space according to the ion flux balance (2.1b), where n_r is the ion number density of cations ($r = +$) and anions ($r = -$), t is time, x is the position across the cell, and j_r is the ion flux.

We supplement the governing equations with the following boundary conditions:

$$\phi(x = \pm L, t) = \pm V_o \cos(\omega t), \quad (2.2a)$$

$$j_r(x = \pm L, t) = -D \left[\frac{\partial n_r}{\partial x} + r \frac{e}{k_B T} n_r \frac{\partial \phi}{\partial x} \right]_{\pm L} = 0, \quad (2.2b)$$

specifying that the electrode surface potential is equal to the applied potential (2.2a) and no ion flux through the electrodes (2.2b). By using these boundary conditions, we seek to find the steady periodic response as opposed to suddenly applying an AC voltage to a previously unaffected system. Note that from (2.2a), the total applied potential across the cell is $2V_o$.

We non-dimensionalize as follows: position (x) with half the cell width (L), electrostatic potential (ϕ) with thermal voltage ($k_B T/e$), ion density (n_r) with the uniform ion density (of a single species) prior to the application of a voltage (n_0), time (t) with the RC time for Debye layer charging ($\lambda_D L/D$)[59], and frequency (ω) with the RC frequency. The non-dimensional governing equations are then

$$\frac{\partial^2 \phi}{\partial x^2} = -\frac{n_+ - n_-}{2\epsilon^2}, \quad (2.3a)$$

$$\frac{\partial n_r}{\partial t} = \epsilon \left[\frac{\partial^2 n_r}{\partial x^2} + r \frac{\partial}{\partial x} \left(n_r \frac{\partial \phi}{\partial x} \right) \right], \quad (2.3b)$$

where $\epsilon = \lambda_D/L$ and all quantities in (2.3) and onward, unless stated otherwise, are dimensionless. The corresponding non-dimensional boundary conditions are

$$\phi(x = \pm 1, t) = \pm \mathcal{V}_o \cos(\omega t), \quad (2.4a)$$

$$\left[\frac{\partial n_r}{\partial x} + r n_r \frac{\partial \phi}{\partial x} \right]_{\pm 1} = 0, \quad (2.4b)$$

where $\mathcal{V}_o = V_o/(k_B T/e)$ is the dimensionless applied voltage amplitude.

For small amplitude voltages, $\mathcal{V}_o < 1$, it is typical to express ϕ and n_r as complex valued functions of ω that depend linearly on \mathcal{V}_o :

$$\phi(x, t) = \phi_0^{(0)} + \mathcal{V}_o \phi_1^{(1)}(x) e^{i\omega t}, \quad (2.5a)$$

$$n_r(x, t) = n_0^{(0)} + \mathcal{V}_o n_{r,1}^{(1)}(x) e^{i\omega t}, \quad (2.5b)$$

where $\mathcal{V}_o \phi_1^{(1)}$ and $\mathcal{V}_o n_{r,1}^{(1)}$ are complex valued $O(\mathcal{V}_o)$ perturbations. Here, we assume that the electrodes do not carry a “native” surface charge; hence, the equilibrium potential is $\phi_0^{(0)} = 0$, and the equilibrium ion density is uniform, $n_0^{(0)} = 1$. In (2.5), the notation is that the numerical subscripts and parenthetic superscripts indicate to which harmonic and which order of voltage the quantity corresponds, respectively. The harmonics in (2.5) are 0 - steady and

1 - first, or fundamental. While this is evident in (2.5) we explicitly state it here to be consistent with later notation.

This approach works because at $O(\mathcal{V}_o)$ the nonlinear term in (2.3b) degenerates to a coupling of $\mathcal{V}_o\phi_1^{(1)}$ with $n_0^{(0)}$ and oscillates at $e^{i\omega t}$. More specifically, as long as $O(\mathcal{V}_o^2)$ terms can be neglected, there is no multiplication of complex functions and only terms oscillating at $e^{i\omega t}$ will be present. Here, the real part is the physically meaningful portion since the applied voltage is $\mathcal{V}_o \cos(\omega t)$. When $O(\mathcal{V}_o^2)$ terms cannot be neglected, the coupling of complex functions (e.g., $\phi_1^{(1)}e^{i\omega t}$ and $n_{r,1}^{(1)}e^{i\omega t}$) manifests as additional harmonic modes in the electrolyte response.

At $O(\mathcal{V}_o)$, the fundamental mode (first harmonic) dominates the overall response but as \mathcal{V}_o increases, the higher order harmonics need to be taken into account. The solution for this oscillating system can therefore be written as a Fourier series, which for $g(x, t) = \phi(x, t)$ or $n_r(x, t)$ is

$$g(x, t) = a_0(x) + \sum_{k=1}^{\infty} a_k(x) \cos(k\omega t) + b_k(x) \sin(k\omega t), \quad (2.6)$$

where a_k and b_k are real functions of ω . Here, a_0 is just the stationary ($k = 0$) contribution. Equation (2.6) can be rewritten using complex functions via Euler's formula, $e^{iz} = \cos(z) + i\sin(z)$. The result is a complex Fourier series,

$$g(x, t) = a_0(x) + \sum_{k=1}^{\infty} A_k(x)e^{ki\omega t} + B_k(x)e^{-ki\omega t}, \quad (2.7)$$

where $A_k = (a_k - ib_k)/2$ and $B_k = (a_k + ib_k)/2$ are complex conjugates. Note that the sum in (2.7) is of complex conjugates and is therefore real valued.

Thus, we can express the solutions to (2.3) as

$$\phi(x, t) = \phi_0(x) + \sum_{k=1}^{\infty} \phi_k(x)e^{ki\omega t} + \phi_{-k}(x)e^{-ki\omega t}, \quad (2.8a)$$

$$n_r(x, t) = n_{r,0}(x) + \sum_{k=1}^{\infty} n_{r,k}(x)e^{ki\omega t} + n_{r,-k}(x)e^{-ki\omega t}, \quad (2.8b)$$

where the “coefficients”, ϕ_k and $n_{r,k}$, are complex valued functions of ω while ϕ_0 and $n_{r,0}$ are real valued. A negative subscript ($-k$) denotes the complex conjugate of the corresponding positive subscript (k), and the dependence on \mathcal{V}_o is implicit in the coefficients.

Substitution of (2.8) into (2.3) yields an infinite set of coupled nonlinear ordinary differential equations. Without giving the full expression, we can address the primary difficulty of the resulting set of equations. The nonlinear term in (2.3b) ($n_r \partial \phi / \partial x$) results in doubly infinite sums through the coupling of terms containing $e^{ki\omega t}$ with $e^{-qi\omega t}$ where k and q are any positive integers. The result is terms which look like

$$\sum_{k=1}^{\infty} \sum_{q=1}^{\infty} n_{r,k+q} \phi_{-q} e^{ki\omega t} + \sum_{q=1}^{\infty} n_{r,q} \phi_{-q}, \quad (2.9)$$

for example. This arises due to the fact that there are an infinite number of positive integers k and q such that $(k+q) - q = k$ and $q + (-q) = 0$. Hence, the k^{th} harmonic is dependent upon *all* other harmonic modes q , even those for which $q > k$. The series must therefore be truncated at a suitable harmonic. We can alleviate ourselves of the doubly infinite sums by expressing the Fourier coefficients ϕ_k and $n_{r,k}$ as power series in \mathcal{V}_o . We give the form of the power series later but it is instructive to first demonstrate how it arises from the nonlinearity of (2.3b).

First, ϕ_k and $n_{r,k}$ contain a linear dependence on \mathcal{V}_o from (2.5) which we denote as $\phi_1^{(1)}$ and $n_{r,1}^{(1)}$. Recall that a parenthetic superscript indicates the order of \mathcal{V}_o the quantity applies to. The coupling of $\mathcal{V}_o n_{r,1}^{(1)} e^{i\omega t}$ with $\mathcal{V}_o \phi_1^{(1)} e^{i\omega t}$ produces terms which are $O(\mathcal{V}_o^2)$ and oscillate at the second harmonic, $e^{2i\omega t}$. We also obtain the corresponding complex conjugates. Furthermore, the coupling of $\mathcal{V}_o n_{r,1}^{(1)} e^{i\omega t}$ with $\mathcal{V}_o \phi_{-1}^{(1)} e^{-i\omega t}$ also results in $O(\mathcal{V}_o^2)$ terms but they are non-oscillatory, or stationary. The $O(\mathcal{V}_o^2)$ terms for ϕ (and similarly for n_r) are thus $\mathcal{V}_o^2 \phi_2^{(2)} e^{2i\omega t}$, $\mathcal{V}_o^2 \phi_{-2}^{(2)} e^{-2i\omega t}$, and $\mathcal{V}_o^2 \phi_0^{(2)}$. These terms are coupled to other

$O(\mathcal{V}_o^2)$ terms but also to $O(\mathcal{V}_o)$ and $O(1)$ terms. Coupling with $O(\mathcal{V}_o)$ yields terms which are $O(\mathcal{V}_o^3)$ and oscillate at $e^{3i\omega t}$ and $e^{i\omega t}$ (through coupling with a term oscillating at $e^{-i\omega t}$). As we show later, $O(\mathcal{V}_o^3)$ is the first nonlinear contribution to the current. Thus, we truncate our series here and write the expansions as

$$\begin{aligned} \phi(x, t) = & \mathcal{V}_o \left(\phi_1^{(1)} e^{i\omega t} + \phi_{-1}^{(1)} e^{-i\omega t} \right) + \mathcal{V}_o^2 \left(\phi_2^{(2)} e^{2i\omega t} + \phi_0^{(2)} + \phi_{-2}^{(2)} e^{-2i\omega t} \right) \\ & + \mathcal{V}_o^3 \left(\phi_3^{(3)} e^{3i\omega t} + \phi_1^{(3)} e^{i\omega t} + \phi_{-1}^{(3)} e^{-i\omega t} + \phi_{-3}^{(3)} e^{-3i\omega t} \right) + O(\mathcal{V}_o^4), \end{aligned} \quad (2.10a)$$

and

$$\begin{aligned} n_r(x, t) = & n_{r,0}^{(0)} + \mathcal{V}_o \left(n_{r,1}^{(1)} e^{i\omega t} + n_{r,-1}^{(1)} e^{-i\omega t} \right) + \mathcal{V}_o^2 \left(n_{r,2}^{(2)} e^{2i\omega t} + n_{r,0}^{(2)} + n_{r,-2}^{(2)} e^{-2i\omega t} \right) \\ & + \mathcal{V}_o^3 \left(n_{r,3}^{(3)} e^{3i\omega t} + n_{r,1}^{(3)} e^{i\omega t} + n_{r,-1}^{(3)} e^{-i\omega t} + n_{r,-3}^{(3)} e^{-3i\omega t} \right) + O(\mathcal{V}_o^4), \end{aligned} \quad (2.10b)$$

which can be rearranged to show how the Fourier coefficients in (2.8) depend on voltage. For example, for the potential from (2.10a),

$$\phi_0(x) = \mathcal{V}_o^0 \phi_0^{(0)} + \mathcal{V}_o^2 \phi_0^{(2)} + \mathcal{V}_o^4 \phi_0^{(4)} + \dots, \quad (2.11a)$$

$$\phi_1(x) = \mathcal{V}_o \phi_1^{(1)} + \mathcal{V}_o^3 \phi_1^{(3)} + \mathcal{V}_o^5 \phi_1^{(5)} + \dots, \quad (2.11b)$$

$$\phi_2(x) = \mathcal{V}_o^2 \phi_2^{(2)} + \mathcal{V}_o^4 \phi_2^{(4)} + \mathcal{V}_o^6 \phi_2^{(6)} + \dots, \quad (2.11c)$$

etc, where $\phi_0^{(0)} = 0$. The power series can more generally be written as

$$\phi_k(x) = \sum_{v=0}^{\infty} \phi_k^{(2v+k)}(x) \mathcal{V}_o^{2v+k}, \quad (2.12a)$$

$$\phi_{-k}(x) = \sum_{v=0}^{\infty} \phi_{-k}^{(2v+k)}(x) \mathcal{V}_o^{2v+k}, \quad (2.12b)$$

and an analogous series for the ion densities, $n_{r,\pm k}$. The moderately nonlinear expansions (2.10) can be written concisely as

$$\phi(x, t) = \phi_0^{(0)} + \sum_{v=1}^{\infty} \mathcal{V}_o^v \left(\sum_{l=0}^v \phi_{v-2l}^{(v)} e^{(v-2l)i\omega t} \right), \quad (2.13a)$$

$$n_r(x, t) = n_{r,0}^{(0)} + \sum_{v=1}^{\infty} \mathcal{V}_o^v \left(\sum_{l=0}^v n_{r,v-2l}^{(v)} e^{(v-2l)i\omega t} \right). \quad (2.13b)$$

From the pattern in (2.10), or equivalently the series in (2.13), it is apparent that the odd orders of voltage contain only odd harmonics while the even orders of voltage contain only even harmonics. Note that the sums in (2.10) are all real valued since a complex quantity is always present with its complex conjugate. Also, note that the stationary terms are always real valued quantities.

Substitution of (2.13) into (2.3) yields a set of *linear* differential equations. We present here the explicit statements of the governing equations up to $O(\mathcal{V}_o^3)$ for $e^{ki\omega t}$, where $k \geq 0$. The equations for $k < 0$ are obtained by taking the complex conjugate. The resulting $O(\mathcal{V}_o)$ equations for $e^{i\omega t}$ are

$$\frac{d^2\phi_1^{(1)}}{dx^2} = -\frac{n_{+,1}^{(1)} - n_{-,1}^{(1)}}{2\epsilon^2}, \quad (2.14a)$$

$$\frac{d^2n_{r,1}^{(1)}}{dx^2} = \frac{i\omega}{\epsilon}n_{r,1}^{(1)} - r \left[n_0^{(0)} \frac{d^2\phi_1^{(1)}}{dx^2} \right], \quad (2.14b)$$

$$\frac{dn_{r,1}^{(1)}}{dx} + r \left[n_0^{(0)} \frac{d\phi_1^{(1)}}{dx} \right] = 0, \text{ at } x = \pm 1 \quad (2.14c)$$

$$\phi_1^{(1)} = \pm \frac{1}{2}, \text{ at } x = \pm 1. \quad (2.14d)$$

The $O(\mathcal{V}_o^2)$ equations have $e^{2i\omega t}$ and stationary contributions. The $e^{2i\omega t}$ equations are

$$\frac{d^2\phi_2^{(2)}}{dx^2} = -\frac{n_{+,2}^{(2)} - n_{-,2}^{(2)}}{2\epsilon^2}, \quad (2.15a)$$

$$\frac{d^2n_{r,2}^{(2)}}{dx^2} = \frac{2i\omega}{\epsilon}n_{r,2}^{(2)} - r \frac{d}{dx} \left[n_0^{(0)} \frac{d\phi_2^{(2)}}{dx} + F_{r,2}^{(2)} \right], \quad (2.15b)$$

$$\frac{dn_{r,2}^{(2)}}{dx} + r \left[n_0^{(0)} \frac{d\phi_2^{(2)}}{dx} + F_{r,2}^{(2)} \right] = 0, \text{ at } x = \pm 1, \quad (2.15c)$$

$$\phi_2^{(2)} = 0, \text{ at } x = \pm 1, \quad (2.15d)$$

which are forced by,

$$F_{r,2}^{(2)} = n_{r,1}^{(1)} \frac{d\phi_1^{(1)}}{dx}. \quad (2.15e)$$

The stationary equations are

$$\frac{d^2\phi_0^{(2)}}{dx^2} = -\frac{n_{+,0}^{(2)} - n_{-,0}^{(2)}}{2\epsilon^2}, \quad (2.16a)$$

$$\frac{d^2n_{r,0}^{(2)}}{dx^2} = -r \frac{d}{dx} \left[n_0^{(0)} \frac{d\phi_0^{(2)}}{dx} + F_{r,0}^{(2)} \right], \quad (2.16b)$$

$$\frac{dn_{r,0}^{(2)}}{dx} + r \left[n_0^{(0)} \frac{d\phi_0^{(2)}}{dx} + F_{r,0}^{(2)} \right] = 0, \text{ at } x = \pm 1, \quad (2.16c)$$

$$\phi_0^{(2)} = 0, \text{ at } x = \pm 1, \quad (2.16d)$$

which are forced by,

$$F_{r,0}^{(2)} = n_{r,1}^{(1)} \frac{d\phi_{-1}^{(1)}}{dx} + n_{r,-1}^{(1)} \frac{d\phi_1^{(1)}}{dx}. \quad (2.16e)$$

The $O(\mathcal{V}_o^3)$ equations contain both $e^{3i\omega t}$ and $e^{i\omega t}$ contributions. The $e^{3i\omega t}$ equations are

$$\frac{d^2\phi_3^{(3)}}{dx^2} = -\frac{n_{+,3}^{(3)} - n_{-,3}^{(3)}}{2\epsilon^2}, \quad (2.17a)$$

$$\frac{d^2n_{r,3}^{(3)}}{dx^2} = \frac{3i\omega}{\epsilon} n_{r,3}^{(3)} - r \frac{d}{dx} \left[n_0^{(0)} \frac{d\phi_3^{(3)}}{dx} + F_{r,3}^{(3)} \right], \quad (2.17b)$$

$$\frac{dn_{r,3}^{(3)}}{dx} + r \left[n_0^{(0)} \frac{d\phi_3^{(3)}}{dx} + F_{r,3}^{(3)} \right] = 0, \text{ at } x = \pm 1, \quad (2.17c)$$

$$\phi_3^{(3)} = 0, \text{ at } x = \pm 1, \quad (2.17d)$$

which are forced by,

$$F_{r,3}^{(3)} = n_{r,1}^{(1)} \frac{d\phi_2^{(2)}}{dx} + n_{r,2}^{(2)} \frac{d\phi_1^{(1)}}{dx}, \quad (2.17e)$$

and the $e^{i\omega t}$ equations are

$$\frac{d^2\phi_1^{(3)}}{dx^2} = -\frac{n_{+,1}^3 - n_{-,1}^3}{2\epsilon^2}, \quad (2.18a)$$

$$\frac{d^2n_{r,1}^3}{dx^2} = \frac{i\omega}{\epsilon} n_{r,1}^{(3)} - r \frac{d}{dx} \left[n_0^{(0)} \frac{d\phi_1^{(3)}}{dx} + F_{r,1}^{(3)} \right], \quad (2.18b)$$

$$\frac{dn_{r,1}^{(3)}}{dx} + r \left[n_0^{(0)} \frac{d\phi_1^{(3)}}{dx} + F_{r,1}^{(3)} \right] = 0, \text{ at } x = \pm 1, \quad (2.18c)$$

$$\phi_1^{(3)} = 0, \text{ at } x = \pm 1, \quad (2.18d)$$

which are forced by,

$$F_{r,1}^{(3)} = n_{r,1}^{(1)} \frac{d\phi_0^{(2)}}{dx} + n_{r,-1}^{(1)} \frac{d\phi_2^{(2)}}{dx} + n_{r,2}^{(2)} \frac{d\phi_{-1}^{(1)}}{dx} + n_{r,0}^{(2)} \frac{d\phi_1^{(1)}}{dx}. \quad (2.18e)$$

The stationary $O(\mathcal{V}_o^2)$ equations (2.16) pose an issue in that the governing equations (2.16b) are the derivatives of the boundary conditions (2.16c). Thus one of the boundary conditions (2.16c) are redundant. We can resolve this issue by recognizing that since there is no flux of ions at the boundaries, the total number of ions in the cell must be constant. This means that the integral of each perturbation to the ion density must be zero: $\int_{-1}^1 n_{r,k}^{(v)} dx = 0$, for $v > 0$. Using this condition, it is possible to derive a new set of governing equations for the stationary $O(\mathcal{V}_o^2)$ terms:

$$\epsilon^2 \frac{d^2 \phi_0^{(2)}}{dx^2} = \phi_0^{(2)} + \frac{1}{2}(\mathcal{I}_+ + \mathcal{I}_-) - \frac{1}{2} \int_{-1}^1 \phi_0^{(2)} dx - \frac{1}{4} \int_{-1}^1 (\mathcal{I}_+ + \mathcal{I}_-) dx, \quad (2.19a)$$

$$n_{r,0}^{(2)} = -r\phi_0^{(2)} - r\mathcal{I}_r + r\frac{1}{2} \int_{-1}^1 \phi_0^{(2)} dx + r\frac{1}{2} \int_{-1}^1 \mathcal{I}_r dx, \quad (2.19b)$$

where,

$$\mathcal{I}_r = \int_{-1}^x F_{r,0}^{(2)} d\bar{x}, \quad (2.19c)$$

This set of equations has thus been reduced to a single integro-differential equation (2.19a) for $\phi_0^{(2)}$. Once (2.19a) is solved, $n_{r,0}^{(2)}$ is easily computed from $\phi_0^{(2)}$.

Thus far we have claimed that the electrolyte dynamics are linear so long as $\mathcal{V}_o < 1$, while for $\mathcal{V}_o > 1$ the response is voltage dependent. This is not precisely the case, though $\mathcal{V}_o < 1$ does ensure linearity. We can obtain a useful frequency-dependent criteria for linearity by considering the linear ion density perturbation $\mathcal{V}_o n_{r,1}^{(1)}$ from (2.5). When $\mathcal{V}_o |n_{r,1}^{(1)}| \ll n_0^{(0)}$, the nonlinear term in (2.3b) can be linearized since $n_r \approx n_0^{(0)}$. Physically, this means that the extent of the ion motion is sufficiently small that the perturbation to the

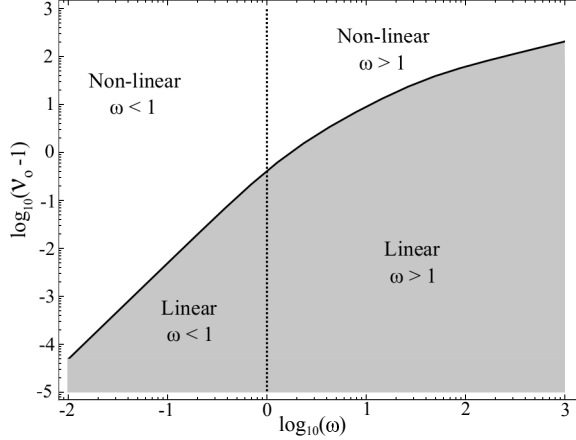


Figure 2.2: Plot of voltage amplitude in excess of thermal voltage, $\mathcal{V}_o - 1$, versus the driving frequency, ω . The solid line is the critical voltage \mathcal{V}_c for linearity predicted by (2.20) and the dotted line indicates the RC frequency. As the driving frequency increases, a larger voltage amplitude is required to yield a nonlinear response.

equilibrium distribution is negligible. From the analytic solutions obtained by substitution of (2.5) into (2.3), it can be shown that the above inequality is satisfied when[61]

$$\mathcal{V}_o \ll \mathcal{V}_c = \left| \frac{1}{\beta^2} + \frac{i\omega}{\beta} \coth\left(\frac{\beta}{\epsilon}\right) \right|, \quad (2.20)$$

where $\beta = \sqrt{1 + i\omega\epsilon}$. This gives a frequency-voltage relationship for linearity where, for a given ω , the ion perturbation is small if \mathcal{V}_o is less than the critical voltage, \mathcal{V}_c .

Figure 2.2 is a plot of the dimensionless applied voltage in excess of the thermal voltage, $\mathcal{V}_o - 1$, against ω with the linear and nonlinear regions separated by the solid line created by \mathcal{V}_c . The vertical dotted line separates the plot into frequencies above or below the RC frequency. It is clear that $\mathcal{V}_o \leq 1$ always results in a linear response, and as frequency increases, the voltage needed to observe nonlinear effects increases.

The physical effect of increasing frequency can be understood in terms of ion motion. At low frequencies, the ions have time to move in response to the applied voltage and begin to form Debye layers at the electrode surfaces. The

developing Debye layers are what ultimately give rise to the nonlinearities in the charge dynamics. As the frequency increases, the ions are only able to move a short distance before the voltage has reversed and they must move in the opposite direction, precluding the formation of Debye layers. Therefore, although there is a greater driving force at large \mathcal{V}_o , there exists a frequency beyond which the dynamics will be linear in \mathcal{V}_o .

Equations (2.14), (2.15), and (2.17)-(2.19) were solved using the MATLAB `bvp4c` solver. It is a finite difference scheme utilizing the three stage Lobatto 3a collocation method.

2.3 Results

2.3.1 Harmonic Profiles

We begin with general observations regarding the electrostatic potential and ion densities that will aid subsequent analysis. First, at $O(\mathcal{V}_o)$ and $O(\mathcal{V}_o^3)$, the ion densities are equal and opposite (e.g. $n_{+,1}^{(1)} = -n_{-,1}^{(1)}$) (figure 2.3a and 2.3e). This is not surprising since the electrolyte is symmetric with equal ionic diffusivities. A consequence of this behavior is that the ion densities for odd orders of voltage are anti-symmetric about $x = 0$.

The second, more interesting, observation is that the ion densities and electrostatic potential for $O(\mathcal{V}_o^2)$ are not only symmetric, but also $\phi_2^{(2)} = \phi_0^{(2)} = 0$, $n_{+,2}^{(2)} = n_{-,2}^{(2)}$, and $n_{+,0}^{(2)} = n_{-,0}^{(2)}$ (figure 2.3b and 2.3c). At this order, the voltage on the electrode is “squared” which leads to an identical charge on each and no electric field in the electrolyte. However, the ions still migrate due to the electromigrative forcing originating from the $O(\mathcal{V}_o)$ dynamics, $F_{r,2}^{(2)} = n_{r,1}^{(1)} d\phi_1^{(1)} / dx$. This symmetric motion corresponds to the adsorption of neutral salt (total ion concentration) leading to a depletion of neutral salt in the bulk

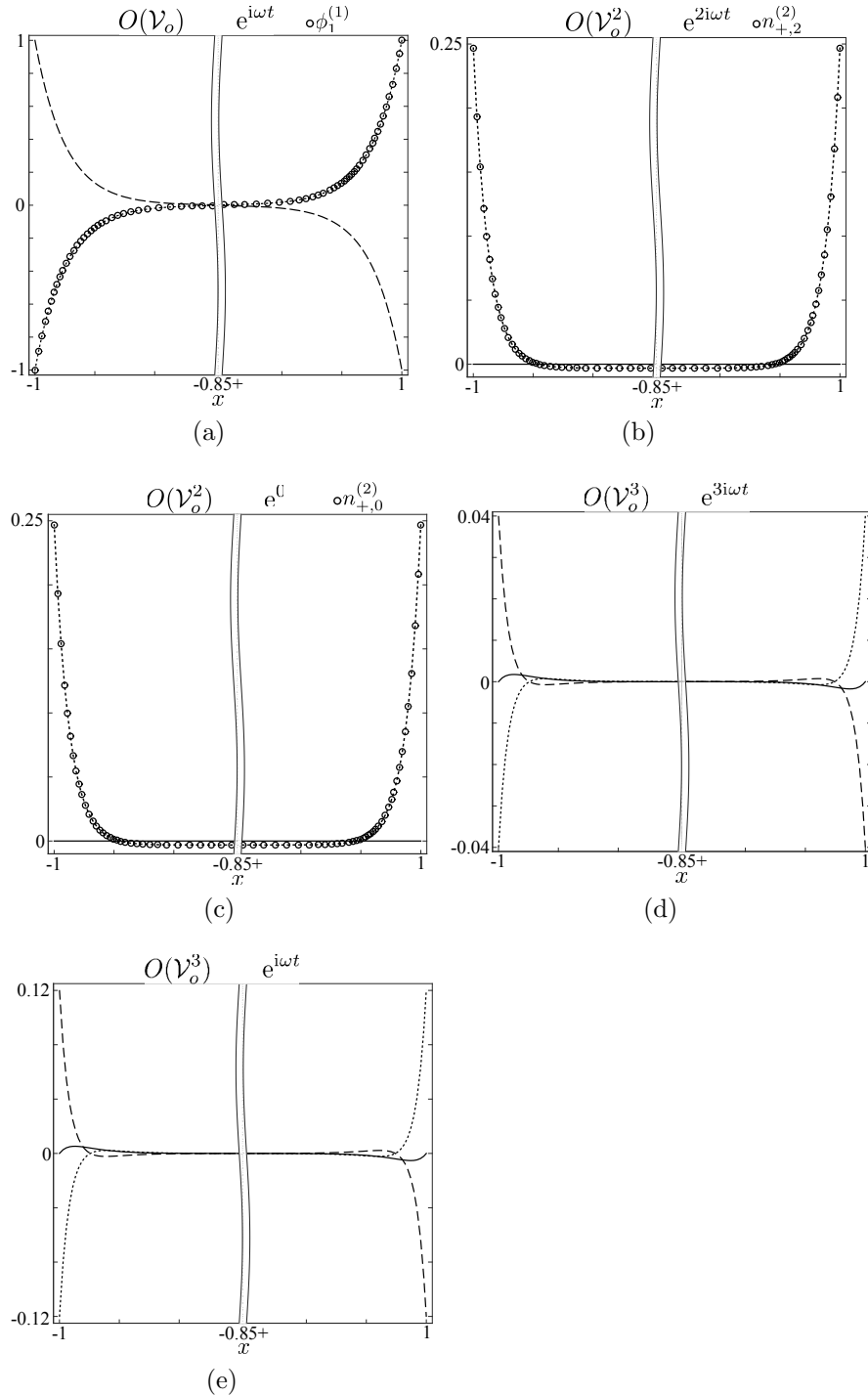


Figure 2.3: Total individual harmonic modes of electrostatic potential (solid line), positive ion density (dashed line), and negative ion density (dotted line) for $\omega = 0.01$, $\epsilon = 0.025$, and $t = 0$ throughout the cell. Symbols in (a)-(c) are used to show data that is hidden behind other lines; they indicate electrostatic potential (a), positive ion density (b) and (c). The odd harmonics (a), (d), and (e) are anti-symmetric about $x = 0$ and the ion densities are equal and opposite. In (a), the dimensionless negative ion density is equal to the electrostatic potential. The even harmonics (b) and (c) are symmetric and the ion densities are equal due to the symmetry of the electrolyte. An interesting result of this symmetry is that the even harmonics of the potential are uniformly zero.

electrolyte as can be seen in figures 2.3b and 2.3c.

Olesen *et al.* [63] predicted this adsorption of salt in the context of a “strongly nonlinear” regime in which oscillating diffusion layers could almost completely deplete the salt concentration outside the Debye layers. They referred to this effect as “AC capacitive desalination.” Remarkably, they showed that despite the oscillatory nature of the driving voltage, there is a time-averaged salt adsorption into the Debye layers. We demonstrate that this “steady” desalination of the bulk electrolyte also occurs at moderately large voltages. Our analysis indicates neutral salt adsorption occurs first at $O(\mathcal{V}_o^2)$ and, in general, at all even orders of voltage.

2.3.2 Nonlinear Current

We now calculate the overall current through the system, $I(t) = dQ/dt$, where Q is the total charge on the electrode surface normalized by $A\epsilon k_B T/eL$, where A is the surface area of the electrode in contact with electrolyte. Using Gauss’s law, $I(t)$ can be related to ϕ , and the dimensionless current (normalized by $A\epsilon D k_B T/e\lambda_D L^2$) is $I(t) = -\partial^2 \phi / \partial x \partial t|_{x=-1}$ [19]. The current can be expanded in the same form as (2.10) where it is clear from the above explanation that the $O(\mathcal{V}_o^2)$ contribution is zero since $\phi_k^{(2)} = 0$. In fact, the stationary term $\phi_0^{(2)}$ cannot contribute to the current regardless of electrolyte symmetry since it lacks a time dependent co-factor (see (2.10)). More generally, for a symmetric electrolyte, all even orders of voltage will have zero electrostatic potential and be non-contributing to the overall current.

The relationship between current and voltage can be visualized from a Lissajous plot, which is a parametric mapping of current versus voltage, each normalized by their respective maximums. The more closely the resulting curve resembles a line, the more in-phase the current and voltage are. Like-

wise, a perfectly out-of-phase (but linear in \mathcal{V}_o) current results in a circular curve. Physically, the out-of-phase circular curves are achieved through the capacitance of either the Debye layers ($\omega \ll 1$) or the dielectric solvent ($\omega \gg 1$) and the most in-phase curves represent a relative balance between conduction of ions and capacitive charging ($\omega \sim 1$).

Using the idea of Pipkin diagrams from rheology[66], we make a colored diagram of Lissajous plots for a range of voltages and frequencies (figure 2.4 for $\epsilon = 0.025$ and figure 2.5 for $\epsilon = 0.25$). The axes on each individual Lissajous plot range from -1 to 1 while the axes values for the total diagram are explicitly labeled. The solid and dashed lines are results from our moderately nonlinear expansion (2.10) and, for comparison, a full numerical solution to the PNP equations, respectively. (Numerical solution obtained using a finite difference method via the MATLAB `pdepe` solver.) The color is a visual measure of the linearity of the response:

$$f = \left[\frac{\int_0^{T/2} (I^{(1)})^2 dt}{\int_0^{T/2} (I^{(1)} + \mathcal{V}_o^2 I^{(3)})^2 dt} \right]^{1/2}, \quad (2.21)$$

where $T = 2\pi/\omega$ is the period of oscillation. For values of f between 1 and 0.9, the color linearly changes from green ($f = 1$) to yellow ($f = 0.9$). For f between 0.9 and 0.53 (the lowest value calculated), the color linearly changes from yellow to red. This is also shown in the color bar legend. In figure 2.4, the minimum value is $f = 0.53$. Including higher order terms in voltage and frequency would likely reduce this value further so it is a conservative measure of linearity.

Most apparent from figure 2.4 is that the responses which are most nonlinear are those at high voltages and low frequencies. This is not surprising given the relationship between ω and \mathcal{V}_o in (2.20) for linear response (see also figure 2.2). What is notable about figure 2.4 is it suggests the current response is essentially linear for $\omega > 1$. This could allow use of linearizing approxima-

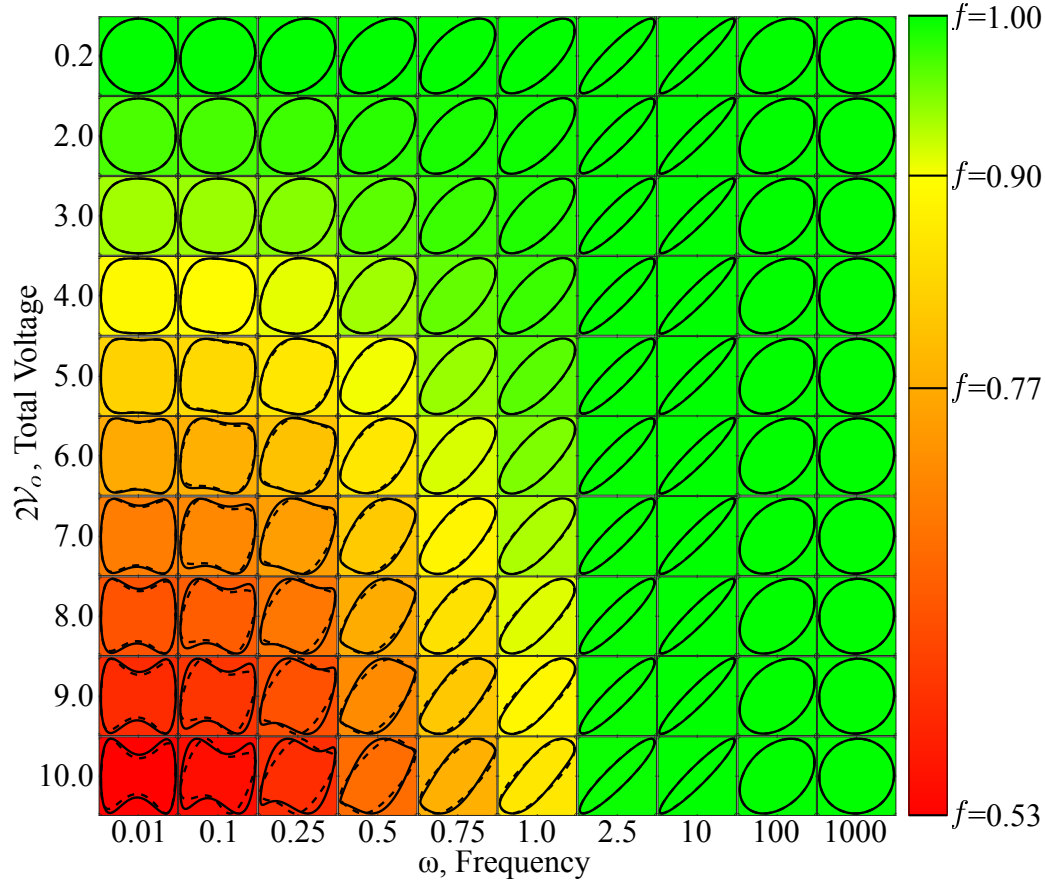


Figure 2.4: Pipkin diagram for $\epsilon = 0.025$. On each plot, the horizontal axis is voltage and the vertical axis is current, both scaled to be in the range $[-1, 1]$. The solid lines are the result from our moderately nonlinear expansion and the dashed lines are numerical solutions to the PNP equations. The frequency, ω , increases to the right and the total applied voltage difference increases down. The color is based upon the linearity fraction, f , defined in equation (2.21) with two distinct regions: $f=[1, 0.9]$ the color changes from green to yellow; $f=[0.9, 0.53]$ the color changes from yellow to red and a linear theory captures relatively little of the dynamics. Also labeled on the color bar is $f = 0.77$, which is the value corresponding to $2V_o = 6$ and $\omega = 0.01$.

tions and traditional models of EIS even for large driving voltages. Using large voltages would be advantageous for eliminating noise in measurements of current.

Regarding the validity of our moderately nonlinear expansions (2.10), we see excellent agreement with the full numerical solution for all ω up to $2\mathcal{V}_o = 6$ and for all $\omega > 1$ for $2\mathcal{V}_o > 6$, where $f = 0.77$ in the former and the dynamics are predominately linear in the latter. For $2\mathcal{V}_o > 6$ and $\omega < 1$, we still capture the qualitative features of the current. This highlights the usefulness of (2.10) in describing a moderately nonlinear response.

For comparison with the above thin Debye layer ($\epsilon = 0.025$) diagram, figure 2.5 is a Pipkin diagram for $\epsilon = 0.25$. The coloring scheme and scale is identical to the one used in figure 2.4. Once again, the most nonlinear response is seen for low frequencies at high voltages and becomes more linear as frequency increases. One significant difference is the linearity factor (2.21) suggests the response is more linear for all values of \mathcal{V}_o plotted since $f > 0.82$. Comparing the full numerical solutions for $\omega = 0.01$, we conclude that the same voltage of $2\mathcal{V}_o = 6$ is the largest voltage amplitude for which our expansion has good agreement. Here, it corresponds to $f = 0.93$, compared with $f = 0.77$ for $\epsilon = 0.025$. The Lissajous plots are also hexagon-like in shape at large voltages which contrasts to the “bow-tie”-like shape for $\epsilon = 0.025$. The apparent lack of this feature in our perturbation analysis suggests more terms in the voltage expansion are needed as ϵ increases. Another difference is that for $\epsilon = 0.25$, the plots are generally more circular than the corresponding plot for $\epsilon = 0.025$. This is a direct consequence of there being fewer ions in the electrolyte and hence less in-phase conduction. Alternatively, the thicker Debye cloud at larger ϵ results in a diminished frequency gap between the capacitive response due to the dielectric solvent and the Debye layer.

To better understand how higher order harmonics (specifically the third

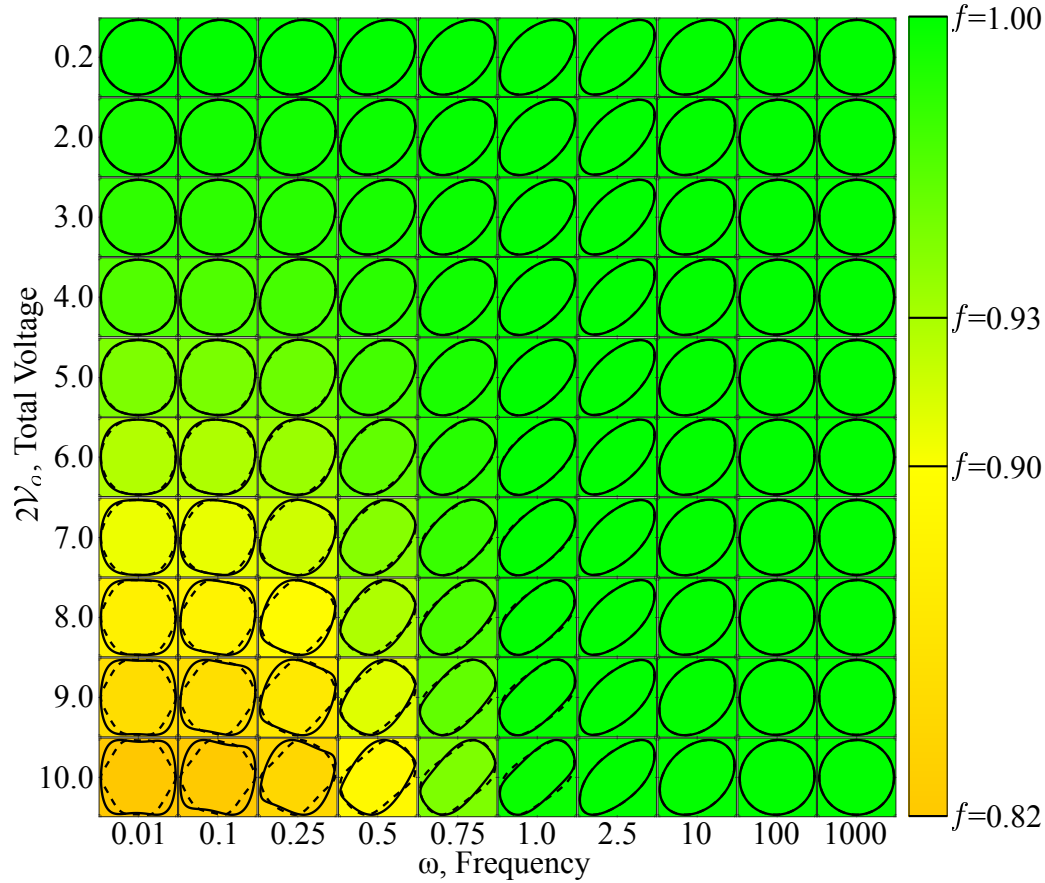


Figure 2.5: Pipkin diagram for $\epsilon = 0.25$. The solid and dashed lines represent the moderately nonlinear calculations and the numerical solutions, respectively. The color legend is the same as in figure 2.4. Also labeled on the color bar is $f = 0.93$, which is the value corresponding to $2\mathcal{V}_o = 6$ and $\omega = 0.01$.

harmonic) effect the current, figure 2.6 shows how the current response changes with frequency for a linear ($\mathcal{V}_o = 0.1$, solid) and moderately nonlinear ($\mathcal{V}_o = 3$, dashed) voltage amplitude. The presence of the third harmonic, $e^{3i\omega t}$, is readily apparent in figure 2.6 for $\omega = 0.01$ and results in a “double-peak” in the current versus time plot and a “bow-tie” in the Lissajous plot. Also apparent is the lack of a second harmonic which if non-zero would reduce the size of the second peak.

As the frequency increases, the current shifts to be more in-phase with the applied voltage and the second peak starts to diminish. The phase shift is due to a reduction in Debye layer capacitance resulting in a relative increase

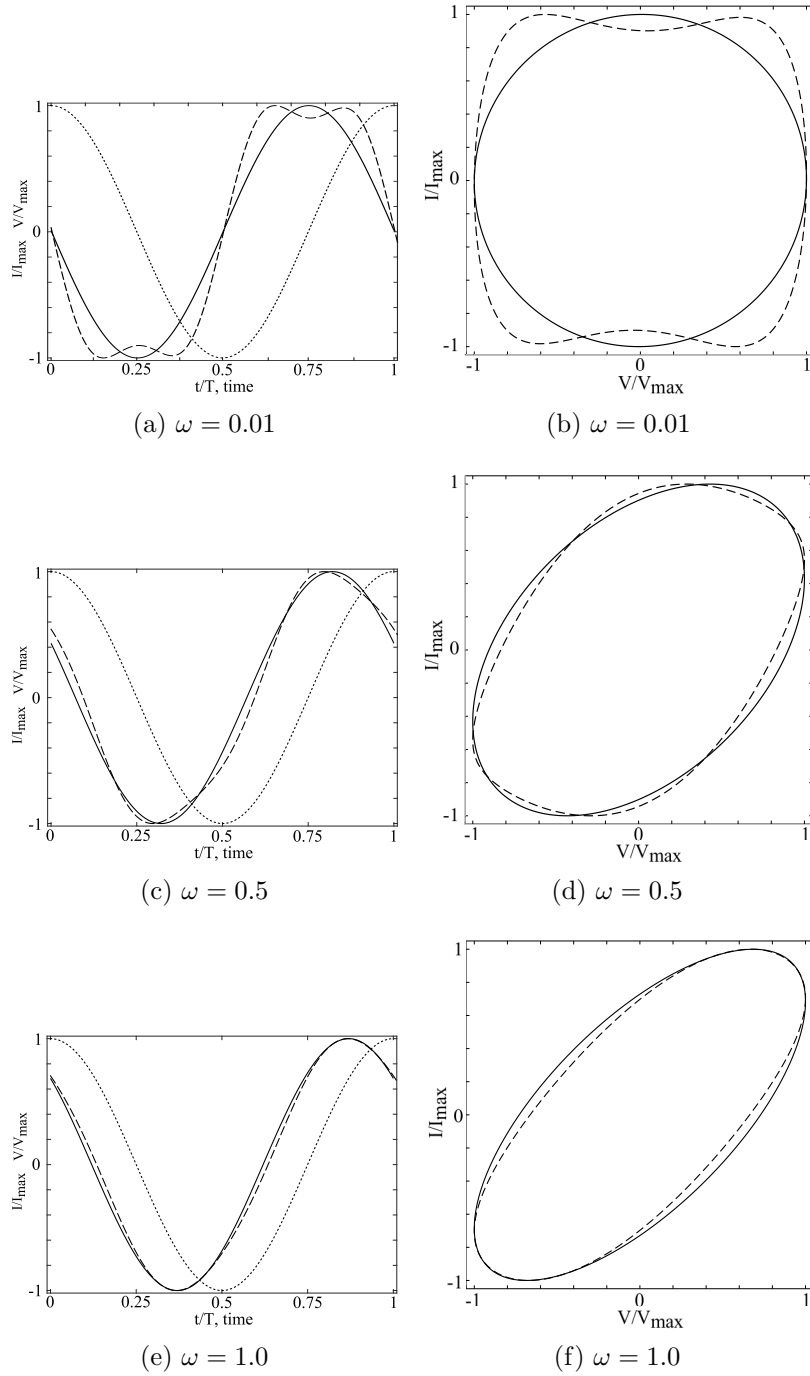


Figure 2.6: Dependence of current on frequency. Solid lines are linear dynamics ($\mathcal{V}_o = 0.1$), dashed lines are moderately nonlinear ($\mathcal{V}_o = 3$), and dotted lines are the applied voltage. The “double-peak” visible in (a) and the “bow-tie” in (b) are due to the third harmonic of current. This harmonic gradually loses amplitude relative to the linear contribution as frequency increases.

in in-phase conduction (see explanation for (2.20)). The second peak results from the third harmonic and as ω approaches 1 from low values, higher order harmonics ($\phi_1^{(3)}$, $\phi_3^{(3)}$, etc.) become less prominent. That is, they decrease in amplitude relative to $\phi_1^{(1)}$. Since the second peak is due entirely to the third harmonic, this necessarily leads to it vanishing. As it diminishes, the nonlinear current more closely resembles that of the linear response. The second peak could also be reduced by the existence of a second harmonic in the case of asymmetric electrolytes, but $\phi_2^{(2)} = 0$ is guaranteed for symmetric, point-like electrolytes. Even if $\phi_2^{(2)} \neq 0$, it would also diminish in amplitude as ω increases.

Therefore, linear dynamics can result at high voltages because the higher order harmonic modes decrease in amplitude as frequency increases. This results in a reduction in the extent of ion motion and less capacitive storing in Debye layers. Since the nonlinear response is a direct consequence of the capacitive storing, the result is increased linearity in the current response.

Interestingly, the ion densities predicted in figure 2.3 could lead to unphysical values at sufficiently large \mathcal{V}_o even though each term in (2.10) is correct, as we show in figure 2.7. It is a plot of total cation density for a small voltage ($\mathcal{V}_o = 0.1$) and two larger voltages ($\mathcal{V}_o = 1$ and 2) at $\omega = 0.01$ and $t = 0$. For $\mathcal{V}_o = 0.1$, the ion perturbation is primarily due to $O(\mathcal{V}_o)$ effects and is thus antisymmetric. For $\mathcal{V}_o = 1$, the total perturbation is unequal due to the symmetric $O(\mathcal{V}_o^2)$ contribution, giving rise to an increased density of cations on the negative electrode ($x = -1$) compared to the smaller decrease in density on the positive electrode ($x = 1$). For $\mathcal{V}_o = 2$, the asymmetric $O(\mathcal{V}_o^3)$ perturbation is now prevalent enough to significantly affect the ion densities. As a consequence, the positive electrode has a negative density of cations at its surface. It is clearly not physically possible to have negative ion concentrations; however, this does not mean our approach is incorrect. Again, we

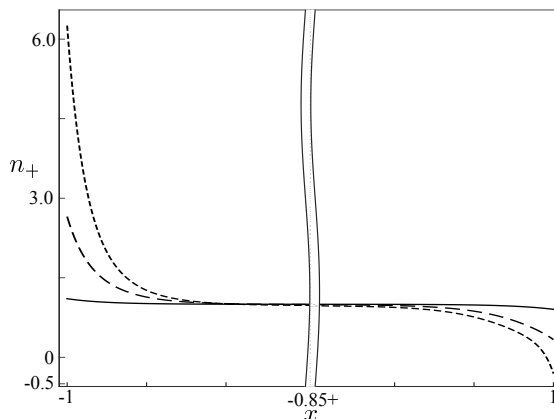


Figure 2.7: Total cation density for $\omega = 0.01$ and $t = 0$ at three voltages: $\mathcal{V}_o = 0.1$ (solid), $\mathcal{V}_o = 1$ (dashed), and $\mathcal{V}_o = 2$ (dotted). As the voltage increases, the ion density becomes less antisymmetric and for $\mathcal{V}_o = 2$ attains a negative value at $x = 1$.

emphasize that the individual contributions in figure 2.3 are correct. We use a regular perturbation expansion in \mathcal{V}_o which is asymptotic as $\mathcal{V}_o \rightarrow 0$ so it is expected to break down at some \mathcal{V}_o greater than unity. In this view, it is remarkable that the predicted current responses in figure 2.4 agree well with numerics at $\mathcal{V}_o = 2$ and $\omega = 0.01$ and beyond (and even at larger voltages, as explained above).

2.4 Weakly Nonlinear Impedance

Electrochemical impedance spectroscopy (EIS) uses an experimental system such as figure 2.1 where the electrodes are sufficiently close such that the charge transport occurs primarily normal to the electrode surface. A time varying voltage, $V(t) = \mathcal{V}_o \cos(\omega t)$, is imposed resulting in the charging/discharging of the Debye layers and a current response, $I(t)$. Provided that $\lambda_D \ll L$, the system is analogous to an equivalent circuit in which the two Debye layers are described as capacitors in series with the electrolyte's resistance and in parallel is the geometric capacitance of the cell itself via the dielectric solvent.

It is convenient to express the voltage and current as complex quantities:

$V(t) = \mathcal{V}_o e^{i\omega t}$ and $I(t) = I_1^{(1)} e^{i\omega t}$. Then the impedance for a symmetric binary electrolyte, defined as $Z = V(t)/I(t)$, is given by[61]

$$Z = \frac{-2\epsilon}{\beta^2 \omega^2} \left[\frac{i}{\beta} \tanh\left(\frac{\beta}{\epsilon}\right) - \omega \right], \quad (2.22)$$

where $\beta = \sqrt{1 + i\omega\epsilon}$. Equation (2.22) can be used to determine physical properties of the electrolyte such as conductivity and dielectric permittivity by determining the limiting behavior of the real and imaginary components at small and large frequencies[29, 30].

Equation (2.22) is formally valid when $\mathcal{V}_o \ll \mathcal{V}_c$, i.e. linear response. When this condition is violated, higher order harmonic modes must be included in the expression for $I(t)$. The result is a time dependent ‘‘impedance,’’ if defined by simply dividing the voltage by the current. Alternatively, following Olesen *et al.* [63], we define a generalized impedance,

$$\mathcal{Z} = \frac{\int_0^T V(t) e^{-i\omega t} dt}{\int_0^T I(t) e^{-i\omega t} dt}, \quad (2.23)$$

to capture only those contributions to the current oscillating at the applied frequency. Hence, \mathcal{Z} is time independent.

Given that the current is $I(t) = \mathcal{V}_o I^{(1)}(t) + \mathcal{V}_o^3 I^{(3)}(t)$, it is natural to assume a similar expression for \mathcal{Z} is

$$\mathcal{Z} = \mathcal{Z}^{(0)} + \mathcal{V}_o^2 \mathcal{Z}^{(2)} + O(\mathcal{V}_o^4). \quad (2.24)$$

This expression provides an approximation to the voltage dependence observed in impedance measurements at large voltages[30, 61, 63]. We can express \mathcal{Z} in terms of the components of the electrostatic potential,

$$\mathcal{Z} = \frac{1}{i\omega} \left[\frac{1}{d\phi_1^{(1)}/dx} - \mathcal{V}_o^2 \frac{d\phi_1^{(3)}/dx}{(d\phi_1^{(1)}/dx)^2} \right]. \quad (2.25)$$

Figure 2.8 are plots of $\text{Im}(\mathcal{Z})$ and $\text{Re}(\mathcal{Z})$ versus ω for $\epsilon = 0.025$ and 0.25 and $\mathcal{V}_o = 0.1$ and 3 . At high frequency, the imaginary impedances are

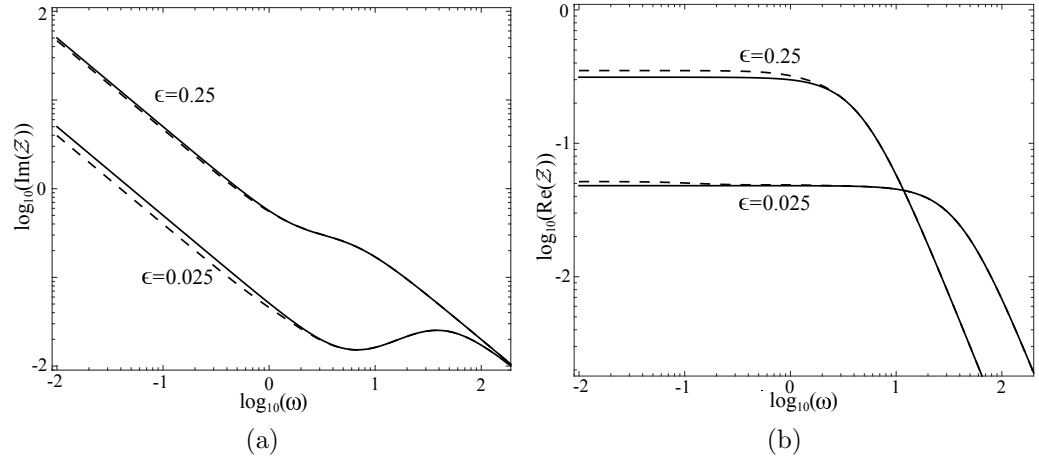


Figure 2.8: Imaginary (a) and real (b) parts of the generalized impedance defined in (2.23) versus frequency of applied voltage for $\epsilon = 0.025$ and 0.25 . The voltages plotted are $\mathcal{V}_o = 0.1$ (solid) and $\mathcal{V}_o = 3$ (dashed).

equal due to the aforementioned capacitance of the dielectric dominating the response. For small frequencies, however, the impedances are unequal.

The low frequency impedance increases with increasing Debye layer thickness. The imaginary part increases due to a reduction in capacitance and the real part due to an increased resistance - both due to less ions in the electrolyte. The decrease in $\text{Im}(\mathcal{Z})$ with increasing voltage for both values of ϵ is due to the behavior of the Debye layer as a nonlinear capacitor. As voltage increases, the capacitance also increases. Since $\text{Im}(\mathcal{Z})$ is inversely proportional to capacitance, it decreases[63]. For $\epsilon = 0.25$, this decrease is less pronounced than for $\epsilon = 0.025$ because of the lower ion concentration in the thick Debye layer case.

From figure 2.8b, $\text{Re}(\mathcal{Z})$ is shown to increase with increasing voltage, for both values of ϵ , which corresponds to an increase in resistance. This can be attributed directly to the neutral salt adsorption from the bulk solution into the Debye layers at $O(\mathcal{V}_o^2)$. This causes a reduction in conductivity and hence an increase in $\text{Re}(\mathcal{Z})$. Since there are fewer ions in solution in the $\epsilon = 0.25$ case, any ions adsorbed into the Debye layers represent a greater proportion

of the total ion concentration. Hence, the increase in resistance is greater for $\epsilon = 0.25$.

2.5 Conclusions

We have quantified diffuse charge dynamics of a symmetric binary electrolyte at moderately nonlinear AC voltages. We used a Fourier series expansion in driving frequency for which the coefficients are expressed as a perturbation series in voltage amplitude. This approach allows the evaluation of nonlinearities in terms of both voltage order and harmonic mode. We find that the odd voltage orders have antisymmetric ion densities and electrostatic potential profiles. For symmetric electrolytes, the even voltage orders have ion densities that are symmetric and equal while the electrostatic potential is zero.

The symmetry in the $O(\mathcal{V}_o^2)$ ion densities represents “AC capacitive desalination” [63] in which neutral salt from the bulk solution adsorbs into the diffuse charge layers near the electrodes. The result is a reduced total salt concentration in the bulk and an increased resistance. Moreover, the net, or time averaged, separation of neutral salt is captured by the steady $O(\mathcal{V}_o^2)$ contribution.

We use our expansion to express a voltage dependent impedance. For low frequencies, we observe the increased bulk resistance manifesting as an increase in the real part of the impedance. The imaginary part of the impedance decreases with voltage due to the increase in Debye layer capacitance as predicted by Gouy-Chapman theory.

In this work, we considered a binary symmetric electrolyte, for simplicity. Asymmetry could be introduced through unequal ion valences or diffusivities, which would require only minor modification to our moderately nonlinear expansions. Such asymmetry would result in a non-zero $O(\mathcal{V}_o^2)$ potential, and

hence unequal neutral salt adsorption and an $O(\mathcal{V}_o^2)$ contribution to the current. In addition, it would be interesting to consider modified PNP equations that account for ion-size effects [26] and ion-ion electrostatic correlations [67]. In the former case, various modified PNP equations including finite-ion-size effects predict a Debye layer capacitance that only weakly increases with voltage, in contrast to the exponential increase of the capacitance from Gouy-Chapman theory. Clearly, ion steric effects would thus dramatically impact the low-frequency impedance at large voltages. Finally, future work could also incorporate asymmetrically applied voltages and non-zero native zeta potentials to model asymmetric electrochemical supercapacitors, where the electrodes are made of differing materials.

Chapter 3

Diffuse-Charge Dynamics in Ionic Thermo-Electrochemical Systems

3.1 Introduction

The thermoelectric effect is the generation of a voltage across an electrically conducting material in response to an applied temperature gradient. When subjected to a temperature gradient, charge carriers will tend to migrate toward colder regions of the material [68], but have differing thermal diffusion coefficients, thereby generating a “thermo-voltage,” V_T . This is analogous to the “diffusion potential” generated under an applied concentration gradient of charge carriers [40]. The thermo-voltage is related to the temperature difference across the material, ΔT , by the Seebeck coefficient, Se , or thermo-power,

$$V_T = -Se\Delta T, \quad (3.1)$$

where the negative sign is by definition such that the lower temperature corresponds to a higher potential. The ability of a thermoelectric material to convert thermal energy into electrical energy is characterized by the figure of merit, $ZT = Se^2\sigma T/\lambda$, where σ is the electrical conductivity and λ is the thermal conductivity [69]. Traditional thermo-electric devices utilize inorganic

semiconducting materials, which contain electronic charge carriers, resulting in $ZT \approx 0.1 - 1$, while nano-structured devices have been fabricated with $ZT \approx 2 - 3.5$ [31, 70, 71], achieved by having large electrical conductivities, $O(10^3 \text{ S/cm})$ at room temperature, and Seebeck coefficients of $O(100 \mu\text{V/K})$ [71, 72]. However, this still places their efficiency below that of other heat engines [31]. Moreover, these inorganic thermo-electrics are usually composed of rare, expensive, and sometimes toxic materials [73].

Due to these drawbacks, there has been recent interest in “soft” thermo-electric materials containing ionic charge carriers such as ionic liquids [8, 9, 10], non-aqueous organic electrolytes [74], and mixed ionic-electronic conducting polymers [11, 12, 13, 14, 15]. Although these come with a reduction in electrical conductivity compared to semiconductor based thermo-electrics, they can be competitive due to having much larger Seebeck coefficients, on the order of mV/K [13, 14, 15, 74]. This enables such materials to store more charge [15] and provides a pathway for designing devices which have figures of merit comparable to semiconductor based devices. In addition, the materials used tend to be much cheaper to process and less toxic, making them good candidates for wearable devices, and mass production [73].

For example, Zhao *et al.* [15] utilized polyethylene oxide with anionic end groups and sodium ions as the counterions to obtain a Seebeck coefficient of 11.1 mV/K . Chang *et al.* [13] used polymeric ethylenedioxythiophene (PEDOT) and polystyrenesulphonate (PSS) doped with silver ions and achieved $\text{Se} = 0.1 \text{ mV/K}$ with $ZT = 0.13$, stable over $O(10^3 \text{ s})$ compared to the undoped material which exhibited a decay in Se over $O(100 \text{ s})$. Kim *et al.* [14] use a PSS-based thermo-electric generator to achieve an ionic Seebeck coefficient of 8 mV/K and $ZT = 0.4$. A non-aqueous solution of tetrabutylammonium nitrate in dodecanol was reported to have $\text{Se} = 7 \text{ mV/K}$ by Bonetti *et al.* [74].

A commonality among these soft material based thermo-electric devices

is charging times, i.e., the time to reach a steady state thermo-voltage, on the order of hundreds to thousand of seconds[13, 14, 15]. Clearly, such long times warrant an investigation of the dynamics of diffuse ionic charge carriers in thermo-electrics materials. However, mathematical modeling for even the simplest case of a binary electrolyte has not included an analysis of the charging dynamics, and instead considers only the steady state thermo-voltage and ion distributions across a device [20, 32, 33]. At steady-state, in an electroneutral solution, the Seebeck coefficient is $Se_E = k_B(\alpha_+ - \alpha_-)/e$ [33], where k_B is Boltzmann's constant, e is the elementary charge, and the subscript E denotes the steady-state electroneutral solution value. The quantities α_+ and α_- are the reduced Soret coefficients, which are related to the ratios of the thermal diffusion coefficients to the Brownian diffusion coefficients of the cation (+) and anion (-), respectively. For the similar problem of a suddenly applied voltage at a constant, uniform temperature, the relevant time scale for the charging of the Debye, or diffuse, screening layers of ionic charge adjacent to the electrodes is the RC time, $L/D\kappa$, where L is the distance between electrodes, $1/\kappa$ is the Debye length, and D is the Brownian diffusion coefficient of the ions [59]. However, it is not clear what the time scale would be for a suddenly applied temperature gradient, since the ions undergo both Brownian and thermal diffusion. A central goal of the present chapter is to address this point.

Therefore, we systematically investigate the charge dynamics of a prototypical ionic thermo-electrochemical cell subjected to a suddenly applied temperature gradient between two parallel, perfectly blocking electrodes. We find that, for “weak” applied temperature gradients (where “weak” will be defined precisely in what follows), the Debye time, $1/D\kappa^2$, is the relevant time scale for development of the thermo-voltage and charging of the diffuse layers, whereas the diffusion time, L^2/D , is the time scale of bulk diffusion of neu-

tral salt. In section 3.2, we formulate the mathematical problem and obtain the time scales for charge, salt, and thermo-voltage evolution. In section 3.3, we examine the time evolution of the profiles for these quantities across the cell. In section 3.4, we offer some concluding remarks, including a qualitative comparison to the above mentioned experiments.

3.2 Problem Formulation

Consider two parallel electrodes a distance $2L$ apart which are not connected via an external circuit as depicted in figure 3.1. The space between the electrodes is occupied by a fully dissociated binary electrolyte solution with positive ion number density n_+ and negative ion number density n_- . The cations (+) and anions (-) have equal charge number, z , and equal Brownian diffusion coefficients, D , but differing thermal diffusion coefficients, $D_{T,i}$, such that their reduced Soret coefficients are α_+ and α_- , respectively, and $\alpha_+ \neq \alpha_-$. Initially, at time $t < 0$, the system is in thermal equilibrium at a constant, uniform temperature T_0 , with uniform ion number densities $n_{+,0}$ and $n_{-,0}$. At time $t \geq 0$, the electrode at $x = +L$ (henceforth referred to as the hot electrode) is heated to a temperature $T_H > T_0$ while the electrode at $x = -L$ (the cold electrode) is maintained at the initial temperature T_0 .

As the heat propagates through the cell, the ions migrate via the Soret effect toward the cold electrode [68], which is balanced by Brownian diffusion and electro-migration via the induced electric field within the cell. The ions migrate at different rates according to their reduced Soret coefficients, $\alpha_i = TD_{T,i}/2D$. For example, in the simple salt KCl, the Brownian diffusion coefficients are approximately equal [34] but the reduced Soret coefficients are $\alpha_+ = 0.5$ and $\alpha_- = 0.1$ [32]. This tendency to migrate at different rates results in a local electric field and hence a macroscopic voltage across the cell, termed

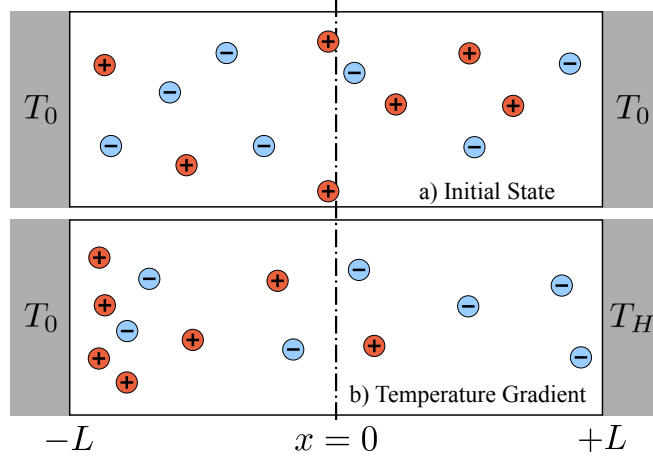


Figure 3.1: Sketch of the model problem. The initial, isothermal state is depicted in figure (a); the charges are uniformly distributed. Upon heating the an electrode to a temperature $T_H > T_0$, the charges migrate towards the colder regions of the cell, shown in figure (b). Two effects are depicted in (b): the concentration gradient and the regions of net charge near the electrodes.

the thermo-voltage, which acts to ensure no net current.

Assuming the distance between the electrodes is much smaller than the other dimensions, which is reasonable considering devices often have separations on the order of millimeters [13, 14, 15], the dynamics of this system are governed by the one dimensional ion conservation equation,

$$\frac{\partial n_{\pm}}{\partial t} = -\frac{\partial j_{\pm}}{\partial x}, \quad (3.2)$$

where t is time, and j_{\pm} is the flux of the cations (+) or anions (-), given by [32]

$$j_{\pm} = -Dn_{\pm} \left(\frac{\partial \ln n_{\pm}}{\partial x} \pm \frac{ze}{k_B T} \frac{\partial \phi}{\partial x} + 2\alpha_{\pm} \frac{\partial \ln T}{\partial x} \right), \quad (3.3)$$

where e is the elementary charge, k_B is Boltzmann's constant, T is temperature, and ϕ is electrostatic potential. Equation (3.3) therefore represents the sum of the Brownian-diffusive, electromigrative and thermo-diffusive fluxes of ions, respectively.

The electrostatic potential is governed by Poisson's equation,

$$-\frac{\partial}{\partial x} \left(\epsilon \frac{\partial \phi}{\partial x} \right) = \rho = ez(n_+ - n_-), \quad (3.4)$$

where ε is the permittivity of the solution and ρ is the ionic charge density. Finally, the temperature evolves according to the heat equation,

$$\frac{\partial}{\partial t}(\eta C_p T) = \frac{\partial}{\partial x} \left(\lambda \frac{\partial T}{\partial x} \right), \quad (3.5)$$

where η is the density, C_p is the heat capacity per mass, and λ is the thermal conductivity of the solution.

These equations are supplemented with the following initial conditions specifying temperature, and the uniform ion densities,

$$T(x, t < 0) = T_0, \quad (3.6a)$$

$$n_{\pm}(x, t < 0) = n_{\pm,0}. \quad (3.6b)$$

The boundary conditions specify no flux of ions and no electric field at the electrode surfaces, and the temperature applied to the electrodes:

$$j_{\pm}(x = +L, t \geq 0) = 0, \quad (3.7a)$$

$$j_{\pm}(x = -L, t \geq 0) = 0, \quad (3.7b)$$

$$\frac{\partial \phi}{\partial x}(x = \pm L, t \geq 0) = 0, \quad (3.7c)$$

$$T(x = +L, t \geq 0) = T_H, \quad (3.7d)$$

$$T(x = -L, t \geq 0) = T_0. \quad (3.7e)$$

Equation (3.7c) arises from Gauss's law and the fact that there is no external circuit connected to either electrode through which they could develop a charge. Note that (3.7d) assumes the electrode is instantly heated from T_0 to T_H . The ultimate quantity of interest, the thermo-voltage generated, is calculated from an integral of the resultant electrostatic potential gradient across the entire cell,

$$V_T = \int_{-L}^{+L} \frac{\partial \phi}{\partial x} dx = \phi(L, t) - \phi(-L, t). \quad (3.8)$$

3.2.1 Linear Dynamics under Weak Temperature

Gradients

This mathematical problem (3.2)-(3.8) is impossible to solve exactly. Not only are there nonlinearities in the ion flux equations (3.3), but the physical properties (permittivity, diffusion coefficients, etc.) of the solution vary with temperature and hence with time and position. In general, mathematical expressions, or experimentally determined correlations, to approximate the temperature dependence of these properties would be necessary. To make progress, we assume that, after all transients have died out, the resulting temperature gradient $G_f = (T_H - T_0)/2L$ is small, such that $G_f \ll T_0/2L$. This condition can be expressed solely in terms of the temperatures involved as $\Delta T \ll T_0$, where $\Delta T = T_H - T_0$. Assuming a thermo-electric device is intended to operate at least at room temperature, $T_0 \approx 300$ K, then $O(1)$ K temperature differences would readily suffice to meet this condition. Several devices operate in this regime [13, 14, 15, 74]. Thus, defining a small parameter $\delta = G_f 2L/T_0 = \Delta T/T_0 \ll 1$, we can express all unknowns as perturbations to their initial state by a small temperature gradient. Hence for a general quantity, $f = f_0 + \delta f_1$, where f_0 is the initial state and f_1 is the perturbed contribution due to the temperature gradient. The resulting $O(1)$ problem is merely the initial state of the system prior to applying a temperature gradient, and the $O(\delta)$ problem becomes

$$\frac{\partial n_{\pm,1}}{\partial t} = -\frac{\partial j_{\pm,1}}{\partial x}, \quad (3.9a)$$

$$j_{\pm,1} = -D_0 \left(\frac{\partial n_{\pm,1}}{\partial x} \pm \frac{z e n_{\pm,0}}{k_B T_0} \frac{\partial \phi_1}{\partial x} + \frac{2\alpha_{\pm,0} n_{\pm,0}}{T_0} \frac{\partial T_1}{\partial x} \right), \quad (3.9b)$$

$$\frac{\partial^2 \phi_1}{\partial x^2} = -\frac{\rho_1}{\varepsilon_0} = -\frac{e z}{\varepsilon_0} (n_{+,1} - n_{-,1}), \quad (3.9c)$$

$$\frac{\partial T_1}{\partial t} = \frac{\lambda_0}{\eta_0 C_{p,0}} \frac{\partial^2 T_1}{\partial x^2}, \quad (3.9d)$$

where to obtain (3.9d) it is assumed that the heat capacity and density do not change appreciably with temperature such that the ratios $C_{p,1}/C_{p,0}$ and η_1/η_0 are negligible. This is a reasonable assumption for dilute aqueous electrolytes [34]. The initial and boundary conditions for the $O(\delta)$ problem are

$$n_{\pm,1}(x, t < 0) = 0, \quad (3.10a)$$

$$T_1(x, t < 0) = 0, \quad (3.10b)$$

$$j_{\pm,1}(x = +L, t \geq 0) = 0, \quad (3.10c)$$

$$j_{\pm,1}(x = -L, t \geq 0) = 0, \quad (3.10d)$$

$$\frac{\partial \phi_1}{\partial x}(x = \pm L, t \geq 0) = 0, \quad (3.10e)$$

$$T_1(x = +L, t \geq 0) = T_0, \quad (3.10f)$$

$$T_1(x = -L, t \geq 0) = 0, \quad (3.10g)$$

and the thermo-voltage is obtained from (3.8) as

$$V_T = \delta \int_{-L}^{+L} \frac{\partial \phi_1}{\partial x} dx = \delta [\phi_1(L, t) - \phi_1(-L, t)]. \quad (3.11)$$

Next, we eliminate temperature as an unknown quantity by assuming that the heat diffusivity is much greater than both ion diffusion coefficients, i.e., $k_0/\eta_0 C_{p,0} \gg D_0$ and $k_0/\eta_0 C_{p,0} \gg T_0 D_{T,0}$. That is, we assume the temperature within the electrolyte responds instantaneously to variations in the electrode temperature, compared to the response of the ions. This assumption is valid for aqueous solutions of electrolytes, where the ratio $k/\eta C_p D \approx 100$ [34] and $\alpha_i \approx 1$ [32]. For thermo-electric devices which use large, non-aqueous or organic charge carriers, this ratio will be much greater than unity due to a smaller Brownian diffusion coefficient [75]. Therefore, compared to the relatively slow diffusion of ions, the heat diffuses rapidly through the cell and the temperature has the quasi-steady linear profile

$$T(x, t) = T_0 + G(t)(x + L), \quad (3.12)$$

where $G(t) = (T_H(t) - T_0)/2L$ is the time dependent temperature gradient, reflecting the heating of the hot electrode. We now assume that the hot electrode achieves its final temperature instantaneously, and replace $G(t)$ with G_f . To eliminate T_1 from (3.9b), we express the left hand side of (3.12) as a perturbation expansion and obtain $\partial T_1/\partial x = G_f/\delta = T_0/2L$. The linearized ion flux is thus

$$j_{\pm,1} = -D_0 \left(\frac{\partial n_{\pm,1}}{\partial x} \pm \frac{z e n_{\pm,0}}{k_B T_0} \frac{\partial \phi_1}{\partial x} + \frac{\alpha_{\pm,0} n_{\pm,0}}{L} \right), \quad (3.13)$$

and the thermo-diffusive contribution has been reduced to a constant at this order, $-D_0 \alpha_{\pm,0} n_{\pm,0}/L$.

Next, we define

$$c = \frac{n_+ + n_-}{2z}, \quad (3.14a)$$

$$\rho_c = \frac{n_+ - n_-}{2z}, \quad (3.14b)$$

such that c represents the neutral salt concentration and $e\rho_c$ represents a corresponding charge density. Substituting these definitions into (3.9) and (3.13) yields,

$$\frac{\partial c_1}{\partial t} = D \frac{\partial^2 c_1}{\partial x^2}, \quad (3.15a)$$

$$\frac{\partial \rho_{c,1}}{\partial t} = D \frac{\partial^2 \rho_{c,1}}{\partial x^2} - D \kappa^2 \rho_{c,1}, \quad (3.15b)$$

$$\frac{\partial^2 \phi_1}{\partial x^2} = -\frac{2ez^2}{\varepsilon_0} \rho_{c,1}, \quad (3.15c)$$

where $1/\kappa = \sqrt{\varepsilon_0 k_B T_0 / 2e^2 z^3 c_0}$ is the Debye length in terms of the initial state, prior to applying a temperature gradient. The initial and boundary conditions (3.10a)-(3.10d) become

$$c_1(x, t < 0) = 0, \quad (3.16a)$$

$$\rho_{c,1}(x, t < 0) = 0, \quad (3.16b)$$

$$\frac{\partial c_1}{\partial x}(\pm L, t) = -\frac{c_0 \alpha_m}{L}, \quad (3.16c)$$

$$\frac{\partial \rho_{c,1}}{\partial x}(\pm L, t) = -\frac{c_0 \alpha_d}{L}, \quad (3.16d)$$

where $\alpha_m = (\alpha_{+,0} + \alpha_{-,0})/2$ and $\alpha_d = (\alpha_{+,0} - \alpha_{-,0})/2$ and we have used (3.10e) to eliminate the electrostatic potential gradient. Note that, at least to first order in the applied gradient, all thermal dependence is found in the boundary conditions (3.16c) and (3.16d) through the reduced Soret coefficients. Physically, this means, as we will see, that changing the Soret coefficients alters only the magnitude of the charge density, concentration, and thermo-voltage at any point in time; the charging dynamics are unaffected. That is, surprisingly, we expect the time it takes to reach a steady state to be independent of the thermal diffusion of the ions.

We now introduce Laplace transforms, defined by

$$\hat{f}(x, s) = \int_0^\infty e^{-st} f(x, t) dt, \quad (3.17)$$

where s is the Laplace frequency. The governing equations are thus transformed to

$$\frac{d^2 \hat{c}_1}{dx^2} = r^2 \hat{c}_1, \quad (3.18a)$$

$$\frac{d^2 \hat{\rho}_{c,1}}{dx^2} = k^2 \hat{\rho}_{c,1}, \quad (3.18b)$$

$$\frac{d^2 \hat{\phi}_1}{dx^2} = -\frac{2ez^2}{\varepsilon_0} \hat{\rho}_{c,1}, \quad (3.18c)$$

where

$$k^2 = \frac{s}{D} + \kappa^2 \quad \text{and} \quad r^2 = \frac{s}{D},$$

with boundary conditions,

$$\frac{\partial \hat{c}_1}{\partial x}(\pm L, s) = -\frac{c_0 \alpha_m}{Ls}, \quad (3.19a)$$

$$\frac{\partial \hat{\rho}_{c,1}}{\partial x}(\pm L, s) = -\frac{c_0 \alpha_d}{Ls}. \quad (3.19b)$$

These equations are readily solved, yielding

$$\hat{c}_1(x, s) = -\frac{c_0\alpha_m}{rLs} \left(\frac{\sinh(rx)}{\cosh(rL)} \right), \quad (3.20a)$$

$$\hat{\rho}_{c,1}(x, s) = -\frac{c_o\alpha_d}{kLs} \left(\frac{\sinh(kx)}{\cosh(kL)} \right), \quad (3.20b)$$

$$\hat{\phi}_1(x, s) = -\frac{kT_0\alpha_d\kappa^2}{ezk^2s} \left(\frac{x}{L} - \frac{\sinh(kx)}{kL \cosh(kL)} \right). \quad (3.20c)$$

The Laplace transform of (3.11) yields $\hat{V}(s) = 2\delta\hat{\phi}_1(L, s)$; therefore the Laplace transform of the thermo-voltage is given by

$$\hat{V}(s) = -\frac{2k\Delta T\alpha_d\kappa^2}{ezk^2s} \left(1 - \frac{\tanh(kL)}{kL} \right). \quad (3.21)$$

The first term in both (3.20c) and (3.21) is due to the linear electrostatic potential drop across the bulk, electroneutral solution. In this region, the electric field which results from the unequal thermo-migration of the ion species is uniform. However, near the electrodes, diffuse layers with non-zero net charge develop and screen this electric field on the length scale $1/\kappa$, described by the second term in (3.20c) and (3.21).

3.2.2 Determining Time scales for Thermo-electric Charging

To determine the time scales for neutral salt diffusion, charge separation, and thermo-voltage evolution, we evaluate (3.20) at the cold electrode ($x = -L$). However, it is difficult to obtain physical insights into the dynamics from direct analytic inversion of the resulting equations. Therefore, we consider the limit of long times, $t \rightarrow \infty$, by taking the limit $s \rightarrow 0$. By expressing (3.20) and (3.21) as Taylor series about $s = 0$, we can obtain expressions of the form $(1/s)/(1 + \tau s)$ which has an inverse Laplace transform of $(1 - e^{-t/\tau})$, where τ

is the time scale which we seek. Doing so we find

$$c_1(-L, t) \sim c_0 \alpha_m (1 - e^{-t/\tau_c}), \quad (3.22a)$$

$$\rho_{c,1}(-L, t) \sim \frac{c_0 \alpha_d \tanh(\kappa L)}{\kappa L} (1 - e^{-t/\tau_\rho}), \quad (3.22b)$$

$$V_T(t) \sim -\frac{2k_B \Delta T \alpha_d}{ez} \left(1 - \frac{\tanh(\kappa L)}{\kappa L}\right) (1 - e^{-t/\tau_\phi}), \quad (3.22c)$$

where

$$\tau_c = \frac{L^2}{3D}, \quad (3.23a)$$

$$\tau_\rho = \frac{1}{2D\kappa^2} \left(1 - \frac{2\kappa L}{\sinh(2\kappa L)}\right), \quad (3.23b)$$

$$\tau_\phi = \frac{1}{2D\kappa^2} \frac{3 \tanh(\kappa L) + \kappa L (\tanh^2(\kappa L) - 3)}{\tanh(\kappa L) - \kappa L}, \quad (3.23c)$$

are the time scales associated with diffusion of neutral salt, diffuse layer charging, and thermo-voltage evolution, respectively.

We see in (3.23) that the time scales for charge density and thermo-voltage are both functions of κL but are proportional to the Debye time, $1/D\kappa^2$. In fact, for very thin diffuse layers, $\kappa L \rightarrow \infty$, $\tau_\rho \sim 1/2D\kappa^2$ and $\tau_\phi \sim 1/D\kappa^2$. This contrasts with the salt diffusion time scale, which is proportional to the bulk diffusion time, L^2/D , and is therefore independent of concentration and much longer than the Debye time for thin diffuse layers.

In figure 3.2 we compare the time scales (normalized by $1/D\kappa^2$) as a function of κL . For $\kappa L \ll 1$, or thick diffuse layers, all time scales are proportional to $(\kappa L)^2$ and hence diffuse charge, salt concentration and voltage all evolve on essentially the same time scale, the diffusion time. For $\kappa L \gg 1$, or thin diffuse layers, the charge and voltage time scales achieve the limiting values mentioned above while the salt diffusion time scale continues to increase as $(\kappa L)^2$. This suggests that the salt concentration profile evolves much more slowly than the charging of the diffuse layers and the thermo-voltage evolution for thin diffuse layers, which is the regime in which many devices operate [13, 14, 15, 74].

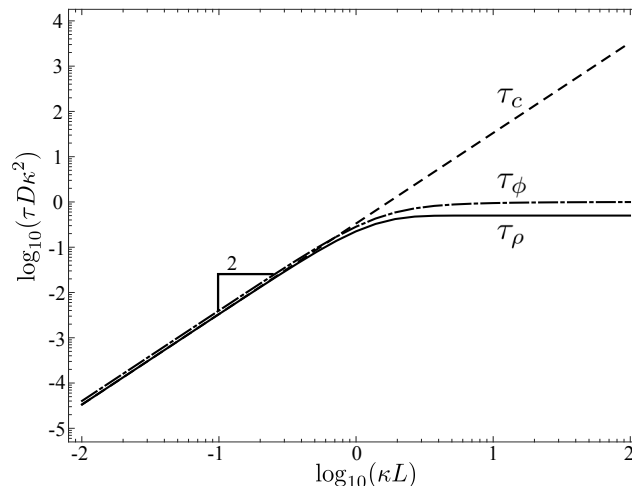


Figure 3.2: Dimensionless time scales for charge density, τ_ρ (solid), salt concentration, τ_c , (dashed) at the cold electrode (the hot electrode exhibits identical timescales) as well as voltage, τ_ϕ , (dot-dashed) versus κL . For $\kappa L \ll 1$, all time scales increase with a slope of 2. However, for $\kappa L \gg 1$, the charge density and voltage time scales reach a constant value of $1/2$ and 1 , respectively, but the concentration time scale continues to increase at the same rate.

Moreover, we see in equation (3.22c) that for thin diffuse layers, we recover the known steady state Seebeck coefficient for an electroneutral solution, $-V_T(t \rightarrow \infty)/\Delta T = 2k_B\alpha_d/ez = \text{Se}_E$ [33]. For finite κL , the Seebeck coefficient is reduced by $\text{Se}_E \tanh(\kappa L)/\kappa L$ due to screening of the induced electric field by the non-zero net charge and incomplete charge separation due to overlapping diffuse layers. As the diffuse layer shrinks, and hence the regions of non-zero net charge shrink, the thermo-voltage increases to the maximum value predicted for an electroneutral solution.

In figure 3.3, we plot the salt concentration and charge density at the cold electrode, calculated from the long-time solutions (3.22) and numerical inversion [76] of (3.20) versus time for several values of κL . Note that the concentration in figure 3.3(a) is the perturbed concentration relative to the uniform initial concentration. The positive perturbed concentration is the expected result of the Soret effect: that both ion species will be thermally induced to migrate toward the cold electrode. Further, as κL increases, it

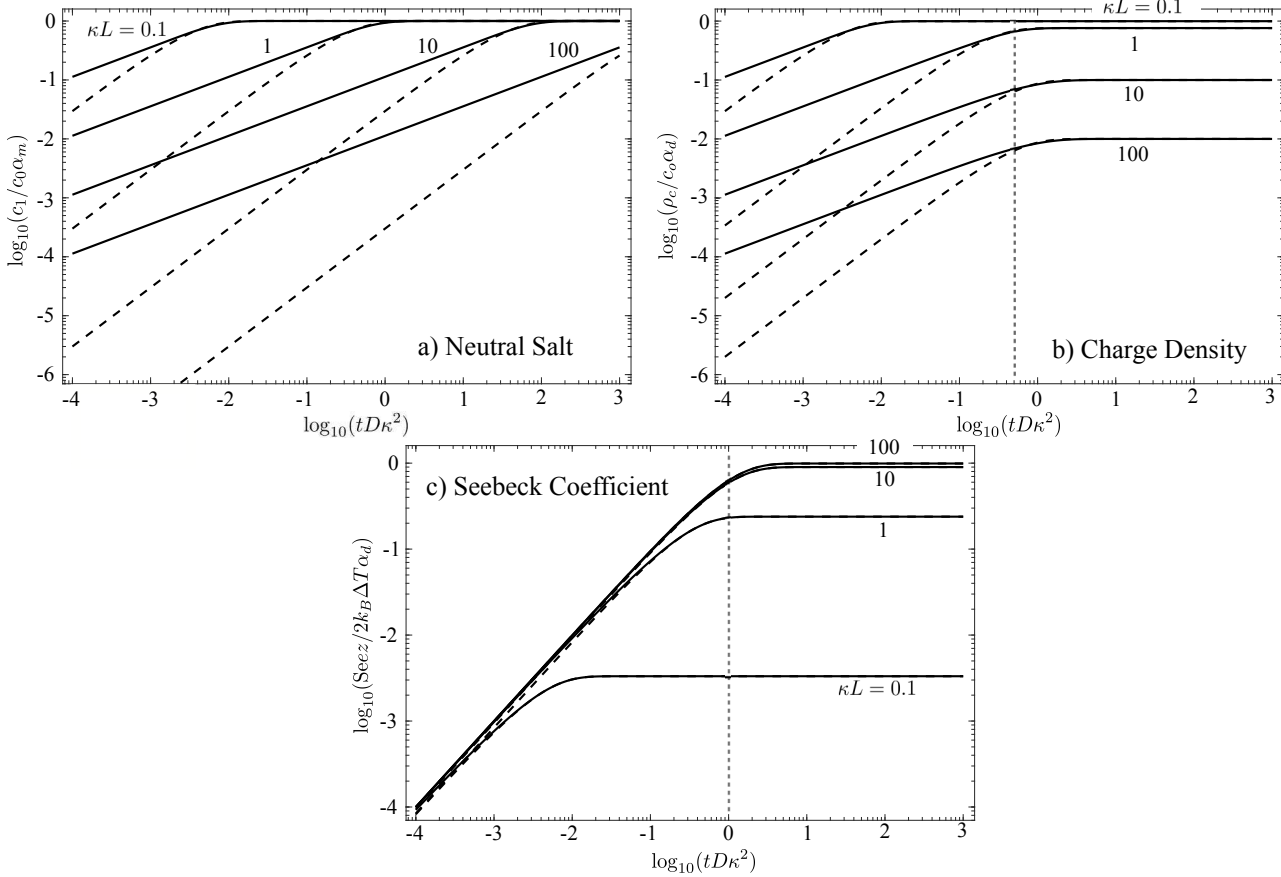


Figure 3.3: Salt concentration (a) and charge density (b) at the cold electrode ($x = -L$) along with the Seebeck coefficient (c), $\text{Se}(t) = -V(t)/\Delta T$, versus time at $\kappa L = 0.1, 1, 10$ and 100 . Numerical Laplace transform inversion of (3.20) are shown as solid lines; dashed lines are the long time solutions (3.22). For (a), at early times, salt concentration exponentially increases until the steady-state level is reached. The time to achieve steady-state increases as κL increases since the appropriate time scale for concentration evolution is L^2/D . For (b), at early times, charge density increases but achieves progressively lower charge densities at equilibrium. For (c), the Seebeck coefficient increases at approximately the same rate at early times but achieves progressively greater values, indicating larger thermo-voltages, as κL increases. The vertical dashed line in (b) and (c) indicate the thin diffuse layer limit of the respective time scales.

takes longer to reach the steady state value, as predicted by the time scales (3.23) and figure 3.2.

For positive values of α_d , which corresponds to $\alpha_+ > \alpha_-$, the cations undergo faster thermal migration than the anions. This results in the positive diffuse charge at the cold electrode predicted in figure 3.3(b). Recall that we

have assumed both ion species have equal Brownian diffusion coefficients. As κL increases, the amount of charge stored in the diffuse layer decreases and the equilibrium state is essentially achieved progressively closer to $t = 1/(2D\kappa^2)$, as indicated by the dashed vertical line in figure 3.3(b).

In figure 3.3(c), we plot the time dependent Seebeck coefficient, $Se(t) = -V_T(t)/\Delta T$ versus time. Surprisingly, the long-time solution (3.22c) agrees well with the numerical inversion even at short times. The steady state Seebeck coefficient increases with increasing κL , due to the shrinking diffuse layers as discussed previously. This indicates that in designing thermo-electric devices, it is advantageous to have the electrode separation much larger than the Debye length to achieve large Seebeck coefficients.

Other quantities, such as the total diffuse charge in the half of the cell near the cold electrode,

$$Q_T(t) = \int_{-L}^0 \rho_c(x, t) dx, \quad (3.24)$$

and the total salt concentration in this same half,

$$C_T(t) = \int_{-L}^0 c(x, t) dx, \quad (3.25)$$

also evolve with a long-time exponentially decaying transient to their steady state, but with different time scales. Using Laplace transforms on these definitions and substituting (3.20), we obtain,

$$\hat{Q}_T(s) = \frac{c_0 \alpha_d}{k^2 L_S} [1 - \operatorname{sech}(kL)] \quad (3.26)$$

$$\hat{C}_T(s) = \frac{c_0 \alpha_m}{r^2 L_S} [1 - \operatorname{sech}(rL)]. \quad (3.27)$$

As before, direct inversion masks physical insights. Thus, in the long-time limit, we obtain

$$Q_T(t) \sim \frac{c_0 \alpha_d}{\kappa^2 L} [1 - \operatorname{sech}(\kappa L)] (1 - e^{-t/\tau_Q}), \quad (3.28a)$$

$$C_T(t) \sim \frac{c_0 \alpha_m L}{2} (1 - e^{-t/\tau_C}), \quad (3.28b)$$

where

$$\tau_Q = \frac{1}{D\kappa^2} \left(1 - \frac{2\kappa L \cosh^2(\kappa L/2)}{\sinh(2\kappa L)} \right), \quad (3.29a)$$

$$\tau_C = \frac{5L^2}{12D}, \quad (3.29b)$$

are the time scales for total diffuse charge and total salt concentration. Clearly, the timescales have different κL dependency than those of the charge density, τ_ρ , and salt concentration, τ_c , at the cold electrode. However, for $\kappa L \gg 1$, the total diffuse charge timescale once again becomes the Debye time, $\tau_Q \sim 1/D\kappa^2$ and for $\kappa L \ll 1$, $\tau_Q \sim L^2/D$, which is identical to the timescales for the charge density at the electrodes, τ_ρ . Note also that the total diffuse charge decreases as κL increases. This reduction in non-zero net charge is what enables the Seebeck coefficient to increase with κL .

3.3 Evolution of Charge, Salt, and Electrostatic Potential

We plot salt concentration, charge density, and electrostatic potential across the cell obtained via numerical inversion of (3.20). The quantities are plotted for $\kappa L = 5$ at times $tD\kappa^2 = 0.01, 0.1, 1$, and 1000, with the final time intended to capture the steady-state profile. In figure 3.4(a), we see the salt slowly diffuses away from the hot electrode toward the cold electrode (for $\alpha_m > 0$). This diffusion begins near the electrodes, and, as the diffuse layers attain equilibrium, extends to the bulk solution until the final linear profile is achieved.

As mentioned in the previous section, for $\alpha_d > 0$, the cations undergo stronger thermal migration than the anions and hence the diffuse layer near the cold electrode obtains a net positive charge, while the diffuse layer near the hot

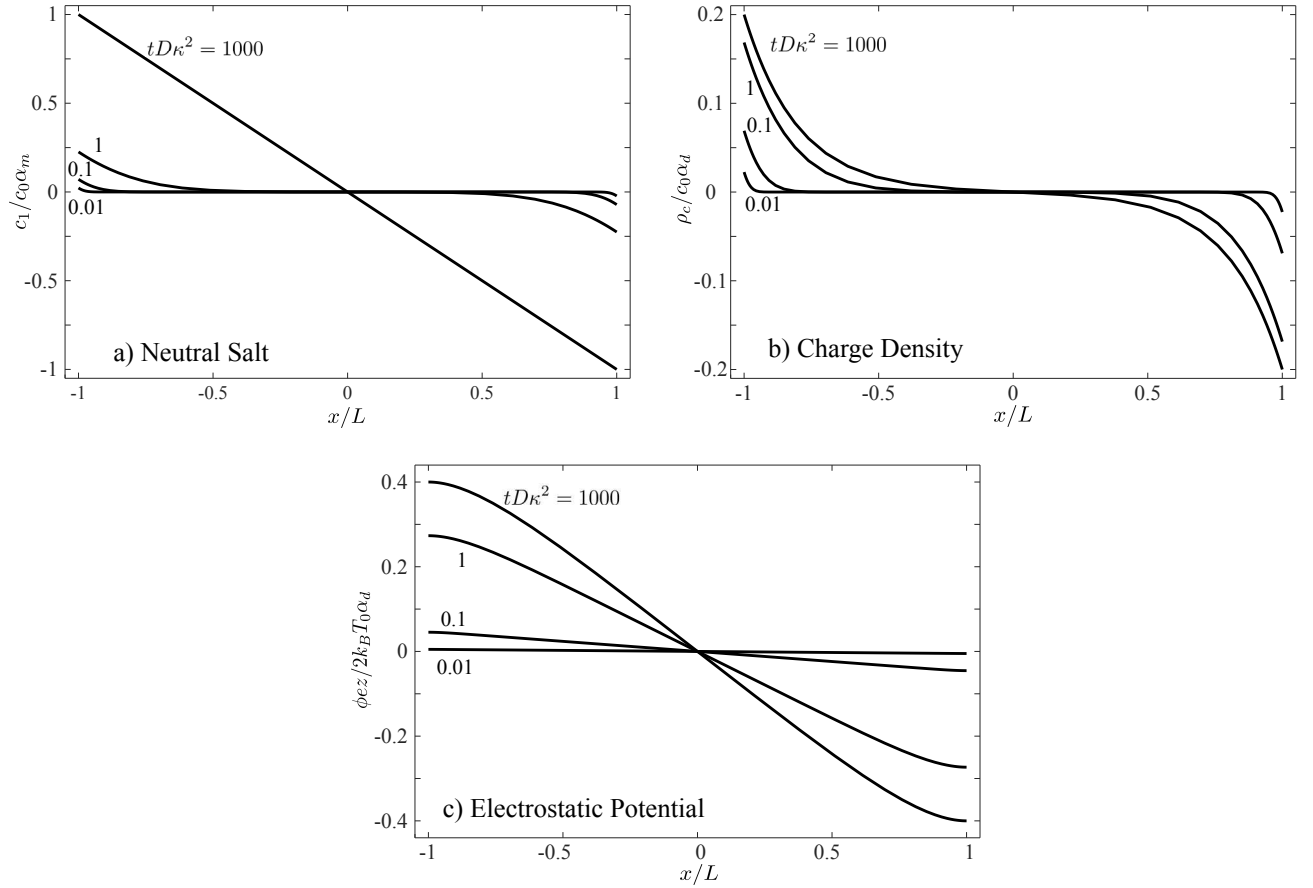


Figure 3.4: Salt concentration (a), charge density (b), and electrostatic potential (c), across the cell at $tD\kappa^2 = 0.01, 0.1, 1$, and 1000 at $\kappa L = 5$. The heated electrode is located at $x/L = 1$ and the cold electrode at $x/L = -1$. At steady state ($tD\kappa^2 \approx 1000$), the neutral salt has a linear profile and the electrostatic potential is linear only in the bulk solution, away from the net charge of the diffuse layers.

electrode obtains a net negative charge, as shown in figure 3.4(b). Compared to the neutral salt, the diffuse layers are much nearer to their equilibrium state by $tD\kappa^2 \approx 1$. This suggests, surprisingly, that the majority of ion transport occurs *after* diffuse layer charging has occurred. This is similar to what has been predicted under a suddenly applied voltage [59], where there exists an initial salt depletion zone near the electrodes as the diffuse layers form for applied voltages greater than the thermal voltage, $k_B T/e$. These depletion zones are then filled on the diffusion time scale L^2/D . The difference here is that for an applied temperature difference, diffuse layers charge on the time

scale $1/D\kappa^2$, whereas for an applied potential difference, the charging time scale is $L/D\kappa$.

Finally, figure 3.4(c) shows that the electrostatic potential is linear in the bulk solution, indicating a uniform induced electric field exists there. Near the electrodes, the electric field is screened by the non-zero net charge within the diffuse layers, leading to a nonlinear profile.

Note that both charge density and electrostatic potential share the same sign across the cell. This is distinctly different from the situation observed for an applied voltage, in which the electrostatic potential and charge density have opposite signs, and is a consequence of the dynamics being driven by a temperature gradient. For instance, consider an electrolyte for which $\alpha_d > 0$: then, the net negative charge density at the hot electrode is driven toward the cold electrode by the electromigrative force (negative potentials in figure 3.4(c)) together with the thermal migration. This is balanced by the diffusive flux, which acts to equalize the salt concentration across the entire cell. Similarly, at the cold electrode (net charge is positive), the diffusive flux and electromigration (toward the hot electrode) are balanced by the thermal migration (toward the cold electrode).

3.4 Conclusions

We have provided a detailed derivation of the charging dynamics of an ionic thermo-electric system, starting from the fundamental ion transport equations for dilute electrolytes. We assumed a weak temperature gradient and defined a parameter to reflect this, $\delta = G_f 2L/T_0 \ll 1$, which sets a condition on the temperature difference: $\Delta T \ll T_0$. This condition can allow for rather large temperature differences provided the initial temperature of the device is appropriately chosen.

We predict the thermo-voltage and diffuse layers develop on the order of the Debye time, $1/D\kappa^2$, for thin diffuse layers, $\kappa L \gg 1$. In this regime, the Debye time is much shorter than both the diffusion time, L^2/D , over which the linear salt concentration profile develops, and the RC time, $L/D\kappa$, which is relevant for the related problem of a suddenly applied voltage in an isothermal system. As an example, consider that a 1 mM aqueous electrolyte solution has a Debye length of $1/\kappa \approx 10$ nm; then, assuming $D = 10^{-5}$ cm²/s and $L = 1$ mm yields $\kappa L \approx 10^5$, and $L^2/D = 10^3$ s, while $1/D\kappa^2 \approx 10^{-7}$ s. This implies that the thermo-voltage (and diffuse layers) develop extremely quickly as the device charges under a temperature gradient. However, salt diffusion due to the temperature gradient is much slower.

This conclusion appears at odds with experimental results which show charging times on the order of hundreds to thousands of seconds [13, 14, 15]. Although these experiments involve non-aqueous charge carriers, the Debye length is still $O(\text{nm})$ and $L \sim O(\text{mm})$. From our calculations, charging times that are $O(100$ s) would require unreasonably small diffusivities for the charge carriers. We therefore conclude that the thermo-charging of the devices in those experiments is limited by how quickly the electrodes can be heated. That is, if we accounted for the time dependent heating of the electrode, the rate determining timescale would be the heating timescale or a combination of charging and heating time scales.

Another factor which could affect the charging timescales is relaxing our assumption of equal Brownian diffusion coefficients for the two ion species. In experiments [13, 14, 15], one species is a large polymer molecule and diffuses much more slowly relative to the other, hence unequal Brownian diffusion coefficients would be a more accurate representation of the physical systems. Furthermore, the time scales for salt diffusion, diffuse charge, and thermo-voltage, would necessarily have different limiting values for thin diffuse layers,

but the magnitude of the thermo-voltage might not be affected for weak temperature gradients, as only the Soret coefficients determine its magnitude.

In addition, we have considered only the first order effects of a weak temperature gradient. To this order, all thermal dependency exists only in the boundary conditions and hence the Soret coefficients do not appear in the charging time scales. Perhaps beyond this weak gradient regime, the Soret coefficients play a greater role in the dynamics of the system, as opposed to merely determining the magnitude of the steady state thermo-voltage. One expected outcome is that the Seebeck coefficient will depend on the magnitude of the temperature gradient, i.e. a “nonlinear” Seebeck coefficient. We will examine this issue in future work.

Chapter 4

A Continuum Approach to Predicting Electrophoretic Mobility Reversals

4.1 Introduction

Electrophoresis refers to the motion of a charged colloidal-scale particle in an electrolytic solution under an applied electric field. Electrophoretic transport is used extensively in analytical chemistry [77], microfluidics [49], and DNA sequencing [78]. A central quantity of interest is the electrophoretic mobility, which relates the migrative velocity of a charged particle, \mathbf{U} , to the uniform applied field, \mathbf{E}_∞ . The electrophoretic mobility for a uniformly charged spherical colloid is a scalar quantity (M_e), such that $\mathbf{U} = M_e \mathbf{E}_\infty$ [19].

Charged surfaces and particles in electrolytic solutions attract a diffuse region of net charge around them - a ‘Debye layer.’ In dilute solutions, the thickness of this layer is characterized by the Debye length, κ^{-1} : for a binary electrolyte $\kappa^{-1} = \sqrt{\varepsilon k_B T / e^2 n_+^\infty z_+(z_+ - z_-)}$, where ε is the dielectric permittivity, k_B is the Boltzmann constant, T is temperature, e is the fundamental charge, n_+^∞ is the bulk number density of counter-ions, and z_+ and z_- are the charge numbers of the counter- and co-ions, respectively, assuming a nega-

tively charged surface. For a 1 mM monovalent salt at $T = 298\text{K}$, $\kappa^{-1} \approx 10$ nm. Thus, for a colloidal particle of radius $R \sim O(\mu\text{m})$, $\kappa R \gg 1$ and the Debye layer is said to be ‘thin.’

In this thin-Debye-layer limit, $M_e = \varepsilon\zeta/\eta$ (where η is solution viscosity) as shown by Smoluchowski [79] for a uniformly charged, dielectric, spherical particle with a surface ‘zeta’ potential (ζ) that is small compared to the thermal voltage, $k_B T/e \simeq 25$ mV. Hückel [80] predicted $M_e = 2\varepsilon\zeta/3\eta$ for thick-Debye-layers ($\kappa R \ll 1$). These limits were bridged by Henry [81], who calculated a monotonic increase in the magnitude of M_e with increasing κR . Importantly, M_e remains the same sign with varying κR for a fixed sign of ζ . For example, a negatively charged particle ($\zeta < 0$) has $M_e < 0$ for any κR and thus moves against \mathbf{E}_∞ (to higher potentials).

O’Brien and White [82] numerically solved the Poisson-Nernst-Planck (PNP) equations for point-like non-interacting ions to compute M_e over a wide range of ζ and κR . For $\kappa R \gg 1$ and $\zeta > 0$, M_e initially increases linearly with ζ according to Smoluchowski’s result, then attains a maximum value for $\zeta \approx (5 - 10)k_B T/e$ and subsequently decreases to a finite value as $\zeta \rightarrow \infty$ (see also [83, 84]). More precisely, Smoluchowski’s result holds until $\zeta \sim O[(k_B T/e) \ln(\kappa R)]$ [85]. The departure from Smoluchowski’s prediction arises from surface conduction of ions in the Debye layer as a consequence of the exponentially large counter-ion concentration predicted by the PNP model at moderately large ζ . Khair and Squires [28] showed that surface conduction can be reduced, and hence the mobility maximum delayed to unphysically large ζ , by inclusion of steric hindrance between finite sized ions using Bikerman’s model [26, 27, 86]. Nonetheless, M_e retains the same sign with varying κR for a fixed sign of ζ .

However, ‘mobility reversals’ have been observed in experiments involving multivalent electrolytes with increasing salt concentration [35, 36, 37, 38,

87, 88]. For example, at low ionic strength (small κR) a negatively-charged particle ($\zeta < 0$) has $M_e < 0$ and migrates against \mathbf{E}_∞ (to higher potentials). As ionic strength increases, M_e crosses zero and becomes positive - the particle migrates with \mathbf{E}_∞ (to lower potentials). The above mentioned theories lack a key physical trait for capturing mobility reversals. Here, we present a continuum framework capable of predicting electrophoretic mobility reversals.

Concentrated electrolytes are known to exhibit ‘overscreening,’ where the charge on a surface is overcompensated by a first layer of counter-ions, that first layer is overcompensated by a second layer consisting of co-ions and so on; the ionic charge density oscillates in sign away from the surface [25]. A purported cause of overscreening is ion-ion electrostatic (Coulomb) correlations, beyond mean-field Debye screening [89, 90]. Molecular Dynamics (MD) and Monte Carlo (MC) simulations [91, 92], integral equation approaches [87, 93, 94, 95, 96], and density functional and statistical field theories [24, 97, 98] have predicted overscreening in equilibrium Debye layers. These techniques often adopt the primitive model of electrolytes as charged hard spheres in a dielectric continuum. Although they offer an accurate picture of the equilibrium Debye layer around simple geometries such as a flat plate or sphere, calculation of electrophoretic mobility is challenging since the Debye layer is driven away from equilibrium by the imposed electric field. Martín-Molina *et. al.* [99] calculated the mobility of a spherical colloid using Smoluchowski’s formula with ζ determined from an MC simulation for a flat plate that included Coulombic potentials for ion-ion and ion-wall interactions. Lozada-Cassou *et al.* [100] used the weak-field linearization of O’Brien and White [82] along with an integral equation description of the equilibrium Debye layer around a spherical particle. Raafatnia *et. al.* [39] also utilized the weak-field linearization combined with MD simulation of the equilibrium Debye layer over a flat plate. While these approaches can predict electrophoretic mobility

reversals, the first [99] does not account for surface conduction, and all three can become computationally intensive in complex geometries. Our approach below utilizes an entirely continuum framework, which could be applied to a wide range of particle geometries and is not restricted to the thin-Debye-layer limit.

Bazant *et. al.* [67] recently derived a modified Poisson equation (MPE) to capture ion-ion electrostatic correlations in equilibrium Debye layers (see also [23, 24]). The MPE introduces a correlation length, ℓ_c , which is expected to be bounded from below by the ion diameter, a , and from above by $z_+^2 \ell_B$, where $\ell_B = e^2/4\pi\epsilon k_B T$ is the Bjerrum length that signifies the distance at which electrostatic energy between a pair of monovalent ions equals thermal energy; in water, $\ell_B \approx 0.7\text{nm}$. Ions separated by a distance greater than ℓ_c predominantly experience mean-field (screened) electrostatics; ions closer than ℓ_c experience (Coulombic) electrostatic correlations. The MPE reads $\epsilon(\ell_c^2 \nabla^4 \varphi - \nabla^2 \varphi) = \rho$, where φ is the electrostatic potential and $\rho = e(z_+ n_+ + z_- n_-)$ is the ionic charge density with n_+ and n_- as the number density of cations and anions, respectively. As suggested by [67], the MPE can be interpreted in terms of a permittivity operator $\hat{\epsilon} = \epsilon(1 - \ell_c^2 \nabla^2)$ resulting from non-local dielectric responses of correlated ion pairs. The MPE can predict overscreening and an electro-osmotic flow reversal over a flat plate [22].

In section 4.2, we utilize the MPE to compute the mobility of a weakly charged (small ζ) particle. In section 4.3, we compute the mobility at larger ζ , using the MPE to describe electrostatic correlations and Bikerman's model to capture steric hindrance between ions. Conclusions are offered in section 4.4.

4.2 Electrophoretic Mobility: Small Zeta Potentials

Consider a uniformly charged spherical colloid of radius R in a binary electrolyte. The charge density $\rho \approx -e^2 n_+^\infty z_+(z_+ - z_-)\varphi/k_B T$ for $|\zeta| \lesssim k_B T/e$. Normalizing ρ by $z_+ e n_+^\infty$ and φ and ζ by $k_B T/e$, we obtain $\tilde{\rho} = -(z_+ - z_-)\tilde{\varphi}$, where we use a tilde to denote the dimensionless counterpart of a dimensional quantity. Radial distance, r , from the center of the colloid is scaled by R and the dimensionless correlation length is $\delta_c = \ell_c \kappa$. The MPE thus reduces to a modified Debye-Hückel equation (for $\delta_c = 0$, the standard Debye-Hückel equation is recovered),

$$(\kappa R)^2 \tilde{\nabla}^2 \tilde{\varphi} - \delta_c^2 \tilde{\nabla}^4 \tilde{\varphi} = (\kappa R)^4 \tilde{\varphi}. \quad (4.1)$$

As in [67] and [22], $\tilde{\varphi}$ and its derivatives vanish as $\tilde{r} \rightarrow \infty$; $\tilde{\varphi} = \tilde{\zeta}$ and $\hat{\mathbf{n}} \cdot \tilde{\nabla}(\tilde{\nabla}^2 \tilde{\varphi}) = 0$ at $\tilde{r} = 1$, where $\hat{\mathbf{n}}$ is the unit vector normal to the surface. This last boundary condition assumes that correlations at the particle surface are negligible and yields predictions in agreement with molecular simulations [22, 67, 101].

Since the equilibrium potential is spherically symmetric, let $\tilde{\varphi} = \tilde{\zeta} f(\tilde{r})/\tilde{r}$. Thus, (4.1) reduces to $(\kappa R)^2 f'' - \delta_c^2 f'''' = (\kappa R)^4 f$, where primes denote derivatives in \tilde{r} . An analytical solution is readily obtained whose features are similar to the solution over a charged plate [22]. Two distinct solutions exist based on the value of δ_c . For $\delta_c < 1/2$ (“weak correlations”) we arrive at

$$f(\tilde{r}) = A e^{-n_1(\tilde{r}-1)} + (1 - A) e^{-n_2(\tilde{r}-1)}, \quad (4.2a)$$

where

$$n_1 = \frac{\kappa R}{\delta_c} \sqrt{\frac{1 + \sqrt{1 - 4\delta_c^2}}{2}}, \quad n_2 = \frac{\kappa R}{\delta_c} \sqrt{\frac{1 - \sqrt{1 - 4\delta_c^2}}{2}}, \quad (4.2b)$$

$$A = \frac{n_2^2(n_2 + 1)}{n_2^2(n_2 + 1) - n_1^2(n_1 + 1)},$$

and for $\delta_c > 1/2$ (“strong correlations”) we arrive at

$$f(\tilde{r}) = e^{-k_1(\tilde{r}-1)} [\cos(k_2(\tilde{r}-1)) + B \sin(k_2(\tilde{r}-1))], \quad (4.3a)$$

where

$$k_1 = \kappa R \frac{\sqrt{2\delta_c + 1}}{2\delta_c}, \quad k_2 = \kappa R \frac{\sqrt{2\delta_c - 1}}{2\delta_c}, \quad B = \frac{k_1^2(k_1 + 1) - k_2^2(3k_1 + 1)}{k_1 k_2 (3k_1 + 2) - k_2^3}. \quad (4.3b)$$

For weak correlations (4.2), $f(\tilde{r})$ is the sum of exponentially decaying terms, resulting in a potential whose decay is monotonic with increasing \tilde{r} yet predicts a greater potential near the surface than the case of $\delta_c = 0$. For strong correlations (4.3), the potential has decaying oscillations, signifying charge inversion and stronger overscreening. From the definition of k_1 and k_2 in (4.3b) it is seen that $\sqrt{\ell_c/\kappa}$ is a more appropriate length scale to characterize charge density variation in a Debye layer with strong electrostatic correlations.

Figure 4.1 shows the dimensionless charge density $\tilde{\rho}$ versus \tilde{r} for four combinations of κR and δ_c . For $\delta_c = 0$ and $\kappa R = 10$, $\tilde{\rho}$ decays monotonically to zero with increasing \tilde{r} . For $\delta_c = 5$ and $\kappa R = 10$, $\tilde{\rho}$ is larger (compared to $\delta_c = 0$) near the surface, indicating overscreening. To balance this excess counter-ion charge, co-ions are brought into the Debye layer and result in charge inversion - net negative charge density ($\tilde{\rho} < 0$) - seen at $\tilde{r} \sim 1.5$. At $\kappa R = 50$, a smaller Debye length, the same trend is observed although the charge density decays more rapidly with \tilde{r} .

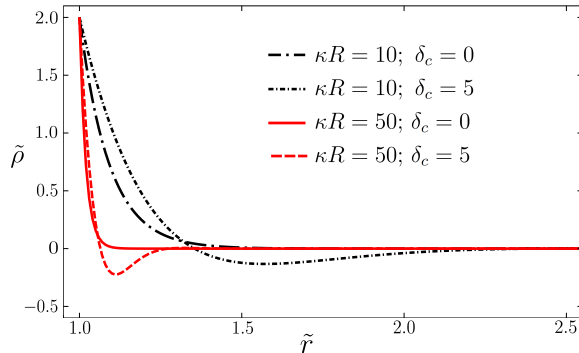


Figure 4.1: Dimensionless charge density, $\tilde{\rho}$, calculated from (4.1) for a monovalent electrolyte around a negatively-charged sphere with $|\tilde{\zeta}| \lesssim 1$. Ion-ion electrostatic correlations ($\delta_c = 5$) lead to overscreening and charge oscillations.

4.2.1 Electrophoretic Mobility

An applied electric field, \mathbf{E}_∞ , sets the colloid into motion with an electrophoretic velocity \mathbf{U} . For small zeta potentials, $|\tilde{\zeta}| \lesssim 1$, polarization of the Debye layer can be neglected to a first approximation [19]. Hence, the imposed field exerts an electrical force $\mathbf{F}_E = Q\mathbf{E}_\infty$ on the colloid, where $Q = 4\pi R\epsilon\zeta [f(1) - f'(1)]$ is the colloid surface charge. This expression for Q follows from the modified electrostatic boundary condition $\hat{\mathbf{n}} \cdot \mathbf{D} = q$, where $\mathbf{D} = -\hat{\epsilon}\nabla\phi$ is the displacement field and q is the surface charge density, and the assumption $\hat{\mathbf{n}} \cdot \nabla(\nabla^2\phi) = 0$ at the particle surface [67]. The fluid within the Debye layer undergoes an electro-osmotic flow, imparting a hydrodynamic force on the colloid, $\mathbf{F}_O = \int \rho\mathbf{P} \cdot \mathbf{E}dV$, where $\mathbf{E} = [(1 + R^3/2r^3)\mathbf{I} - (3R^3/2r^3)\hat{\mathbf{r}}\hat{\mathbf{r}}] \cdot \mathbf{E}_\infty$ is the field around the insulating particle, $\mathbf{P} = (3R/4r + R^3/4r^3)\mathbf{I} + (3R/4r - 3R^3/4r^3)\hat{\mathbf{r}}\hat{\mathbf{r}}$ (\mathbf{I} is the identity tensor and $\hat{\mathbf{r}}$ is a radial unit vector), and the integral is over the electrolyte volume. Note, the expression for \mathbf{F}_O is derived using the Lorentz reciprocal theorem in which the primary flow of interest is that due to a body force density $\rho\mathbf{E}$, resulting in the hydrodynamic force \mathbf{F}_O on the colloid. The secondary flow in the reciprocal theorem is that due to an uncharged sphere translating at unit velocity, for which the tensor \mathbf{P} relates the

fluid velocity field to the velocity of the particle (see, e.g., [102]). The migration of the colloid results in a drag force, $\mathbf{F}_D = -6\pi\eta R\mathbf{U}$. Since the colloid is freely suspended, \mathbf{F}_E , \mathbf{F}_O , and \mathbf{F}_D sum to zero; hence $\mathbf{U} = M_e\mathbf{E}_\infty$ and the dimensionless mobility, $\tilde{M}_e = 3\eta M_e/2\varepsilon\zeta$, is given by

$$\tilde{M}_e = -\frac{d}{d\tilde{r}} \left(\frac{f}{\tilde{r}} \right) \Big|_{\tilde{r}=1} - (\kappa R)^2 \int_1^\infty f(\tilde{r}) \left(1 - \frac{1}{4\tilde{r}^3} + \frac{1}{4\tilde{r}^5} \right) d\tilde{r}, \quad (4.4)$$

where the first term in (4.4) is a measure of the electrical force, \mathbf{F}_E , and the second term represents the electro-osmotic force, \mathbf{F}_O . After substituting the expressions for f given by (4.2)-(4.3) into (4.4), we obtain, for $\delta_c < 1/2$,

$$\tilde{M}_e = (1 + A(n_1 - n_2) + n_2) - (\kappa R)^2 (AG_1 + (1 - A)G_2), \quad (4.5a)$$

where

$$G_x = \frac{1}{n_x} + \frac{e^{n_x}}{4} (E_5(n_x) - E_3(n_x)), \quad (4.5b)$$

and for $\delta_c > 1/2$

$$\tilde{M}_e = (1 + k_1 - Bk_2) - \frac{(\kappa R)^2}{2} [(1 - Bi)H_1 + (1 + Bi)H_2], \quad (4.6a)$$

where

$$H_x = \frac{1}{m_x} + \frac{e^{m_x}}{4} (E_5(m_x) - E_3(m_x)). \quad (4.6b)$$

Here, $E_a(z) = \int_1^\infty e^{-z\tilde{r}}/\tilde{r}^a d\tilde{r}$ is the exponential integral, $m_1 = k_1 - ik_2$, $m_2 = k_1 + ik_2$, and $i = \sqrt{-1}$. Note that $E_a(z) = z^{a-1}\Gamma_u(1-a, z)$, where $\Gamma_u(v, z) = \int_z^\infty e^{-\tilde{r}}\tilde{r}^{v-1} d\tilde{r}$ is the upper incomplete Gamma function. In (4.5b) and (4.6b) the subscript x stands for either index 1 or 2. Despite the appearance of the imaginary unit in (4.6), the computed mobility is of course still real.

Because \tilde{M}_e is normalized by ζ , reversals in mobility are signified by $\tilde{M}_e < 0$. The mobility is shown in figure 4.2 versus κR for various δ_c . For

$\delta_c = 0$, \tilde{M}_e increases monotonically from 1 to 1.5 with increasing κR [81]. For a negatively charged colloid (inset to figure 4.2), \mathbf{F}_E is directed against the field and \mathbf{F}_O is with the field (due to positive charge density in the Debye layer). There is an imbalance, $|\mathbf{F}_E| > |\mathbf{F}_O|$, so \mathbf{F}_D must be with the field to balance the forces; thus, the particle migrates against the field: $\tilde{M}_e > 0$. As δ_c is increased at fixed κR (say $\kappa R = 10$ in figure 4.2), Q decreases and consequently the total charge in the diffuse layer, $\int \tilde{\rho} d\tilde{V}$, decreases despite the overscreening causing more ions to be present. The lower Q and reduced diffuse charge result in lower $|\mathbf{F}_E|$ and $|\mathbf{F}_O|$, respectively. More precisely, $|\mathbf{F}_O|$ decreases due to a reduction in local charge density within the Debye layer by excess co-ions (figure 4.1), and hence a locally reduced electro-osmotic flow. (The no-slip condition prevents the excess counter-ions near the surface from driving a comparably enhanced electro-osmotic flow). The rate of decrease of $|\mathbf{F}_O|$ and $|\mathbf{F}_E|$ are unequal, and $|\mathbf{F}_E| < |\mathbf{F}_O|$ for sufficiently large δ_c , in which case \mathbf{F}_D points against the applied field. This switch in \mathbf{F}_D is an electrophoretic mobility reversal, $\tilde{M}_e < 0$: a negatively charged colloid moves with the applied field. For thick Debye layers ($\kappa R \rightarrow 0$), \tilde{M}_e is independent of δ_c since the charge density becomes vanishingly small. Note that $\tilde{M}_e > 0$ for $\delta_c = 1.5$; thus, overscreening and charge oscillation do not necessarily lead to mobility reversals. Importantly, Q is not zero when $\tilde{M}_e = 0$; the mobility reversal does not coincide with the point of zero particle charge. Another example where the point of zero charge does not coincide with zero mobility is the non-zero induced-charge electrophoretic mobility of an uncharged metal particle under a uniform electric field in an asymmetric electrolyte [2].

Figure 4.3 compares the mobility from (4.5)-(4.6) with experimental results of [35], who utilized optical tweezers to measure the electrophoretic velocity of a single polystyrene sulphonate latex colloid with a diameter of 2.23 μm . The colloid surface charge density was found by acid-base titration to

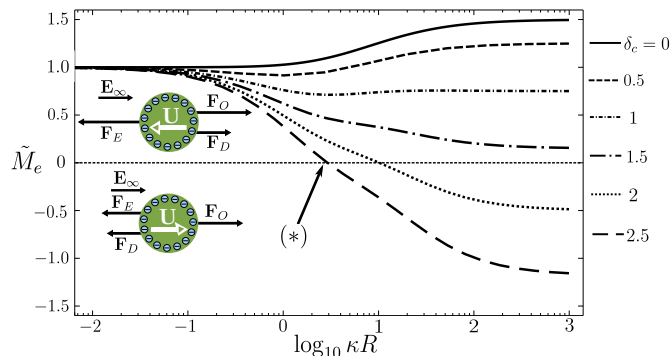


Figure 4.2: Electrophoretic mobility, $\tilde{M}_e = 3\eta M_e / 2\varepsilon\zeta$, versus κR for various δ_c at small $\tilde{\zeta}$. Insets illustrate direction and relative magnitudes of electrical (\mathbf{F}_E), electro-osmotic (\mathbf{F}_O), and drag (\mathbf{F}_D) forces on a spherical colloid for $\tilde{M}_e > 0$ and $\tilde{M}_e < 0$ (reversals). At point (*) along the $\delta_c = 2.5$ curve, $\kappa R = 2.92$, and the mobility is close to zero, $\tilde{M}_e = 0.00020$, while the charge is of order unity $Q/4\pi R\varepsilon\zeta = 2.72$. Thus, the points of zero charge and zero mobility do not coincide.

be $-0.31\mu\text{C}/\text{cm}^2$ and is taken as constant at all concentrations. Experiments were performed in binary monovalent (KCl), divalent (CaCl_2), and trivalent (LaCl_3) salts; only the trivalent salt showed a mobility reversal. We chose the correlation length, ℓ_c , to best match the mobility in the high concentration region for the mono and divalent electrolytes, and to best match the concentration at which the mobility is zero in the trivalent electrolyte. For KCl and CaCl_2 , $\ell_c = 0$. For LaCl_3 , $\ell_c = 3.07$ nm, leading to $\delta_c = 0.03$ at the lowest ionic strength (0.01 mM, $\kappa R \sim 10$) and $\delta_c = 10.10$ at the highest (1 M, $\kappa R \sim 3500$). This estimate of ℓ_c falls within the expected bounds of hydrated counter-ion diameter (0.49 nm) [103] and $z_+^2 \ell_B$ (6.4 nm) for LaCl_3 . It is remarkable that our simple analytical theory can capture the mobility reversal with a physically realistic value of ℓ_c . However, the theory overestimates $|M_e|$ at low ionic strengths. For LaCl_3 we predict $\tilde{\zeta} \approx -0.42$ at the reversal ($M_e = 0$), which is a suitably small zeta potential. At ionic strengths lower than $O(1 \text{ mM})$, $|\tilde{\zeta}|$ is sufficiently larger than unity to invalidate the small zeta potential theory.

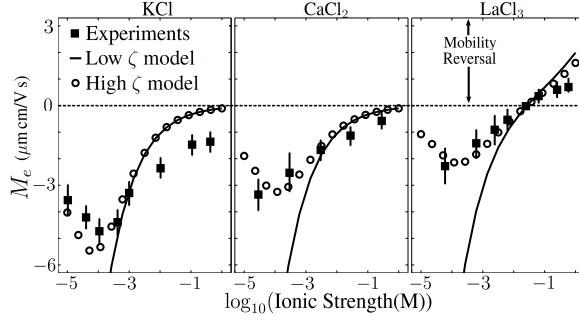


Figure 4.3: Theoretical predictions compared with experimental data taken from figure 5a of [35] (squares).

4.3 Mobility at Larger Zeta Potentials

At larger $\tilde{\zeta}$, the applied field results in polarization of the Debye layer through ionic surface conduction. At the larger concentrations used in the experiments, surface conduction is expected to be mitigated by steric hindrance between ions [28]. Hence, we employ Bikerman’s model [86], such that the electrochemical potential μ_{\pm} , scaled by $k_B T$, of each ion species is $\tilde{\mu}_{\pm} = z_{\pm} \tilde{\varphi} + \ln n_{\pm} - \ln [1 - a^3(n_+ + n_-)]$, where the first two terms are for an ideal solution, and the third term represents steric hindrance. The role of sterics is controlled by the bulk volume fraction of ions $\nu = a^3(n_+^{\infty} + n_-^{\infty})$, using a single ion size a (specified later). At equilibrium, $\tilde{\nabla} \tilde{\mu}_{\pm} = 0$, which gives an explicit relationship between $\tilde{\varphi}$ and \tilde{n}_{\pm} (the latter scaled by n_{\pm}^{∞}) [26] that is combined with the MPE to yield a “Poisson-Fermi” equation (PFE) [67] governing the equilibrium electrostatic potential,

$$\delta_c^2 \tilde{\nabla}^4 \tilde{\varphi} - (\kappa R)^2 \tilde{\nabla}^2 \tilde{\varphi} = (\kappa R)^4 \beta(\tilde{\varphi}) \frac{e^{-z_+ \tilde{\varphi}} - e^{-z_- \tilde{\varphi}}}{z_+ - z_-}, \quad (4.7a)$$

where

$$\beta(\tilde{\varphi}) = \left(1 - \nu + \frac{\nu(z_+ e^{-z_- \tilde{\varphi}} - z_- e^{-z_+ \tilde{\varphi}})}{z_+ - z_-} \right)^{-1}. \quad (4.7b)$$

Figure 4.4 shows the dimensionless charge density, $\tilde{\rho} = \beta(e^{-z_+ \tilde{\varphi}} - e^{-z_- \tilde{\varphi}})$, computed from (4.7) for a monovalent electrolyte at $\kappa R = 10$ and $\nu = 0.1$, for

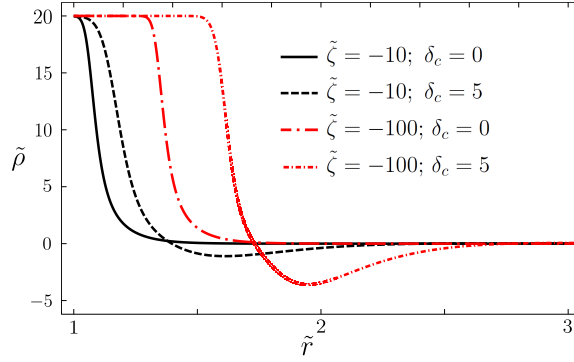


Figure 4.4: Dimensionless charge density $\tilde{\rho}$ of a monovalent electrolyte around a negatively-charged sphere with $\kappa R = 10$ and bulk volume fraction $\nu = 0.1$. The counter-ions form an overscreening condensed layer, followed by a region of charge inversion due to co-ions. The extents of both grow with $|\tilde{\zeta}|$.

$\tilde{\zeta} = -10$ and -100 . At such large $\tilde{\zeta}$, the counter-ions form a condensed layer at the surface due to steric hindrance. With correlations ($\delta_c \neq 0$), the condensed layer overscreens the surface charge and extends further from the surface, despite the Debye length remaining unchanged. The degree of overscreening by counter-ions and charge inversion due to co-ions increases with $\tilde{\zeta}$.

4.3.1 Electrophoretic Mobility: Thin-Debye-Layer

Analysis

The electrolyte dynamics in response to a weak applied field are described by coupled linear equations governing the perturbations to the equilibrium electrochemical potentials, $\tilde{\mu}_{\pm}^1$, and fluid velocity, $\tilde{\mathbf{v}}^1$. The superscripts 0 and 1 indicate quantities that are zeroth or first order in the applied field (they are not meant to represent algebraic powers). These equations are well known and read [28, 82, 84]

$$\tilde{\nabla}^2 \tilde{\mu}_{\pm}^1 + \tilde{\nabla} \ln \tilde{n}_{\pm}^0 \cdot \tilde{\nabla} \tilde{\mu}_{\pm}^1 = \frac{1}{2} m \tilde{\mathbf{v}}^1 \cdot \tilde{\nabla} \ln \tilde{n}_{\pm}^0 \quad (4.8a)$$

$$\tilde{\nabla}^2 (\tilde{\nabla} \times \tilde{\mathbf{v}}^1) = \frac{(\kappa R)^2}{\mathcal{Z}} \left(\tilde{\nabla} \tilde{n}_+^0 \times \tilde{\nabla} \tilde{\mu}_+^1 + \tilde{\nabla} \tilde{n}_-^0 \times \tilde{\nabla} \tilde{\mu}_-^1 \right), \quad (4.8b)$$

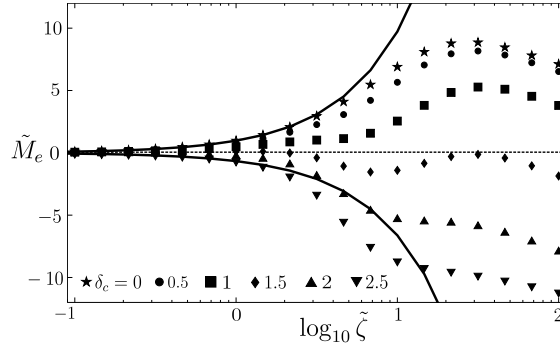


Figure 4.5: Dimensionless electrophoretic mobility, $\tilde{M}_e = \eta M_e / \varepsilon (k_B T / e)$, versus $\tilde{\zeta}$ for various δ_c with $\kappa R = 100$ and $\nu = 0.1$. Symbols are from solution of the large $\tilde{\zeta}$ model (4.7) - (4.8), and the lines are from the small $\tilde{\zeta}$ formulae (4.5)-(4.6) with $\delta_c = 0$ (top) and 2.5 (bottom).

where $\mathcal{Z} = z_+(z_+ - z_-)$, and $\tilde{n}_+^0 = \beta e^{-z_+ \tilde{\varphi}}$ and $\tilde{n}_-^0 = -\frac{z_+}{z_-} \beta e^{-z_- \tilde{\varphi}}$ are the equilibrium cation and anion density, respectively, calculated from (4.7). The velocity field $\tilde{\mathbf{v}}^1$ is normalized by $\varepsilon (k_B T / e)^2 / \eta R$, and $m = 2\varepsilon (k_B T / e)^2 / \eta D$, with D a single ionic diffusion coefficient (specified later). Equation (4.8a) embodies ion conservation and equation (4.8b) governs the inertialess fluid flow with an electrochemical body force. Recall, the experiments [35] have $\kappa R \gg 1$. Therefore, a thin-Debye-layer asymptotic analysis is utilized to solve (4.8) and subsequently compute the mobility. The analysis is essentially identical to [28]; details are not repeated here.

Figure 4.5 shows the dimensionless mobility, now defined as $\tilde{M}_e = \eta M_e / \varepsilon (k_B T / e)$, versus $\tilde{\zeta}$ for a positively-charged particle in a monovalent electrolyte at various δ_c , for $\kappa R = 100$ and $\nu = 0.1$; our results agree with [28] for $\delta_c = 0$. The mobility computed from solution of (4.8) is in agreement with (4.5)-(4.6) at small $\tilde{\zeta}$. For $\delta_c = 0, 0.5$, and 1 the mobility does not reverse ($\tilde{M}_e > 0$), and surface conduction reduces the mobility relative to (4.5)-(4.6). A more complicated dependence of \tilde{M}_e on $\tilde{\zeta}$ is observed when δ_c is sufficiently large for a mobility reversal to occur (e.g. $\delta_c = 1.5$).

Comparison of the large ζ theory with experiments [35] is shown in figure

4.3. The ion size a was taken to be the average of the hydrated ion diameters [103], and D is calculated from the conductivity at infinite dilution [104]. Again, $\ell_c = 0$ in KCl and CaCl₂, whereas now $\ell_c = 2.63$ nm for LaCl₃, which is slightly lower than the estimate of 3.07 nm from the low $\tilde{\zeta}$ model. The two models share the same agreement with the experiments at high concentrations, which is not surprising as $|\tilde{\zeta}| \lesssim 1$ there. The large $\tilde{\zeta}$ model predicts $\tilde{\zeta} = -0.36$ at the mobility reversal in LaCl₃, compared to $\tilde{\zeta} = -0.42$ predicted from the low $\tilde{\zeta}$ model. Notably, the large $\tilde{\zeta}$ model shows better agreement to the experiments at lower concentration. Thus Debye layer polarization must be accounted for to predict the mobility over a wide range of concentrations.

While we have included ion sterics through Bikerman's model, we note that it has little effect on the predicted mobility in figure 4.3 since when $|\tilde{\zeta}|$ is large enough to anticipate a reduction in surface conduction, the volume fraction, ν , is small due to the low ionic strength. Conversely, at higher ionic strengths when $\nu \sim O(0.1)$, $|\tilde{\zeta}| \lesssim 1$ and a condensed counter-ion layer does not form. Hence, we conclude that accounting for surface conduction is sufficient to improve agreement for large $|\tilde{\zeta}|$, at least for this range of concentrations and for these ions. Nevertheless, by accounting for correlations through the MPE, the prediction of electrophoretic mobility reversals is possible in both models.

4.4 Conclusions

A continuum framework to predict electrophoretic mobility reversals in concentrated multivalent electrolytes has been presented which incorporates ion-ion electrostatic correlations and steric hindrance between ions. Of course, additional effects are expected in concentrated systems, including local variations in viscosity and permittivity in the Debye layer [2], and variation in bulk

permittivity due to ion-specific polarizability [105]. Recognize, however, that electrostatic correlations are the essential driver of mobility reversals. Raafatnia [39] utilized an attraction energy of $4k_B T$ between counter-ion and colloid surface to predict the observed mobility reversals in LaCl_3 [35]. In contrast, our work demonstrates that mobility reversals can be predicted solely from consideration of electrostatic ion-ion correlations in the diffuse Debye layer. Finally, the present approach can be adapted to predict a host of other electrokinetic phenomena in concentrated solutions, including dynamic (AC) electrophoresis, induced-charge electrophoresis, diffusiophoresis, and dielectrophoresis.

Chapter 5

Influence of Ion Sterics on Diffusiophoresis and Electrophoresis in Concentrated Electrolytes

5.1 Introduction

Electrophoresis is the motion of a charged colloidal particle under the influence of an electric field in an electrolyte solution [19]. Diffusiophoresis is the motion of a colloidal particle brought about by a concentration gradient of solute molecules that interact with the particle's surface via a long-ranged interaction potential [40, 106]. For charged solute molecules (e.g. ions), the difference in diffusivities of the ions induces an electric field, which for a charged colloid produces electrophoretic motion. The excess of ions adjacent to the charged surface due to electrostatic attraction, together with the concentration gradient, result in so-called chemiphoresis [40, 107, 108]. These two effects can support or counteract each other, depending on electrolyte species and particle zeta potential [40]. The sum of these effects is called diffusiophoresis. For non-electrolyte solute molecules, diffusiophoresis is similar in nature [40, 106, 108], although generally weaker due to the absence of an induced electric field, mak-

ing it difficult to observe in experiments [109]. In this case, the interaction between particle and solute is via Van der Waals or other interaction potentials [106, 110, 111]. In this chapter, we focus on diffusiophoresis in an electrolyte solution. Due to the similarities between diffusiophoresis and electrophoresis, we will keep the mathematical treatment general so it can be applied to both phenomena.

Diffusiophoresis was first described by Derjaguin *et al.* in 1947 [107], while electrophoresis has been known since (at least) the pioneering work of Smoluchowski in 1903 [79]. Electrophoresis is used extensively in microfluidics [49] and particle separation techniques [77, 78]. Diffusiophoresis, on the other hand, has been slow to gain recognition of its impact on systems outside of laboratory settings. Nevertheless, recognition is increasing in applications of porous membrane filtration [112, 113], flows in dead-end pores [114], focusing and spreading of particles [114, 115], and detection and repair of cracks [116, 117]. See [18] for a comprehensive review of the origins of diffusiophoresis. New microfluidic methods offer the ability to directly measure and observe diffusiophoresis [108], which has previously been difficult.

When subjected to an external electric field, \mathbf{E}^∞ , a particle will migrate with an electrophoretic velocity $\mathbf{U} = M\mathbf{E}^\infty$ [19]. When instead exposed to a concentration gradient, the migration velocity is $\mathbf{U} = M\nabla \ln N^\infty$, where N^∞ is the number density of ions in the electroneutral bulk solution [40]. Note that in the previous two equations, the particle's phoretic mobility, M , is not the same, however we retain a single symbol (M) for brevity. To predict the diffusiophoretic mobility, theoretical studies have almost exclusively been based on the Poisson-Boltzmann (PB) equation. Therein, the equilibrium relationship between the number density of ion species i , N_i , and electrostatic

potential, ϕ , is a Boltzmann distribution,

$$N_i = N_i^\infty e^{-z_i \phi e / k_B T}, \quad (5.1)$$

where N_i^∞ is the number density of ion species i in the electroneutral bulk solution, z_i is the ion charge number, and k_B , T , and e are the Boltzmann constant, temperature, and fundamental charge, respectively. This relationship establishes the structure of the “diffuse layer” of charge which screens the particle’s surface charge. The diffuse layer has a characteristic width, $\lambda_D = \sqrt{\varepsilon k_B T / e^2 I}$, called the Debye length, where ε is the solution permittivity, and $I = \frac{1}{2} \sum_i z_i^2 N_i^\infty$ is the ionic strength. Prieve *et al.* [40] used the PB equation to predict the diffusiophoretic mobility of a spherical particle across a wide range of diffuse layer thicknesses (relative to the particle size), zeta potentials, and ionic species; for example, NaCl, NH₄F, and KBrO₃. They found that for some salts, the direction of particle migration could be reversed not only by changing the sign of the zeta potential but also by changing its magnitude.

The PB model assumes that the ions are point charges and have no interactions with each other, such as steric repulsion or electrostatic attraction/repulsion. However, this assumption can lead to unphysically large concentrations near highly charged surfaces or in concentrated electrolytes. For instance, consider a monovalent cation with hydrated volume v_+ ; the maximum density to which it can be packed is then $N_+^{\max} = 1/v_+$. Substituting this value into (5.1) and solving for the electrostatic potential, we obtain $\zeta_c = (k_B T / e) \ln(v_+ N_+^\infty)$ as the critical zeta potential to achieve maximum packing [26]. Using Cs⁺ as an example, the hydrated radius is 0.30 nm [103] and $v_+ = 0.216 \text{ nm}^3$. At a concentration of 1 M, $|\zeta_c| \sim 2(k_B T / e)$, about 50 mV, which is a realistic potential for colloids in physical systems. For this reason, the PB model is sometimes referred to as a dilute solution theory [2], since

it is most valid in relatively dilute solutions, where ion interactions brought about by steric repulsion can be neglected.

However, there are systems of importance that contain concentrated electrolyte solutions, such as in enhanced oil recovery where brine solutions $O(1 \text{ M})$ are encountered [16, 17]; mineral replacement reactions [18]; and energy generation from salinity gradients of sea water at river estuaries [118]. In order to describe the diffusiophoretic motion of colloidal particles in these systems, it is necessary to incorporate ion-ion interactions into a description of the electrolyte. This is the central goal of the present chapter. As a first step, we allow ions to interact sterically by accounting for their size in the governing equations for the structure of the diffuse layer and bulk solution.

One method of accounting for ion size is to establish a Stern layer adjacent to the particle surface [2]. The Stern layer is typically taken to be on the order of one ion radius in extent and acts as a capacitor in series with the diffuse layer. Although effective in eliminating the unphysical concentrations predicted by the PB equation, the Stern model only accounts for ion size at the solid surface and not throughout the diffuse layer or the electroneutral bulk solution. To do the latter, we instead modify the electrochemical potential, μ_i , of each ion species i to include an “excess” term,

$$\mu_i = \mu_i^{\text{id}} + \mu_i^{\text{ex}}, \quad (5.2)$$

where $\mu_i^{\text{id}} = z_i e \phi + k_B T \ln N_i$ is the ideal contribution; and μ_i^{ex} is the “excess” electrochemical potential [2, 28, 119, 120], which accounts for the entropic effect of ion size [120], allowing ions to interact with one another via steric repulsion.

The structure of the equilibrium diffuse layer is greatly affected by which model of μ_i^{ex} is used. For example, the simple Bikerman model [26, 86] predicts that a maximum counterion concentration is achieved for large zeta potentials

($> \zeta_c$), while the Carnahan-Starling model [2, 121] predicts lower concentrations at the surface with no maximum, but a more gradual decrease to the bulk concentration away from the surface. These models use the Local Density Approximation (LDA), which defines the density of ions at a point based on only the information at that point [2, 122]. This contrasts with methods used in density functional theory or molecular simulations (such as Monte Carlo or Molecular Dynamics) which use information throughout a specified volume to calculate an average density at each point [2, 122, 123]. While these non-local or weighted density approximations are capable of producing accurate descriptions of the diffuse layer at equilibrium, they are often computationally prohibitive to implement in the calculation of dynamic problems such as phoretic transport. This is because of the scale disparity between the size of the diffuse layer and of the particle: the former often being orders of magnitude smaller than the latter. Additionally, models based on the LDA have been shown to accurately capture integrated quantities such as capacitance of the diffuse layer [122, 123], even though the detailed ion profiles differ from density functional theory and molecular simulations.

For electrophoresis, the assumption of point-like ions leads to the prediction of a maximum in the mobility of a spherical particle with increasing zeta potential at $|\zeta| \sim O(k_B T/e) \ln(R/\lambda_D)$ [83, 84, 124], in the experimentally relevant thin diffuse layer limit ($\lambda_D/R \rightarrow 0$), where R is the particle radius. The maximum occurs because of surface conduction of the counterions in the diffuse layer, as described in section 5.4.1 and [125]. Khair and Squires [28], employing Bikerman's model for excess electrochemical potential, showed that the maximum in electrophoretic mobility could be delayed to much larger zeta potentials - beyond the physical limits of most practical systems. Hence, ion sterics effectively eliminates the mobility maximum in electrophoresis. They argue that the surface conduction of counterions is reduced due to the con-

straint of a maximum packing density imposed by Bikerman's model. That is, there are simply fewer counterions near the surface relative to the PB model at the same zeta potential.

In this chapter, we utilize three models of ion size in the calculation of the diffusiophoretic mobility of a uniformly charged spherical colloid in a weak electrolyte gradient for thin diffuse layers, $\lambda_D/R \rightarrow 0$. The three models are: Bikerman [2, 86, 119, 120], Carnahan-Starling [2, 119, 120], and Boublik-Mansoori-Carnahan-Starling-Leland [2, 119, 121, 126]. Due to the mathematical similarity between diffusiophoresis and electrophoresis, we take a general approach that is applicable to both phoretic motions.

In section 5.2, we present the mathematics underlying the inclusion of ion size effects (steric repulsion). In section 5.3, we derive the general phoretic mobility equation. In section 5.4, we present the results of mobility calculations based on a colloid with a varying zeta potential at a specified solution concentration (i.e. a single value of λ_D/R) which is a classic depiction of mobility variations in theoretical works [124]. In section 5.5, we present results for a colloid with a specified surface charge density with varying solution concentration, which is more relevant to how experiments are performed. Finally, in section 5.6, we offer concluding remarks.

5.2 Equilibrium Diffuse Layer and Modified Electrochemical Potentials

Consider a spherical particle of radius R and uniform zeta potential ζ immersed in a binary electrolyte. Since we do not consider a Stern layer here, the zeta potential, which is formally the potential drop across the diffuse layer, can be equated with the potential at the particle's surface. The dimension-

less number densities of cations and anions are n_+ and n_- , respectively, along with their respective charge numbers, z_+ and z_- . The charged surface attracts counterions and repels coions. This is balanced by Brownian diffusion, resulting in a diffuse layer of counter charge; a local counterion rich region near the surface. The structure of this equilibrium diffuse layer is described by Poisson's equation,

$$\epsilon^2 \nabla^2 \phi = - \sum_i z_i n_i, \quad (5.3a)$$

together with the condition of constant electrochemical potential at equilibrium,

$$\nabla \mu_i = \mathbf{0}, \quad (5.3b)$$

where ϕ is the electrostatic potential and $\epsilon = \lambda_D/R$, where $\lambda_D = \sqrt{\epsilon k_B T / e^2 I}$ is the Debye length, and the electrochemical potential is given by

$$\mu_i = z_i \phi + \ln N_i + \mu_i^{\text{ex}}. \quad (5.4)$$

In (5.3), and from here on, all quantities are dimensionless unless specified otherwise. The normalizations thus far are ϕ and $\zeta \sim k_B T / e$, $N_i \sim I$, $\mu_i \sim k_B T$, and $\nabla \sim 1/R$, where k_B is Boltzmann's constant, T is temperature, e is the fundamental charge, ϵ is the solution permittivity, and $I = \frac{1}{2} \sum_i z_i^2 N_i^\infty$ is the ionic strength. The quantity $N_i = n_i I$ is the dimensional ion number density of species i . A superscript ∞ denotes reference to the electroneutral bulk solution.

Neglecting ion size by setting $\mu_i^{\text{ex}} = 0$, equation (5.3b) results in a Boltzmann relationship between electrostatic potential and ion density (5.1). Substitution into (5.3a) then results in the Poisson-Boltzmann (PB) equation [19]. Bikerman's model for ion size (which we abbreviate as "Bik") is one of the

simplest modifications to the electrochemical potential that addresses the unphysical predictions of the PB equation. In the Bik model [2, 86],

$$\mu_{i,\text{Bik}}^{\text{ex}} = -\ln(1 - \Phi), \quad (5.5)$$

where $\Phi = \sum_i N_i v_i$ is the local volume fraction of ions and v_i is the dimensional hydrated volume of ion species i . The volume fraction varies from $0 \leq \Phi \leq 1$, where $\Phi = 1$ indicates that all of the solution at that point is occupied by ions. Importantly, Bik assumes that ions occupy sites on a regular lattice, so $v_i = a_i^3$, where a_i is the dimensional hydrated diameter of ion species i .

The attractiveness of using Bik is that one can derive a modified Poisson-Boltzmann equation (sometimes referred to as a Poisson-Bikerman equation [28]) by substituting (5.5) into (5.3) [2, 28]. However, Bik can also underestimate excluded volume effects in the dilute limit, $\Phi \rightarrow 0$ [2, 119]. To correct this, we could use $\mu_i^{\text{ex}} = -\ln(1 - 8\Phi)$ which accounts for the region of excluded volume around a sphere [119, 120]. However, this now overestimates steric repulsion at larger Φ .

The second model we consider is Carnahan-Starling (abbreviated as ‘‘CS’’) which is derived from liquid state theory for monodisperse hard spheres [2, 119, 120, 121]. As such, $v_i = \pi a_i^3/6$. In the CS model, the excess electrochemical potential is [2, 119, 120, 121]

$$\mu_{i,\text{CS}}^{\text{ex}} = \frac{\Phi(8 - 9\Phi + 3\Phi^2)}{(1 - \Phi)^3}. \quad (5.6)$$

As equations (5.5) and (5.6) indicate, μ_i^{ex} is equal for both species of ions for the Bik and CS models. This is because of the underlying assumption in Bik and CS that the ions are the same size and hence impose the same steric effects on one another. In this case, we assign each ion the average size of the pair, i.e. $a = (a_+ + a_-)/2$ is the ion size used in both the Bik and CS models for both cations and anions. This contrasts with the third model we

consider, the Boublik-Mansoori-Carnahan-Starling-Leland model (abbreviated as “BMCSL”), which is a generalization of CS for a mixture of hard spheres of differing size. As such, it explicitly accounts for different sized ions via an excess electrochemical potential [2, 119, 126, 127],

$$\begin{aligned} \mu_{i,\text{BMCSL}}^{\text{ex}} = & - \left[1 + 2 \left(\frac{\xi_2 a_i}{\Phi} \right)^3 - 3 \left(\frac{\xi_2 a_i}{\Phi} \right)^2 \right] \ln(1 - \Phi) + \frac{3\xi_2 a_i + 3\xi_1 a_i^2 + \xi_0 a_i^3}{1 - \Phi} \\ & + \frac{3\xi_2 a_i^2}{(1 - \Phi)^2} \left(\frac{\xi_2}{\Phi} + \xi_1 a_i \right) - \xi_2^3 a_i^3 \frac{\Phi^2 - 5\Phi + 2}{\Phi^2 (1 - \Phi)^3}, \end{aligned} \quad (5.7)$$

where $\xi_k = \sum_j N_j v_j a_j^{k-3}$. By setting $a_+ = a_-$ and hence $v_+ = v_-$, the CS model (5.6) is recovered.

BMCSL is capable of producing qualitatively different results compared to Bik and CS. The primary difference being that for a multicomponent electrolyte, smaller counterions are predicted to be the dominant species near a highly charged surface, in preference to larger counterions [2, 119]. This effect becomes greater as the surface charge is increased. However, since we consider only a binary electrolyte (and thus have only one counterion species) we do not observe this effect. Note, however, that for surfaces with charges that are equal in magnitude but opposite in sign, when the species which act as the counterion differ in size, the BMCSL model will predict different equilibrium profiles. In this case, the Bik, CS, and PB models will all predict the same profiles.

The assumption of Bik and CS that ions are of equal size contradicts them possibly having different diffusivities. Recall that the differences in diffusivities leads to an induced electric field that affects the diffusiophoretic mobility. Nevertheless, we ignore this contradiction and allow them to have unequal diffusivities. This is also why we consider the BMCSL model in order to more accurately portray differing ion size and as a check on the assumption of equal

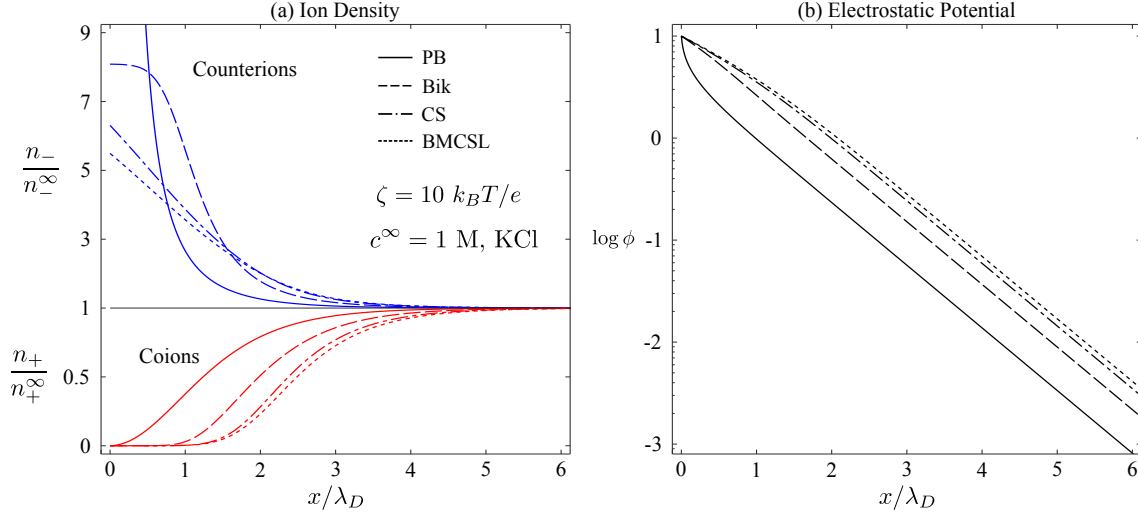


Figure 5.1: Equilibrium ion density within the diffuse layer on a positively charged flat plate ($\zeta = 10$) for a 1 M solution of KCl. Shown are the ion densities from the Poisson-Boltzmann (PB), Bikerman (Bik), Carnahan-Starling (CS), and Boublik-Mansoori-Carnahan-Starling-Leland (BMCSL) models. The counterions increase in concentration near the surface while the coions are excluded. The Bik model achieves a saturation of counterions whereas the PB model predicts an unbounded concentration near the surface. The CS and BMCSL models predict lower concentrations of counterions but a more gradual decrease to the electroneutral bulk solution. (b) Equilibrium electrostatic potential within the diffuse layer. As the ion densities extend further away from the surface, so too do the electrostatic potentials.

size.

In figure 5.1 we plot the equilibrium structure of the diffuse layer for a $c^\infty = 1$ M solution of KCl on a flat plate with $\zeta = 10$ and using $a_+ = 0.56$ nm and $a_- = 0.62$ nm [103] ($a = 0.59$ nm for Bik and CS). Whereas the PB model predicts an unbounded counterion density, the Bik model achieves a saturation of counterions (cnt), $n_{\text{cnt}}^{\text{max}} = 2/N_{\text{cnt}}^\infty z_{\text{cnt}}(z_{\text{cnt}} - z_{\text{co}})v_{\text{cnt}}$, where z_{co} is the charge number of the co-ions.

From figure 5.1(a), both Bik and CS predict counterion densities that do not exponentially increase as one approaches the charged surface. The excess of counterions (relative to the bulk) also extends further away from the surface than for PB. The reason for this is the steric barrier to adding additional ions at any point is greater than with PB because of μ_i^{ex} . For instance, μ_i^{ex} increases

more rapidly with Φ for CS than for Bik: for Bik, it is a slowly increasing logarithm, whereas for CS, it increases as $1/(1 - \Phi)^3$, therefore the CS model favors lower ion densities than Bik. Further, in the dilute limit where $\Phi \rightarrow 0$, Bik is given by $\mu_{i,\text{Bik}}^{\text{ex}} \approx \Phi$ to first order whereas CS is given by $\mu_{i,\text{CS}}^{\text{ex}} \approx 8\Phi$, and we see the factor of 8 due to excluded volume that is not captured with Bik. The differences between the CS and BMCSL models demonstrates the effect of using different sized counterions (0.59 nm in CS versus the true 0.62 nm in BMCSL).

The equilibrium electrostatic potential, figure 5.1(b), shows that despite the high concentration and large zeta potential, the classic Debye-Hückel result is attained far from the surface. This is because beyond a few Debye lengths, the electrostatic potential is below both the critical voltage, ζ_c , and the thermal voltage. Here, electrostatic potential scales as $\phi \sim \exp(-x/\lambda_D)$ for all four models.

5.3 Calculating Phoretic Mobility

5.3.1 Far field boundary conditions

Though conceptually different, electrophoresis (EP) and diffusiophoresis (DP) are mathematically similar. The essential difference is the boundary conditions in the electroneutral solution,

$$-\nabla\phi \rightarrow \mathbf{E}^\infty, \quad (5.8a)$$

$$n_i \rightarrow n_i^\infty, \quad (5.8b)$$

where \mathbf{E}^∞ is the imposed uniform electric field in EP and a (possible) induced electric field in DP. In addition, the bulk concentration is constant in EP but varies according to the concentration gradient in DP. In the latter case, we use the bulk concentration and \mathbf{E}^∞ that would exist at the center of the colloid

if the particle were not present. As long as the concentration gradient is not strong (as we assume in the next section), the time dependence of the particle's position can be neglected, i.e. the diffusiophoretic problem is quasi-steady.

To determine the induced electric field in a concentration gradient, consider that the ions will attempt to diffuse down the concentration gradient at different rates due to having unequal diffusivities. Countering this, and enforcing electroneutrality is an electric field (5.8a) that exactly balances the unequal diffusive fluxes and prevents a current from existing in the bulk solution. The net current is

$$\mathbf{J} = \sum_i z_i \mathbf{j}_i, \quad (5.9a)$$

where

$$\mathbf{j}_i = n_i(m\mathbf{v} - D_i\nabla\mu_i), \quad (5.9b)$$

is the flux of ion species i . In (5.9b), D_i is the diffusivity, \mathbf{v} is the velocity of the fluid, and $m = \varepsilon(k_B T/e)^2/D\eta$, where η is the viscosity, and

$$D = \frac{(z_+ - z_-)D_+D_-}{z_+D_+ - z_-D_-} \quad (5.10)$$

is the effective salt diffusivity [41]. In the preceding, $\mathbf{j}_i \sim ID/R$, $|\mathbf{v}| \sim \varepsilon(k_B T/e)^2/R\eta$, and $D_i \sim D$. Note that equation (5.9b) is an approximation to the flux that is only strictly valid in dilute solutions, where the diffusivity of ion, or solute, species can be taken as relative to the solvent only. A more detailed treatment of the ion flux would require using Stefan-Maxwell like fluxes [128], which account for solute diffusion relative to other solute species as well as relative to the solvent. In addition, the motion of solute in the solution contributes to the average velocity of the solution, whereas (5.9b) assumes this is equal to the velocity of the solvent only. Nevertheless, equation (5.9b) along with excess electrochemical potentials serve as a reasonable starting point to consider concentrated solutions of ions.

Evaluating (5.9) in the bulk, where $n_i = n_i^\infty$, setting $\mathbf{J} = \mathbf{0}$, substituting (5.4), and rearranging yields the induced electric field,

$$\mathbf{E}^\infty = \beta^{\text{id}} \nabla \ln N_+^\infty + \frac{D_+ \nabla \mu_+^{\text{ex},\infty} - D_- \nabla \mu_-^{\text{ex},\infty}}{z_+ D_+ - z_- D_-}, \quad (5.11)$$

where $\beta^{\text{id}} = (D_+ - D_-)/(z_+ D_+ - z_- D_-)$, and we have used the fact that \mathbf{E}^∞ acts to enforce electroneutrality. The first term in (5.11) is equivalent to that derived by Chiang and Velegol [129] and Prieve *et al.* [40], the latter of whom considered the case of $z_+ = -z_- = 1$. The novelty in (5.11) is the second term, which includes gradients of the excess electrochemical potential. These gradients can be understood as follows: within a concentration gradient of point-like ions, there is a driving force for ion motion due to the ideal electrochemical potential. This generates a gradient in the electrostatic potential which drives ions based on their charge, and a gradient in the ion density which drives ions towards regions of lower concentration. However, in a gradient of ions with finite size, there is an additional (“excess”) driving force due to the steric repulsion between the ions. This additional contribution manifests as a gradient in the excess electrochemical potential and drives ions to move towards regions of lower steric repulsion. It will be shown that this additional contribution to \mathbf{E}^∞ is significant for diffusiophoresis in concentrated electrolytes.

To make progress with the gradients in the second term of (5.11), we observe that the only variable all three models for μ_i^{ex} (5.5)-(5.7) depend on is the volume fraction, Φ , hence $\nabla \mu_i^{\text{ex},\infty} = (d\mu_i^{\text{ex},\infty}/d\Phi^\infty) \nabla \Phi^\infty$. Further, we define

$$H_i^\infty = \frac{d\mu_i^{\text{ex},\infty}}{d\Phi^\infty} \Phi^\infty, \quad (5.12)$$

such that $\nabla \mu_i^{\text{ex},\infty} = H_i^\infty \nabla \ln N_+^\infty$, where we have made use of the fact that for a binary electrolyte, $\nabla \ln \Phi^\infty = \nabla \ln N_+^\infty = \nabla \ln N_-^\infty$. Substituting the above

into (5.11) gives

$$\mathbf{E}^\infty = (\beta^{\text{id}} + \beta^{\text{ex}}) \nabla \ln N_+^\infty, \quad (5.13a)$$

where

$$\beta^{\text{ex}} = \frac{D_+ H_+^\infty - D_- H_-^\infty}{z_+ D_+ - z_- D_-}, \quad (5.13b)$$

acts as an “excess” contribution to the induced electric field that, like β^{id} , is a constant parameter of a given electrolyte pair but depends on the volume fraction through (5.12). This additional term serves to enhance the induced electric field. To see this, recall that Bik and CS assign each species the same excess potential, hence $H_+^\infty = H_-^\infty = H^\infty$. In this case, (5.13) reduces to

$$\mathbf{E}^\infty = \beta^{\text{id}}(1 + H^\infty) \nabla \ln N_+^\infty. \quad (5.14)$$

Further, since $0 \leq \Phi^\infty \leq 1$, it can be shown that $(d\mu_i^{\text{ex},\infty}/d\Phi^\infty) > 0$, which means that an increase in ion volume fraction - whether by additional ions or increased ion size - makes further increases less favorable and leads to $H^\infty > 0$. Therefore (5.14) represents an increase to the induced electric field over that predicted for an ideal solution, $H_i^\infty = 0$.

Substituting (5.13) (or (5.14)) into (5.8), we can write a general form for the far field boundary conditions:

$$-\nabla\phi \rightarrow \theta \mathbf{V}, \quad (5.15a)$$

$$n_i \rightarrow n_i^\infty, \quad (5.15b)$$

where

$$\theta = \begin{cases} 1 & , \text{ for EP} \\ \beta^{\text{id}} + \frac{D_+ H_+^\infty - D_- H_-^\infty}{z_+ D_+ - z_- D_-} & , \text{ for DP} \end{cases} \quad (5.15c)$$

is a generalized scale for the induced or applied electric field, and

$$\mathbf{V} = \begin{cases} \mathbf{E}^\infty & , \text{ for EP} \\ \nabla \ln N_+^\infty & , \text{ for DP,} \end{cases} \quad (5.16)$$

such that $\mathbf{E}^\infty = \theta \mathbf{V}$. Note that $\nabla \ln N_+^\infty$ in (5.16) could be replaced by any equivalent measure of concentration in the bulk (e.g., I , N_-^∞ , N_+^∞) since for a binary electrolyte $\nabla \ln N_+^\infty = \nabla \ln N_-^\infty = \nabla \ln I = \nabla \ln c^\infty = \nabla \ln \Phi^\infty$.

Boundary conditions (5.15) can be combined with (5.4) to form a far-field boundary condition on the electrochemical potential,

$$\nabla \mu_i \rightarrow G_i \mathbf{V}, \quad (5.17a)$$

where

$$G_i = \begin{cases} -z_i \theta & , \text{ for EP} \\ -z_i \theta + 1 + H_i^\infty & , \text{ for DP,} \end{cases} \quad (5.17b)$$

which allows us to collect all of the mathematical differences between EP and DP into a single quantity, G_i . Now the derivation for phoretic mobility can be performed generally by using (5.15) and (5.17), as we do in the next subsection.

5.3.2 Phoretic mobility: Thin Diffuse Layer Analysis

To drive the spherical colloid into motion, a uniform gradient of either electrostatic potential or electrolyte concentration is imposed. We denote the resulting “driving” vector generally as \mathbf{V} and give its two forms in (5.16). Importantly, we assume that $|\mathbf{V}| \ll 1$; more specifically,

$$|\mathbf{E}^\infty| \ll 1, \text{ for EP,} \quad (5.18a)$$

$$|\nabla \ln N_+^\infty| \ll 1, \text{ for DP,} \quad (5.18b)$$

where (5.18a) arises from the dimensional comparison $|\mathbf{E}^\infty| \ll k_B T/eR$, and (5.18b) from the dimensional comparison $|\nabla N_+^\infty| \ll N_+^\infty/R$, which state that the applied electrostatic potential and electrolyte concentration, respectively, do not vary appreciably on the scale of the particle. This condition is readily met for concentration gradients when the concentration is large. For example, for a 1 M concentration and a particle with radius 200 nm, according to the dimensional comparison above, the concentration gradient would need to be less than 50,000 M/cm.

These imposed gradients cause the spherical particle to move at a velocity $\mathbf{U} = M\mathbf{V}$, where M is the phoretic mobility of the particle, $|\mathbf{U}| \sim \varepsilon(k_B T/e)^2/R\eta$, and $M \sim \varepsilon(k_B T/e)/\eta$ for EP and $M \sim \varepsilon(k_B T/e)^2/\eta$ for DP. Despite the seeming simplicity of this equation, considerable effort has been made to calculate the value of M under a variety of conditions for both EP and DP [28, 40, 79, 84, 106, 124, 130]. Often, the Poisson equation (5.3a) is used together with

$$\frac{\partial n_i}{\partial t} = -\epsilon \nabla \cdot \mathbf{j}_i, \quad (5.19)$$

to describe the electrolyte dynamics. Equation (5.19) is the Nernst-Planck equation where t is time scaled by the RC time, $\lambda_D R/D$. Together, (5.3a) and (5.19) are the Poisson-Nernst-Planck (PNP) equations. We can simplify (5.19) by making the assumption that the problem is independent of time since (5.18b) implies that as the particle moves, the concentration evolves quasi-steadily [40]. Thus,

$$\nabla \cdot \mathbf{j}_i = 0. \quad (5.20)$$

To solve for the fluid velocity, the Stokes equations are used,

$$\nabla^2 \mathbf{v} - \nabla P = \sum_i n_i \nabla \mu_i / \epsilon^2, \quad (5.21a)$$

$$\nabla \cdot \mathbf{v} = 0. \quad (5.21b)$$

Equation (5.21a) is conservation of momentum with an electrochemical body force term to account for the ions. Equation (5.21b) is conservation of mass.

In a reference frame fixed at the particle center (such that $\mathbf{v} \rightarrow -\mathbf{U}$ far from the colloid), these equations are supplemented with boundary conditions at the particle surface,

$$\phi = \zeta, \quad (5.22a)$$

$$\mathbf{v} = \mathbf{0}, \quad (5.22b)$$

$$\hat{\mathbf{n}} \cdot \nabla \mu_i = 0, \quad (5.22c)$$

where $\hat{\mathbf{n}}$ is the unit normal to the surface. Equations (5.22b) and (5.22c) specify no-slip and no flux of ions through the surface, respectively. Of course, we also utilize a boundary condition far from the surface, (5.15) and (5.17), developed in the previous sub-section. In section 5.5, we replace (5.22a) with a constant surface charge density boundary condition.

Our derivation of the mobility equation follows closely that of O'Brien and White [124] and Khair and Squires [28]. To proceed, we express the unknowns in terms of a perturbation about their equilibrium values,

$$\phi = \phi^0 + \phi^1 |\mathbf{V}|, \quad (5.23a)$$

$$n_i = n_i^0 + n_i^1 |\mathbf{V}|, \quad (5.23b)$$

$$\mu_i = \mu_i^0 + \mu_i^1 |\mathbf{V}|, \quad (5.23c)$$

$$\mathbf{v} = \mathbf{v}^0 + \mathbf{v}^1 |\mathbf{V}|, \quad (5.23d)$$

where a superscript 0 denotes the equilibrium value and a superscript 1 denotes the perturbation. Substituting (5.23) into the governing equations (5.3), (5.20), and (5.21); the boundary conditions (5.15), (5.17), and (5.22); and neglecting all terms $O(|\mathbf{V}|^2)$ and higher, we obtain a set of linear differential equations governing the equilibrium and $O(|\mathbf{V}|)$ problems. Since the equilibrium problem has no imposed field, $\mathbf{v}^0 = \mathbf{0}$ and we are left with only Poisson's

equation (5.3a) and constancy of electrochemical potential (5.3b) describing the equilibrium problem. The perturbed, $O(|\mathbf{V}|)$, equations are

$$\epsilon^2 \nabla^2 \phi^1 = - \sum_i z_i n_i^1, \quad (5.24a)$$

$$m \nabla n_i^0 \cdot \mathbf{v}^1 = D_i \nabla \cdot (n_i^0 \nabla \mu_i^1), \quad (5.24b)$$

$$\epsilon^2 \nabla^2 (\nabla \times \mathbf{v}^1) = \sum_i (\nabla n_i^0 \times \nabla \mu_i^1), \quad (5.24c)$$

where (5.24c) results from taking the curl of the perturbed (5.21a) to eliminate pressure.

By considering the limit of thin diffuse layers, $\epsilon \rightarrow 0$, we can considerably simplify these equations. In this limit, the majority of the electrolyte is electroneutral except for a locally planar region near the surface of the colloid. For a more formal asymptotic analysis of this limit see [84, 131]. A key outcome is that, to leading order in ϵ , the perturbed electrochemical potential is constant across the diffuse layer, $\partial \mu_i^1 / \partial y = 0$, where $y = (r - 1)/\epsilon$ is a local coordinate perpendicular to the particle surface. Upon rescaling (5.24) with y , we find that the perpendicular fluid flow is negligible compared to the tangential component in the diffuse layer; the latter is given by [28]

$$\mathbf{v}^1 = - \sum_i \nabla_s \mu_i^1 \int_0^y \int_{y'}^\infty (n_i^0 - n_i^\infty) dy'' dy', \quad (5.25)$$

where $\nabla_s = (\mathbf{I} - \hat{\mathbf{n}}\hat{\mathbf{n}}) \cdot \nabla$ is the surface gradient operator and the sum is over both ion species, $i = +$ and $i = -$. The quantity $(n_i^0 - n_i^\infty)$ represents the concentration of ions within the diffuse layer relative to the electroneutral solution. To calculate the mobility we require the “slip” velocity which is obtained from the limit $y \rightarrow \infty$ of (5.25), that is, the velocity just outside the diffuse layer. The slip velocity is thus [28]

$$\mathbf{v}_s^1 = - \sum_i \nabla_s \mu_i^1 \int_0^\infty y (n_i^0 - n_i^\infty) dy. \quad (5.26)$$

To determine the perturbed electrochemical potentials, we require that at the “interface” between the diffuse layer and bulk solution ($y \rightarrow \infty$ or $r \rightarrow 1$, with ϵ fixed), all quantities (n_i , μ_i , etc.), are continuous. This means that since n_i^0 is constant in the bulk, we have from equation (5.24b) that $\nabla^2 \mu_i^1 = 0$ throughout the bulk. Solving this subject to boundary condition (5.17) we obtain

$$\mu_i^1 = (G_i + C_i r^{-3}) \mathbf{V} \cdot \mathbf{r}, \quad (5.27)$$

where \mathbf{r} is the position from the center of the sphere, and C_i are integration constants to be determined below.

The mobility is then calculated by averaging \mathbf{v}_s^1 over the surface of the sphere [132],

$$M\mathbf{V} = -\frac{1}{4\pi} \int_S \mathbf{v}_s^1 dS. \quad (5.28)$$

The mobility is thereby

$$M = \frac{2}{3} \sum_i \left[(G_i + C_i) \int_0^\infty y (n_i^0 - n_i^\infty) dy \right]. \quad (5.29)$$

From (5.29), we see that it is the deviation of ion density relative to its value in the bulk, $n_i^0 - n_i^\infty$, that arises in the mobility equation, as opposed to the actual value of ion density, n_i^0 , at a location y .

The remaining constants, C_i , are computed by establishing effective boundary conditions for μ_i^1 between the diffuse layer and the bulk. This is done by balancing the normal flux of ions between the diffuse layer and the bulk with the variation in the tangential flux. Following [28], these boundary conditions are

$$\frac{\partial \mu_i^1}{\partial r} = (f_i \nabla_s^2 \mu_i^1 + g_i \nabla_s^2 \mu_j^1), \quad \text{at } r = 1, \quad (5.30)$$

where $i \neq j$ and

$$f_i = -\epsilon D_i \int_0^\infty (n_i^0 - n_i^\infty) dy - \epsilon m \int_0^\infty (n_i^0 - n_i^\infty) I_i dy, \quad (5.31a)$$

$$g_i = -\epsilon m \int_0^\infty (n_i^0 - n_i^\infty) I_j dy, \quad (5.31b)$$

where $I_i = \int_0^y \int_{y'}^\infty (n_i^0 - n_i^\infty) dy'' dy'$. The C_i are then,

$$C_i = \frac{G_i(2g_i g_j - (2f_i + 1)(f_j - 1)) + 3G_j g_i}{2(f_i - 1)(f_j - 1) - 2g_i g_j}. \quad (5.32)$$

Substituting (5.32) into (5.29) yields an equation which explicitly shows the dependence of the mobility on G_i , that is, on whether EP or DP is considered,

$$M = \sum_i \left[\left(\frac{G_i(1 - f_j) + g_i G_j}{(f_i - 1)(f_j - 1) - g_i g_j} \right) \int_0^\infty y(n_i^0 - n_i^\infty) dy \right], \quad (5.33)$$

where again $i \neq j$.

Equations (5.29) and (5.33) are general expressions of both electrophoretic and diffusiophoretic mobility for a spherical colloid in a binary electrolyte, where z_+ and z_- are not necessarily equal. Ion steric effects (steric repulsion) are contained within the equilibrium ion densities, n_i^0 , and the phoresis dependent far-field electrochemical potential gradient, G_i (5.17b).

5.4 Phoretic Mobility: For Varying Zeta

Potential at Fixed Concentration

In our calculations that follow, all hydrated ion size data is taken from Ohtaki and Radai [103]. The reported size of hydrated ions varies depending on the experimental methods and theories used to determine it. For more information on this, as well as extensive tables of ion size data, see [103]. All diffusivity data is taken from Flury and Gimmi [133] (table 6.2-1), which is calculated from conductance in the limit of low concentration. Their table 6.2-2 shows that the concentration dependence of salt diffusivity is weak up to a concentration of 1 M. Beyond that, the diffusivity is expected to decrease approximately as $D_i = D_{i,o}(1 - \Phi_i)$, where $D_{i,o}$ is the diffusivity in a dilute solution [134]. Incorporating a concentration dependent diffusivity would require including

D_i in the integral of equations (5.31). However, since $\epsilon \ll 1$ at large concentrations, this change has little impact on the mobility. The induced electric field would be affected via the dependence of β^{id} and β^{ex} on ion diffusivity for the BMCSL model only, since the other models assume each ion species has the same size (and hence the same volume fraction). Although β^{id} could be significantly reduced, e.g. for NaCl from a value of -0.2074 in a dilute solution to -0.0719 at 5 M, β^{ex} will continue to increase rapidly with concentration. This is because, as we give in the appendix, H_i^∞ diverges more rapidly than the diffusivity vanishes as $\Phi^\infty \rightarrow 1$. Hence the qualitative results presented in this chapter are not affected by the use of a dilute solution value of the diffusivity.

To characterize the effect of the surface conduction of ions within the diffuse layer on the mobility, we utilize the dimensionless Dukhin number, $\text{Du} = \sigma_s/\sigma_b$, which is a measure of the surface conductivity, σ_s , relative to the conductivity in the bulk, σ_b . The bulk conductivity is just the electrical conductivity, $\sigma_b = \sum_i z_i^2 D_i n_i^\infty$, in the electroneutral bulk solution [125]. Note that although there is no current in the bulk solution for DP, there is still a conductivity given by σ_b . Defining the surface conductivity by the surface current, $\mathbf{J}_s = \sigma_s \mathbf{V}$, and the driving vector \mathbf{V} , we can derive a generalized Dukhin number that is valid for both EP and DP.

Substituting (5.9b) into (5.9a), the total current is given by $\mathbf{J} = \rho m \mathbf{v} - \sum_i z_i D_i n_i \nabla \mu_i$, where $\rho = \sum_i z_i n_i$ is the charge density. Applying this to the bulk solution, where $n_i = n_i^\infty$ and $\rho = 0$, and substituting (5.4) for μ_i , we obtain $\mathbf{J}_b = \sum_i z_i^2 D_i n_i^\infty \mathbf{E}^\infty - \sum_i z_i D_i n_i^\infty G_{i,\text{DP}} \mathbf{V}$ for the current in the bulk solution, where $G_{i,\text{DP}} = 1 + H_i^\infty$ is the contribution to $\nabla \mu_i^\infty$ due to a concentration gradient. The surface current is then the current in excess of \mathbf{J}_b , integrated over the diffuse layer, $\mathbf{J}_s = \epsilon \int_0^\infty (\mathbf{J} - \mathbf{J}_b) dy$. Substituting (5.25),

(5.17), and using the fact that $\partial\mu_i^1/\partial y = 0$ within the diffuse layer, we obtain

$$\mathbf{J}_s = \epsilon \int_0^\infty \left[\sum_i z_i^2 D_i (n_i^0 - n_i^\infty) \theta - \rho^0 m \sum_i G_i I_i - \sum_i z_i D_i (n_i^0 - n_i^\infty) G_{i,\text{DP}} \right] dy \mathbf{V}, \quad (5.34)$$

where we have also made use of the fact that $\mathbf{E}^\infty = \theta \mathbf{V}$. The first term in (5.34) is due to the electromigration of ions with the electric field (induced or applied). The second term is due to convection of ions with the electro- and chemiosmotic fluid flow. The third term represents the contribution from ions diffusing down the concentration gradient.

The generalized Dukhin number is therefore given by

$$\text{Du} = \frac{\epsilon}{\sum_i (z_i^2 D_i n_i^\infty)} \int_0^\infty \left[\sum_i z_i^2 D_i (n_i^0 - n_i^\infty) \theta - \rho^0 m \sum_i G_i I_i - \sum_i z_i D_i (n_i^0 - n_i^\infty) G_{i,\text{DP}} \right] dy, \quad (5.35)$$

Note that for EP, $G_{i,\text{DP}} = 0$ since there is no applied concentration gradient; in this case, the usual definition of the Dukhin number is recovered [28, 60, 125].

5.4.1 Electrophoresis

Figure 5.2a shows the electrophoretic mobility for a 1 M KCl solution with $\epsilon = 0.01$ for PB, Bik, CS, and BMCSL over the range $\zeta = -10$ to 10. First note that the negative zeta potentials have negative mobilities whereas the positive potentials give positive mobilities, i.e. negatively (positively) charged particles move against (with) the applied field. The PB model predicts a maximum in the mobility at $\zeta \sim \pm 6.5$, whereas Bik, CS, and BMCSL predict a continuously increasing mobility over the range of zeta shown. The maximum in PB is due to the increasing importance of surface conduction with exponentially increasing counterion concentration in the diffuse layer [84]. This is reflected in figure 2c, which is a plot of Du versus ζ . As ζ increases (in magnitude), the surface conduction increases rapidly until it offsets further increases in mobility.

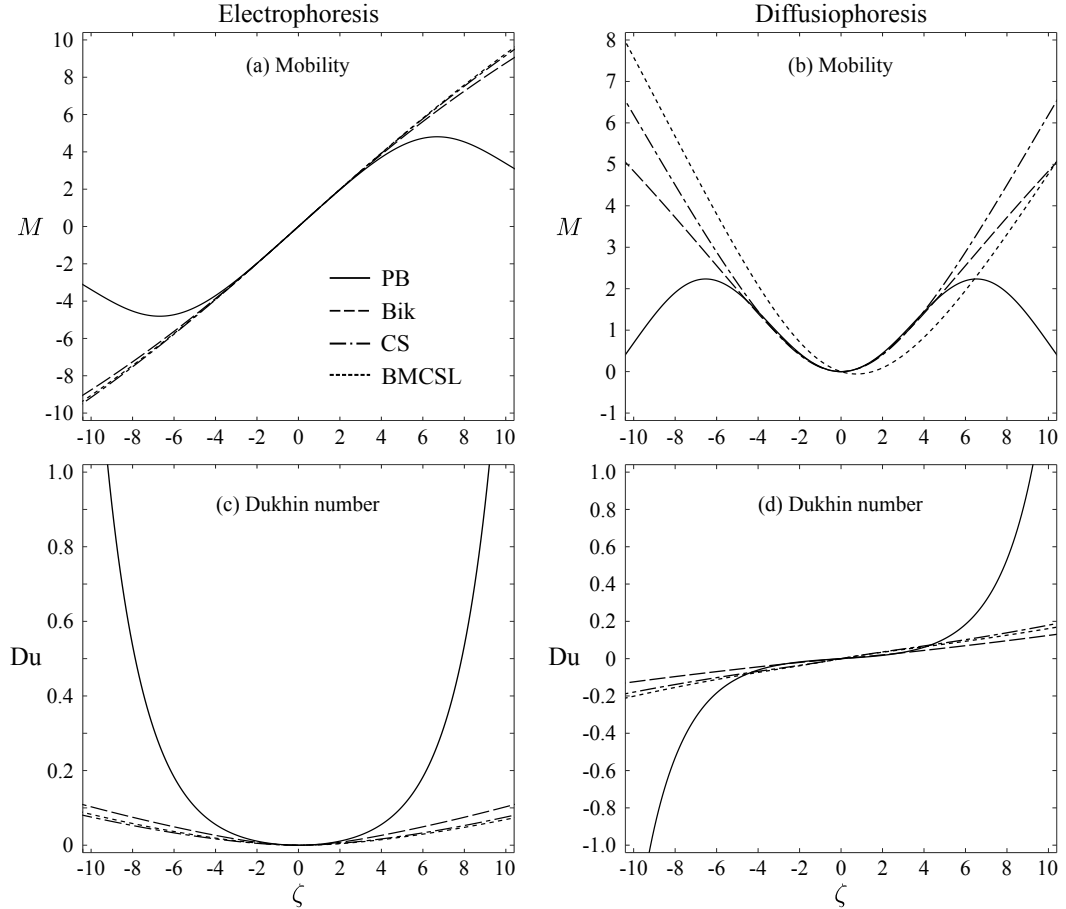


Figure 5.2: Phoretic mobility for a 1 M solution of KCl with $\epsilon = 0.01$ for all four models of ion size: Electrophoretic mobility (a) and corresponding Dukhin number (c) versus zeta potential; diffusiophoretic mobility (b) and corresponding Dukhin number (d) versus zeta potential. Diffusiophoretic plots (b and d) assume equal diffusivities for the cation and anion, $D_+ = D_-$, leading to $\beta^{\text{id}} = 0$.

To see how surface conduction affects the mobility (in the case of PB) it is instructive to consider the (academic) limit $\zeta \rightarrow \infty$ with ϵ fixed (i.e. $Du \rightarrow \infty$). Here, the constants C_i in (5.27) adopt values for a conductor of counterions, $C_{\text{cnt}} = -G_{\text{cnt}}$, and an insulator of co-ions, $C_{\text{co}} = G_{\text{co}}/2$. This ensures that a maximal flux of counter charge can be exchanged between the bulk solution and diffuse layer. Then using these values for C_i together with (5.4) we can derive equations for the perturbed electric potential and ion density in the bulk. The derivation is given in the appendix along with the full expressions

for both EP and DP; here, we give simplified forms relevant to a symmetric, monovalent electrolyte. For electrophoresis these equations are,

$$\phi^1 = -\left(1 - \frac{1}{4r^3}\right)\mathbf{E}^\infty \cdot \mathbf{r}, \quad (5.36a)$$

$$c^1 = n_+^1 + n_-^1 = -\frac{3\text{sgn}(\zeta)}{2r^3}\mathbf{E}^\infty \cdot \mathbf{r}, \quad (5.36b)$$

where $\text{sgn}(\zeta)$ is the sign of ζ .

These equations are identical to those given by Khair and Squires [125]. Figure 5.3 are streamlines of the electric field, $-\nabla\phi^1$, and concentration gradient, $-\nabla c^1$ showing the direction of neutral salt motion, for a positively charged particle. These figures again are identical to those produced by Khair and Squires [125] but are reproduced here to contrast with the forthcoming predictions for DP.

Figure 5.3 (a) shows that the applied electric field is uniform far from the sphere but varies across the surface, where the “surface” is the interface between the thin diffuse layer and the bulk solution. In particular, the tangential component, which is zero at the poles and maximum at the equator, drives a tangentially varying surface flux of counterions (surface conduction). This necessitates that the negative counter ions be exchanged between the diffuse layer and bulk solution. This exchange occurs along the electric field lines and counterions exit the diffuse layer in the upstream and enter in the downstream, relative to the applied electric field, \mathbf{E}^∞ . Of course, the positive co-ions also move along these bulk field lines but are excluded from the diffuse layer. The result is a concentration polarization in the bulk with a greater concentration in the upstream region and a chemiosmotic flow due to gradients in neutral salt (figure 3(b)), from upstream to downstream, which counteracts the electro-osmotic flow and reduces the mobility.

Accounting for steric repulsion between ions eliminates the exponential increase of counterions in the diffuse layer, which means a reduced surface

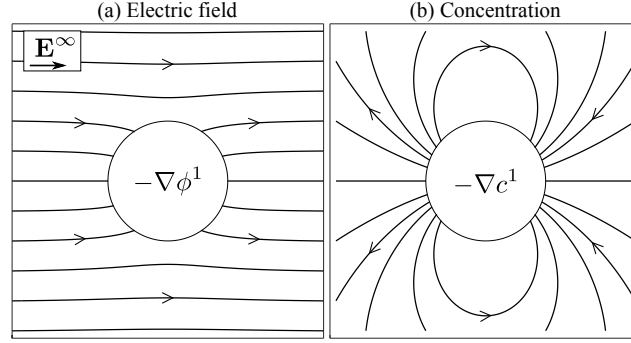


Figure 5.3: Streamlines of the electric field (a) and concentration flux (b) for electrophoresis using the PB model for $\zeta \rightarrow +\infty$ and ϵ fixed, such that $Du \rightarrow +\infty$.

conduction of counterions; consequently, the mobility continues to increase. In fact, for $\epsilon = 0$ with ζ fixed and finite, surface conduction becomes negligible, and all four models approach limiting lines. The slopes of these lines are dependent on the model since the equilibrium diffuse layers have differing structures. In the case of the PB model, the classic Helmholtz-Smoluchowski mobility, $M = \zeta$, is recovered. In general, for $\epsilon \equiv 0$ with ζ fixed, $C_i = G_i/2$ and

$$M = \sum_i \left[G_i \int_0^\infty y(n_i^0 - n_i^\infty) dy \right], \quad (5.37)$$

which is valid for both EP and DP but resists analytic treatment for $\mu_i^{\text{ex}} \neq 0$.

Finally, all four models agree in a range of ζ between about -3 and 3, suggesting that for potentials below about ± 75 mV, steric repulsion between ion does not significantly affect electrophoretic mobility - even in rather concentrated solutions.

5.4.2 Diffusiophoresis

Symmetric electrolytes ($D_+ = D_-$)

Although similar mathematically to electrophoresis, the induced electric field (5.13) brought about by diffusivity differences and steric repulsion between

ions adds a unique feature to diffusiophoresis. As such, we will first consider an idealized example of KCl in which we assume the diffusivities are equal and hence $\beta^{\text{id}} = 0$. Note that the actual value for KCl is $\beta^{\text{id}} = -0.0188$. A consequence of this assumption is that the induced electric field is non-existent for PB, Bik, and CS and the situation resembles that of DP in non-electrolytes. For BMCSL, since $H_+^\infty \neq H_-^\infty$, then $\beta^{\text{ex}} \neq 0$ and an induced electric field exists due solely to steric repulsion between ions as a result of ion size differences.

Figure 5.2c shows the diffusiophoretic mobility for a 1 M KCl solution with $\epsilon = 0.01$ for PB, Bik, CS, and BMCSL over the range $\zeta = -10$ to 10. Unlike in EP, the PB, Bik, and CS models all predict a symmetric mobility about $\zeta = 0$. This is expected since, in the absence of an induced electric field, the particle will prefer to move towards regions of higher ion concentration, i.e. in the direction of the concentration gradient. Therefore, the mobility is symmetric due to neglecting diffusivity differences and assuming both ion species are the same size (or zero size in PB).

This behavior contrasts with what the BMCSL model predicts, which allows for different sized ions. The asymmetry in BMCSL is due primarily to the induced electric field arising from ion size (β^{ex}) as explained above. Another factor is that when $\zeta < 0$, the smaller ion, K^+ , is the counterion which is able to more tightly pack in the diffuse layer than Cl^- when $\zeta > 0$ and it is the counterion. This results in differing equilibrium diffuse layer structures on either side of $\zeta = 0$ and hence an asymmetric mobility. This second factor is much less significant than the induced electric field. In fact, although we do not show this result, by setting $\beta^{\text{ex}} = 0$ (neglecting the induced electric field completely, i.e. $\theta = 0$) the BMCSL model gives mobilities which are much closer to the CS model results. This is despite predicting quantitatively different diffuse layer structures (see figure 5.1), which demonstrates how integrated quantities such as mobility and diffuse layer capacitance do

not have a strong dependence on the structure of the equilibrium diffuse layer, for differing models that account for ion size.

Figure 5.2(d) shows the Dukhin number for diffusiophoresis. As with EP, the PB model predicts a large increase in surface conduction along with a corresponding maximum in mobility. Although Du is always positive for electrophoresis, our generalized Du can take on negative values for DP. However, it is the magnitude of Du which is important. The PB model gives a much larger $|Du|$ than Bik, CS, or BMCSL, indicating significantly greater surface conduction in DP; just as in EP.

The negative values of Du occur because the convective, $-\epsilon \int_0^\infty \rho^0 m \sum_i G_i I_i dy \mathbf{V}$, and concentration gradient, $-\epsilon \int_0^\infty \sum_i z_i D_i (n_i^0 - n_i^\infty) G_{i,DP} dy \mathbf{V}$, contributions to the surface current can be either positive or negative. Since the convective flux is in the opposite direction as particle migration, if positively and negatively charged particles migrate in the same direction (as they do in DP for reasonable zeta potentials), then the convective current will be in opposite directions due to having oppositely charged diffuse layers. Similarly, the flux due to the concentration gradient is always in the same direction and oppositely charged diffuse layers will result in positive or negative current. Therefore, a positively (negatively) charged particle has positive (negative) convective and concentration gradient surface currents. Because the bulk conductivity is always positive, this leads to $Du < 0$ when $\zeta < 0$ and $Du > 0$ when $\zeta > 0$ for the case of $D_+ = D_-$ with KCl.

By assuming the diffusivities are equal, we are effectively neglecting the electromigrative contribution to the surface current, $\epsilon \int_0^\infty \sum_i z_i^2 D_i (n_i^0 - n_i^\infty) \theta dy \mathbf{V}$, since $\theta = 0$. If we allowed the electric field to be non-zero, however, the electromigrative surface current would be positive (negative) for a positive (negative) value of θ , regardless of the sign of the zeta potential. In summary, a negative value for Du is possible when $\theta < 0$, or when $\theta \geq 0$ if $\zeta < 0$.

As with EP, we can turn to streamlines of the perturbed electrostatic potential and neutral salt concentration fields to help explain the effect of surface conduction on mobility. At large $|Du|$,

$$\phi^1 = \frac{3\text{sgn}(\zeta)}{4r^3} (\nabla \ln N_+^\infty) \cdot \mathbf{r}, \quad (5.38a)$$

$$c^1 = n_+^1 + n_-^1 = 2 \left(1 - \frac{1}{4r^3} \right) (\nabla \ln N_+^\infty) \cdot \mathbf{r}, \quad (5.38b)$$

which in comparing with (5.36) we see the roles of ϕ^1 and c^1 are reversed from EP. This similarity is readily understood: in EP, $-\nabla\phi^1|_{r\rightarrow\infty} = \mathbf{E}^\infty$ is the applied, uniform field and the bulk concentration gradient, $-\nabla c^1$, is a result of surface conduction. Conversely, in DP, $\nabla c^1|_{r\rightarrow\infty}$ is the applied and uniform field and $-\nabla\phi^1$ is the result of surface conduction. As such, the explanation for the mobility maximum is similar to that for EP. Specifically, from figure 5.4(b) we see that the concentration flux is uniform far from the sphere and varies across the surface (the interface between the thin diffuse layer and the bulk). This drives a tangentially varying surface flux of counterions (negative ions). This simultaneously directs bulk concentration field lines into (out of) the diffuse layer over the downstream (upstream) regions - relative to the applied concentration gradient. To prevent coions from entering the diffuse layer, a bulk electric field (figure 5.4(e)) is established that induces an electro-osmotic flow which counteracts the chemiosmotic flow, resulting in a reduced mobility. Therefore, the mobility maximum is not observed when steric repulsion is taken into account because of the reduced surface conduction arising from reduced counterion densities within the diffuse layer.

Asymmetric electrolytes ($D_+ \neq D_-$)

For real salts, the diffusivities are unequal and $\beta^{\text{id}} \neq 0$. Figure 5.5 is a plot of zeta potential versus mobility for 1 M solutions of several different electrolytes using all four models. We see the expected behavior of a mobility maximum

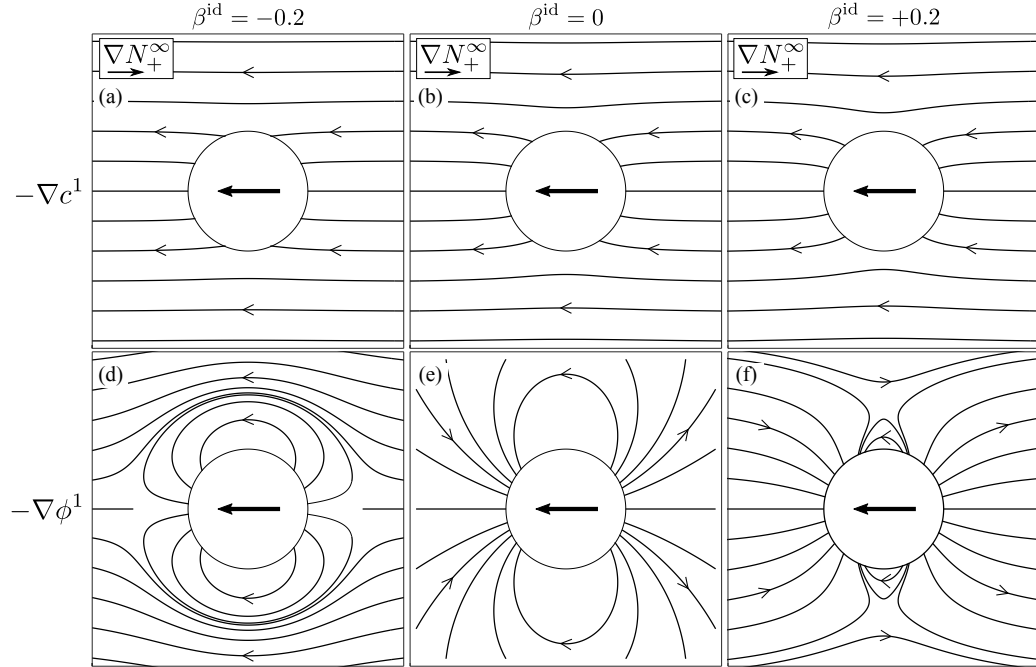


Figure 5.4: Streamlines of concentration flux (a-c) and electric field (d-f) for diffusiophoresis using the PB model for three representative values of β^{id} as $\zeta \rightarrow +\infty$ and ϵ fixed such that $|\text{Du}| \rightarrow \infty$. The varying tangential component of the concentration flux gives rise to a surface conduction induced local electric field for all three values of β^{id} , which provides field lines along which charge can be exchanged between the diffuse layer and the electroneutral bulk. Far from the particle, away from the local electric field, the induced electric field \mathbf{E}^∞ is recovered for $\beta^{\text{id}} \neq 0$.

in PB and no maximum for all models of ion size due to the effect of reducing surface conduction.

For PB, Bik, and CS, as $|\beta^{\text{id}}|$ increases, the asymmetry in the mobility will increase and the larger mobility will be that for which $\beta^{\text{id}}\zeta > 0$. When this condition is met, the electrophoretic contribution to the mobility will be towards higher concentrations and support the chemiphoretic contribution which always acts towards higher concentrations. This generalization is possible because the ions are assumed to be the same size in these three models and $\theta = \beta^{\text{id}}(1 + H)$. As for the above case of symmetric electrolytes, the BMCSL model incorporates the additional asymmetry of different sized ions and such a generalization is not possible due to the more complex dependence

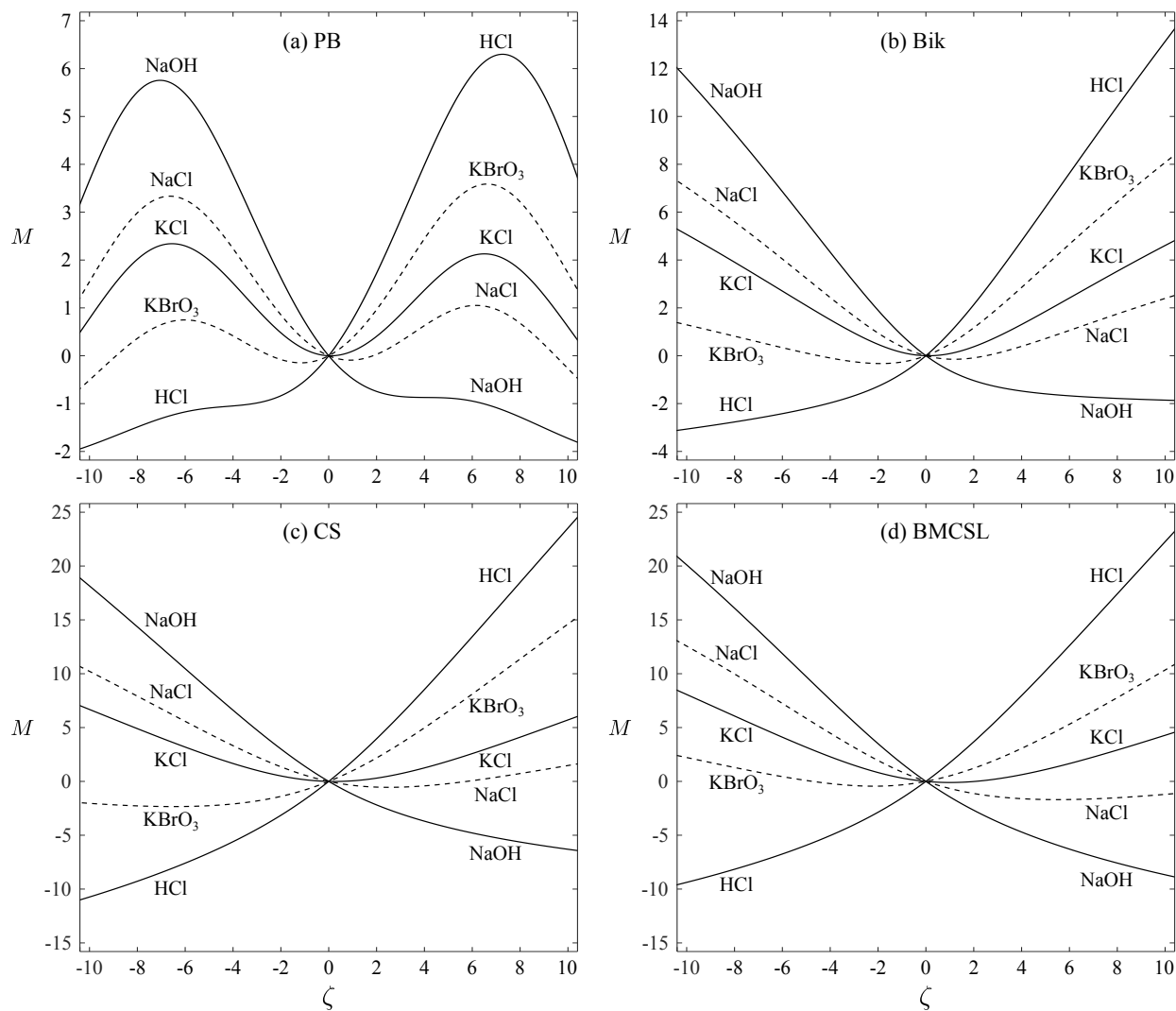


Figure 5.5: Diffusiophoretic mobility versus zeta potential for different salts using (a) PNP, (b) Bik, (c) CS, and (d) BMCSL. The salts have the following values for β^{id} : NaOH (-0.5962), NaCl (-0.2074), KCl (-0.0188), KBrO₃ (0.2618), and HCl (0.6417). All concentrations are 1 M and $\epsilon = 0.01$. The dashed and solid lines are to aid readability.

of the induced electric field on diffusivity and ion size (see (5.15c)). However we observe the same general trend in figure 5.5(d) and predict that the larger mobility will be for that colloid and electrolyte for which $\theta\zeta > 0$.

For non-zero β^{id} , the equations for the perturbed electrostatic potential and neutral salt density in the bulk for the PB model at large $|\text{Du}|$ are

$$\phi^1 = \left[-\beta^{\text{id}} \left(1 - \frac{1}{4r^3} \right) + \frac{3\text{sgn}(\zeta)}{4r^3} \right] (\nabla \ln N^\infty) \cdot \mathbf{r}, \quad (5.39a)$$

$$c^1 = 2 \left[\left(1 - \frac{1}{4r^3} \right) - \frac{3\text{sgn}(\zeta)}{4r^3} \beta^{\text{id}} \right] (\nabla \ln N^\infty) \cdot \mathbf{r}. \quad (5.39b)$$

The terms containing β^{id} are the electrophoretic contribution and setting $\beta^{\text{id}}=0$ recovers the results in (5.38).

The effect of β^{id} on the streamlines is shown in figure 5.4 for $\zeta > 0$. For all possible values of β^{id} ($-1 < \beta^{\text{id}} < 1$), a “local” electric field is generated by the same surface conduction mechanism described above for symmetric electrolytes, i.e. $\beta^{\text{id}} = 0$. This electric field is directed outward over the downstream region and inward over the upstream region of the sphere (relative to the concentration gradient). Because of this, the induced electric field (far from the sphere) for $\beta^{\text{id}} < 0$ cannot participate in the exchange of counter charge between the diffuse layer and the bulk solution. However, for $\beta^{\text{id}} > 0$, it can serve as a source of field lines for the exchange of counter charge. As β^{id} becomes more positive, the concentration flux lines are directed more normal to the surface. This leads to a decrease in the magnitude of the tangential flux and hence a reduced mobility (for a positively charged surface, where $\zeta \rightarrow +\infty$). Note that this is not shown in figure 5.5(a) as the large zeta behavior does not become apparent for the electrolytes given until $|\zeta| \approx 15$, which is not experimentally feasible.

To directly compare EP to DP in the limit of large zeta for PB, we can simplify equation (5.29) for the limit of large zeta with ϵ fixed (i.e. $|\text{Du}| \rightarrow \infty$)

and for $z_+ = -z_- = z$. In this limit, the mobility equation simplifies to

$$M = \begin{cases} \frac{\text{sgn}(\zeta)}{z} \ln 4, & \text{for EP,} \\ \left(\text{sgn}(\zeta) z \beta^{\text{id}} - 1 \right) \frac{1}{z^2} \ln 4, & \text{for DP.} \end{cases} \quad (5.40)$$

The result in (5.40) for EP is known [84, 125, 135], but we believe the result for DP is novel. In both cases, the mobility becomes independent of $|\zeta|$, depending only the sign of the zeta potential. From (5.40), we see that the EP mobility has the same sign as the zeta potential, indicating that positively (negatively) charged particles move with (against) the electric field. However, for DP, it is straightforward to show that the mobility is negative (i.e. toward lower concentrations) for any electrolyte and particle zeta potential since $|\beta^{\text{id}}| < 1/z$. This indicates that large surface conduction effects, such as the local electric field, dominate the diffusiophoretic motion of the particle in the limit of large zeta. Again, these limiting values are approached when $|\zeta| \gtrsim 15$ and thus not observed in figure 5.5.

5.5 Phoretic Mobility: For Varying Concentration at Fixed Surface Charge Density

Here, we consider a colloid with a constant, uniform surface charge density and vary the concentration of the electrolyte solution (i.e. ϵ). This is a more relevant point of view to how experiments involving electrophoresis and diffusiophoresis are typically carried out. That is, it is difficult to vary the zeta potential while keeping the Debye layer thickness fixed (as both are functions of concentration), as was the focus of the previous section. If the electrolyte consists of potential determining ions, changing the electrolyte concentration

can ionize/deionize chemically active sites on the particle surface such that both the zeta potential and surface charge density change with concentration [136]. Here, we assume a constant surface charge density and thus do not account for this effect.

We denote the dimensional surface charge density as Γ^* and use Gauss's Law to relate it to the electrostatic potential at the surface, $-\varepsilon\hat{\mathbf{n}} \cdot \nabla\phi = \Gamma^*$ [19]. In terms of the local planar co-ordinate, y , we replace boundary condition (5.22a) with

$$\left. \frac{d\phi}{dy} \right|_{y=0} = -\varepsilon\Gamma, \quad (5.41)$$

where $\Gamma = \Gamma^*/(\varepsilon k_B T/eR)$ is the dimensionless surface charge density. For the purposes of calculating ε , we assumed a colloid radius of $R = 210$ nm. For PB, it is straightforward to derive Graham's equation, $\Gamma = 2\sqrt{2}\varepsilon \sinh(z\zeta/2)$, for $z_+ = -z_- = z$, which relates the surface charge density, bulk concentration, and zeta potential [19]. It is generally not possible to derive analogous closed-form equations for ion steric models except for Bik [2].

Figure 5.6 plots electrophoretic mobility and diffusiophoretic mobility versus concentration (up to a maximum concentration of 5 M) for a spherical colloid with a uniform surface charge density of $3.0 \mu\text{C}/\text{cm}^2$. This value for surface charge density is used as an intermediate value in the range typically encountered [137, 138]. For the concentration range shown, $1 \text{ mM} \leq c^\infty \leq 5 \text{ M}$, the diffuse layer is still quite thin, $0.062 \leq \varepsilon \leq 8.77 \times 10^{-4}$, even with the particle size of $R = 210$ nm. Figures 5.6(a) and (b) are for the symmetric treatment of KCl for which we assume the diffusivities are equal ($\beta^{\text{id}} = 0$); figures 5.6(c) and (d) are for the asymmetric case of NaCl. We see that the electrophoretic mobility is essentially the same in both electrolytes for all four models; indicating that, surprisingly, there is no appreciable difference in the predictions between the simple PB model and the more complex models for

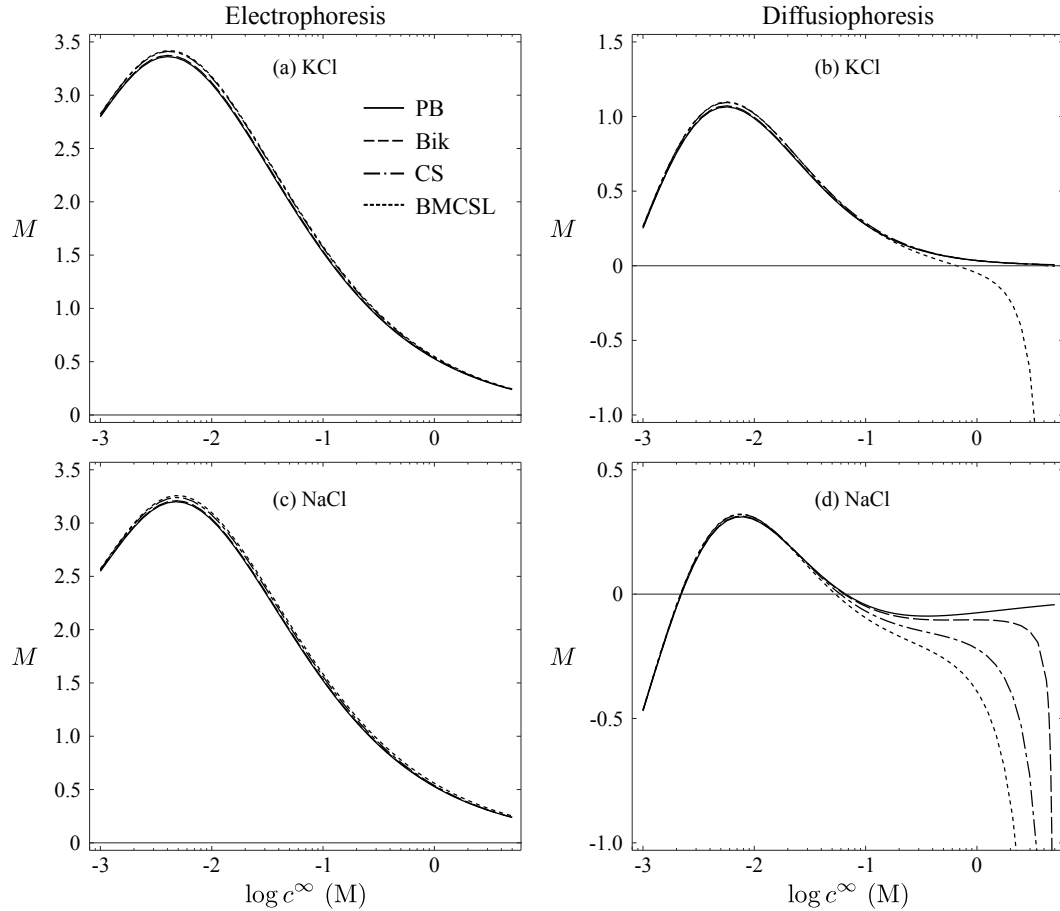


Figure 5.6: The phoretic mobility for a colloid with constant surface charge density $\Gamma^* = 3 \mu\text{C}/\text{cm}^2$ in a solution of KCl (where $D_+ = D_-$) (a, b) and NaCl (c, d). The electrophoretic mobility (a, c) shows essentially no difference between the four models while the diffusiophoretic mobility (b, d) has significant variation at large concentrations due to the rapidly increasing induced electric field. The BMCSL model deviates in KCl (b) because it retains a non-zero β^{ex} when $D_+ = D_-$.

ion size.

We see that in KCl, the diffusiophoretic mobility predicted from PB, Bik, and CS are essentially the same as well; BMCSL differs only at large concentrations. In NaCl, all three models incorporating ion size predict qualitatively different diffusiophoretic mobilities compared with the PB model.

This large concentration behavior can be understood in terms of the zeta potential and induced electric field. Figure 5.7(a) is a plot of zeta potential versus concentration in NaCl. All four models predict that the zeta potential

decreases with increasing electrolyte concentration, and all three models for ion size predict values of zeta that are in good agreement with that predicted by the simple PB model. In addition, since the zeta potential for all models is below the critical zeta potential, ζ_c , at which ion sterics are expected to be important, this has the consequence of rendering ion steric effects negligible within the diffuse layer. Therefore, when the bulk concentration is large, the zeta potential is small and the total ion density in the diffuse layer is not much greater than in the bulk. This is seen in figures 5.7(c) and (d) which show that the structure of the equilibrium diffuse layer does not vary appreciably between the four models despite the rather large concentration of 1 M, where $\Phi^\infty = 0.201, 0.105,$ and $0.110,$ for Bik, CS, and BMCSL, respectively. In addition, the equilibrium ion densities in figure 5.7(c) are on the order of the bulk concentration and the phoretic mobility (5.29) and (5.33) only depends on the diffuse layer ion density relative to the bulk. Since EP depends only on the structure of the equilibrium diffuse layer, steric repulsion (ion size effects) does not effect electrophoretic mobility in this experimentally relevant scenario. Further, note that since the zeta potential decreases with increasing concentration, the EP mobility approaches zero at large concentrations.

However, figure 5.7(b) is a plot of the induced electric field versus concentration from DP. While the PB model predicts a constant value, the three models which account for the size of the ions predict an increasing electric field with increasing concentration. Physically, this is due to the steric repulsion between the ions as they diffuse down the concentration gradient, which as we showed in section 5.3.1, enhances the induced electric field.

Importantly, when $\zeta = 0$, there is no interaction potential between the colloid and the ions, and there will be no phoretic mobility (see figure 5.5). However, since $\zeta \propto \ln(1/\sqrt{c^\infty})$, there will always be a finite zeta potential since an electrolyte concentration has finite physical limits. In addition, while

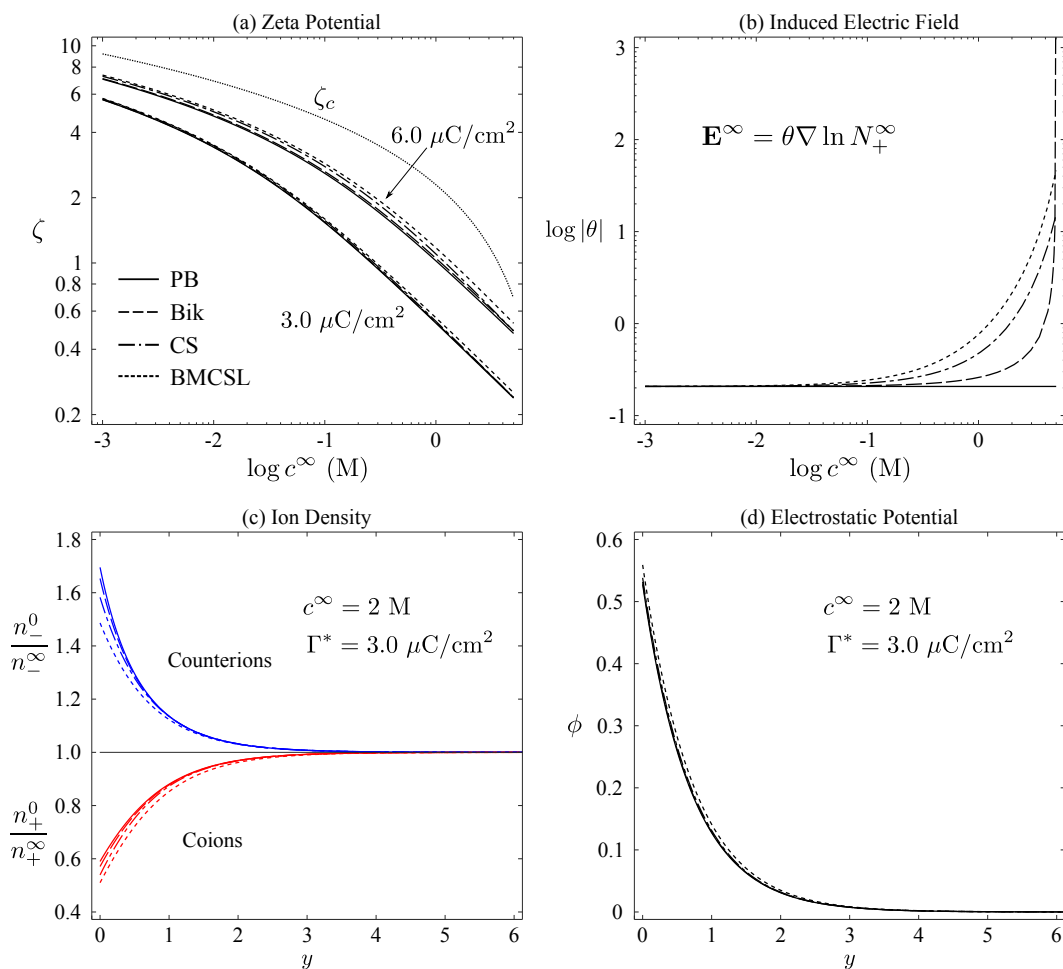


Figure 5.7: A colloid of constant surface charge density in a solution of NaCl. The zeta potential (a) calculated using the four models for surface charge densities of $\Gamma^* = 3$ and $6 \mu\text{C}/\text{cm}^2$. Also shown is the critical zeta potential, ζ_c ; above which ion steric effects are expected to be important. Despite slight deviation from the classic PB model result for $6 \mu\text{C}/\text{cm}^2$, all models predict zeta potentials below the critical value. The induced electric field (b) increases with increasing concentration in all models except the PB model which does not account for ion size. The rate at which the electric field increases is greater than the rate at which the zeta potential decreases. Figures (c) and (d) are for $\Gamma^* = 3 \mu\text{C}/\text{cm}^2$ and $c^\infty = 2 \text{ M}$. All four models predict essentially the same structure of the diffuse layer in terms of both the equilibrium ion densities (c) and the electrostatic potential (d) despite the large concentration.

the zeta potential, and hence the interaction potential, is a slowly decreasing logarithmic function of concentration, the induced electric field (via H_i^∞) is a rapidly increasing function of concentration. For example, from (5.6) and (5.12), $\mathbf{E}^\infty \propto 1/(1 - \Phi^\infty)^4$ for the CS model; recall that $\Phi^\infty \propto c^\infty$. Since the induced electric field increases more rapidly than the zeta potential decreases, the diffusiophoretic mobility is not only non-zero at large concentration but actually increases (figure 5.6(d)).

For both figures 5.6 and 5.7, the Bik model only goes up to a concentration of 4.03 M for KCl and 4.96 M for NaCl. This is due to assuming the ions take up a cubic volume and hence have a larger volume fraction than the CS and BMCSL models, which use ions with a spherical volume. For example, at $c^\infty = 5$ M for NaCl, the theoretical bulk volume fraction predicted by Bik is 1.007 while CS and BMCSL predict the bulk volume fraction to be 0.527 and 0.552, respectively.

5.6 Conclusion

We have derived a general equation for the diffusiophoretic and electrophoretic mobility of a single colloid in a binary electrolyte. To describe the electrolyte, we have utilized three different models which incorporate steric repulsion between finite sized ions into the governing equations, in addition to the classic Poisson-Boltzmann model for point-like, non-interacting ions. We show that the maximums in the mobility (with increasing zeta potential) for both diffusiophoresis and electrophoresis that are predicted by the Poisson-Boltzmann model are essentially eliminated by accounting for ion size. This is readily understood: the effect of ion sterics on the equilibrium diffuse layer is to reduce the counterion density relative to the Poisson-Boltzmann model. Since the maximum in mobility is due to a rapidly increasing surface conduction, the

reduced counterion density reduces the surface conduction and an opposing chemiosmotic (in electrophoresis) or electro-osmotic (in diffusiophoresis) flow does not develop. The mobility therefore does not undergo a maximum over realistic values for the zeta potential.

For a colloid with a constant surface charge density, a more relevant scenario for experiments, we show that, surprisingly, ion size effects are much more important for diffusiophoresis at high concentrations than for electrophoresis. This is because as the zeta potential decreases (and hence counterion density, relative to the bulk, decreases) with increasing concentration, steric repulsion between ions does not affect the structure of the diffuse layer for reasonable surface charge densities. However, steric repulsion within the highly concentrated bulk solution is non-negligible. Therefore, when there is an applied concentration gradient, as in diffusiophoresis (not electrophoresis), there exists an additional effect due to the size of the ions: a gradient in the excess electrochemical potential, which leads to an increase in the induced electric field with increasing concentration. Electrophoresis has no concentration gradient in the bulk solution and therefore has no excess electrochemical potential gradient. Therefore, since steric repulsion minimally affects the diffuse layer structure, the electrophoretic mobility is minimally affected by ion size effects (for zeta potentials resulting from a reasonable constant surface charge density).

Our predictions for diffusiophoresis are contrary to the common notion that the phoretic mobility approaches zero with increasing concentration due to a decreasing zeta potential [19]. While this notion holds for electrophoresis, for diffusiophoresis, it is only predicted by the Poisson-Boltzmann model. For any real electrolyte, for which the diffusivities are not equal, any model that includes steric repulsion between ions will predict an increase in the diffusiophoretic mobility with increasing concentration (see figure 5.6(d)). Hence, far

from becoming immobile, we predict that the mobility will actually increase greatly in concentrated electrolytes. Thus it may be that diffusiophoresis is an attractive transport mechanism in high salinity environments. Despite this increasing mobility with a decreasing zeta potential, when the zeta potential is exactly zero, the mobility is also zero (see figure 5.5). This is because there would no longer be an excess of ions surrounding the particle and therefore no slip velocity (see equation (5.26)).

Hence, the remarkable conclusion here is that to calculate the diffusiophoretic mobility of a spherical colloid, the classic Poisson-Boltzmann treatment of the electrolyte is sufficient to determine the ion profiles within the diffuse layer for reasonable surface charge densities. Then, including ion sterics within the bulk solution to derive the excess contribution to the induced electric field is straightforward by using an excess electrochemical potential. All that is required is a model for the the excess electrochemical potential and $\partial\mu_i^{\text{ex}}/\partial\Phi$ evaluated at the electroneutral solution concentration. These derivatives are provided in the appendix for the three models we considered.

In all of our results for diffusiophoresis, there is considerable dependence on which model is used to predict the mobility. This is simply due to the differences between how the models describe the ions. The Bikerman model assumes the ions occupy a regular lattice. The Carnahan-Starling and Boublik-Mansoori-Carnahan-Starling-Leland models are based on liquid-state theory for hard spheres, the latter being for a general case of different sized spheres while the former is for the special case of spheres of the same size. Our work in this chapter uses equations which are valid under the local density approximation (LDA). The equilibrium profiles calculated under this assumption are not always as accurate at high concentrations as methods based on density functional theory (DFT) or molecular simulations. However, these equilibrium profiles are only an intermediate step towards calculating the mobility.

Such integrated quantities (including capacitance) have been shown to agree well with DFT and molecular simulations [122, 123]. However, by using a fourth order Poisson equation which accounts for electrostatic correlations between ions, it has been shown that the equilibrium profiles can achieve better agreement with those from simulations, including local oscillations of charge density due to overscreening [22, 67]. This “modified-Poisson equation” has also been shown to predict electrophoretic mobility reversals in agreement with experiments in concentrated, multivalent electrolytes [43]. Incorporation of ion electrostatic correlation effects into diffusiophoresis is left for future work. Other effects in concentrated electrolytes include variations in the viscosity and permittivity [2]. As the electrolyte concentration increases, it is expected that the viscosity will also increase and the permittivity will decrease. Given this, it is possible that including these effects could reduce the large increase in diffusiophoretic mobility that we predict.

It should be noted that although our final equation for mobility (5.29) is independent of which model for the excess electrochemical potential is chosen to describe the electrolyte, it needs to be expressible as a function of the local (or bulk) volume fraction of ions only (i.e., $\mu_i^{\text{ex}} = \mu_i^{\text{ex}}(\Phi)$). As we show in the derivation, this is required to express $\nabla\mu_i^{\text{ex}}$ in terms of the applied gradient, $\nabla \ln N_+^\infty$. A consequence of this is that even though certain models used in DFT can be expressed as excess electrochemical potentials [122], they cannot be used in conjunction with our final equation (5.29). However, substitution of *any* excess electrochemical potential model into (5.11) is still possible, but derivation of a single final equation for the phoretic mobility - as we have done - would not readily follow.

Although we have considered the separate application of a concentration gradient and an electric field, the simultaneous action of both is a common situation in electrochemical cells and termed “electrodifusiophoresis” [139].

In such situations, reversals in particle migration direction can be brought about by altering the applied electrical current in addition to an appropriate selection of electrolyte and gradient strength. [139]. When both an electric field and concentration gradient are applied, the electrophoretic and diffusio-phoretic contributions to particle motion combine nonlinearly and the particle migration velocity increases in lower concentration regions due to an increase in the electric field in these regions. An interesting question then is whether ion sterics will increase the electric field in the high concentration region (as we predict) relative to the low concentration regions in electrodiffusiophoresis.

5.7 Appendix

5.7.1 Solution method for the equilibrium diffuse layer and excess electrochemical potential derivatives

To obtain the equilibrium profiles of ion density and electrostatic potential, we used MATLAB and a finite differencing scheme to solve Poisson's equation subject to the algebraic equations generated by the constraint of a constant electrochemical potential. In general, these equations are

$$\frac{d^2\phi}{dy^2} + (z_+n_+ + z_-n_-) = 0, \quad (5.42a)$$

$$z_i\phi + \ln n_i - \ln n_i^\infty + \mu_i^{\text{ex}} - \mu_i^{\text{ex},\infty} = 0, \quad (5.42b)$$

in terms of the local planar coordinate, $y = (r - 1)/\epsilon$ and where $i = +$ and $i = -$ for the cation and anion species, respectively. For the case of a specified zeta potential, we first use (5.42b) to obtain the ion densities at the surface, then apply both equations (5.42a) and (5.42b) to the remainder of the problem domain. Since both ϕ and n_i decay to a constant as $y \rightarrow \infty$, it is only necessary to include a finite distance. We used a domain of $y = [0, 20]$, which we tested

and found $y = 20$ to be sufficiently far from the surface that increases do not affect the results presented in the main text.

Once the equilibrium profiles are known, it is straightforward to evaluate the requisite integrals to obtain the mobility. However it is useful to include the expressions for the excess electrochemical potential gradients, H_i^∞ , for the three models we used; especially considering this is essentially all that is necessary to predict the effects of ion size on diffusiophoresis. Recall that $H_i^\infty = \Phi^\infty \partial \mu_i^{\text{ex}} / \partial \Phi^\infty$, where $\Phi^\infty = \sum_i N_i^\infty v_i$ is the volume fraction of ions in the bulk solution and N_i^∞ is the number density of ion species i .

The expressions for the excess electrochemical potential can be found in the text (5.5)-(5.7). The expressions for H_i^∞ are,

$$H_i^\infty = \begin{cases} \frac{\Phi^\infty}{1 - \Phi^\infty} & , \text{ for Bik} \\ \frac{2\Phi^\infty(4 - \Phi^\infty)}{(1 - \Phi^\infty)^4} & , \text{ for CS} \\ (T_{i,1} + T_{i,2} + T_{i,3} + T_{i,4}) \frac{1}{(\Phi^\infty)^2(1 - \Phi^\infty)^4} & , \text{ for BMCSL,} \end{cases} \quad (5.43a)$$

where

$$T_{i,1} = \left[1 + 2 \left(\frac{\xi_2^\infty a_i}{\Phi^\infty} \right)^3 - 3 \left(\frac{\xi_2^\infty a_i}{\Phi^\infty} \right)^2 \right] \left(\Phi^\infty (1 - \Phi^\infty) \right)^3, \quad (5.44a)$$

$$T_{i,2} = \left(3\xi_2^\infty a_i + 3\xi_1^\infty a_i^2 + \xi_0^\infty a_i^3 \right) \left(\Phi^\infty (1 - \Phi^\infty) \right)^2, \quad (5.44b)$$

$$T_{i,3} = 3\xi_2^\infty a_i^2 (\xi_2^\infty (1 + \Phi^\infty) + 2\Phi^\infty \xi_1^\infty a_i) \Phi^\infty (1 - \Phi^\infty), \quad (5.44c)$$

$$T_{i,4} = -2(\xi_2^\infty)^3 a_i^3 (1 - 3\Phi^\infty - (\Phi^\infty)^2), \quad (5.44d)$$

and $\xi_k^\infty = \sum_j N_j^\infty v_j a_j^{k-3}$.

5.7.2 Streamline equations for a general binary electrolyte

Here, we provide the equations for the perturbed electrostatic potential and salt concentration for the PB model for a general binary electrolyte. By taking appropriate linear combinations of the perturbed electrochemical potentials, we obtain

$$\phi^1 = \frac{\mu_+^1 - \mu_-^1}{z_+ - z_-} \quad (5.45a)$$

$$c^1 = \frac{2(z_- \mu_+^1 - z_+ \mu_-^1)}{z_+ z_- (z_+ - z_-)}. \quad (5.45b)$$

Substituting (5.27) for μ_i^1 and (5.17b) for the definition of G_i , we obtain

$$\phi^1 = \begin{cases} \left[-1 + \frac{\Delta_\phi C}{(z_+ - z_-) r^3} \right] \mathbf{V} \cdot \mathbf{r} & , \text{ for EP} \\ \left[-\beta^{\text{id}} + \frac{\Delta_\phi C}{(z_+ - z_-) r^3} \right] \mathbf{V} \cdot \mathbf{r} & , \text{ for DP} \end{cases} \quad (5.46a)$$

$$c^1 = \begin{cases} \frac{2\Delta_c C}{z_+(z_+ - z_-) r^3} \mathbf{V} \cdot \mathbf{r} & , \text{ for EP} \\ 2 \left[-\frac{1}{z_+ z_-} + \frac{\Delta_c C}{z_+(z_+ - z_-) r^3} \right] \mathbf{V} \cdot \mathbf{r} & , \text{ for DP} \end{cases} \quad (5.46b)$$

for any ζ , where $\Delta_\phi C = C_+ - C_-$ and $\Delta_c C = C_+ - z_+ C_- / z_-$ and C_i are given by (5.32). For large ζ with ϵ fixed (or equivalently, large Du), co-ions (co) are excluded from the diffuse layer so $\partial \mu_{\text{co}} / \partial r|_{r=1} = 0$ and the diffuse layer acts as a conductor of counterions (cnt) with $\nabla_s \mu_{\text{cnt}}|_{r=1} = 0$. This gives $C_{\text{co}} = G_{\text{co}}/2$

and $C_{\text{cnt}} = -G_{\text{cnt}}$ from (5.32). Substituting this into the above we obtain

$$\phi^1 = \begin{cases} -\beta^{\text{id}} \left(1 + \frac{z_{\text{co}} + 2z_{\text{cnt}}}{2(z_+ - z_-)r^3} \text{sgn}(\zeta) \right) \mathbf{V} \cdot \mathbf{r} & , \text{ for EP} \\ \left[-\beta^{\text{id}} \left(1 + \frac{z_{\text{co}} + 2z_{\text{cnt}}}{2(z_+ - z_-)r^3} \text{sgn}(\zeta) \right) + \frac{3\text{sgn}(\zeta)}{2(z_+ - z_-)r^3} \right] \mathbf{V} \cdot \mathbf{r} & , \text{ for DP} \end{cases} \quad (5.47a)$$

$$c^1 = \begin{cases} -\frac{3\text{sgn}(\zeta)}{(z_+ - z_-)r^3} \beta^{\text{id}} \mathbf{V} \cdot \mathbf{r} & , \text{ for EP} \\ 2 \left[-\frac{1}{z_+ z_-} \left(1 - \frac{2z_{\text{co}} + z_{\text{cnt}}}{2(z_+ - z_-)r^3} \text{sgn}(\zeta) \right) - \frac{3\text{sgn}(\zeta)}{2(z_+ - z_-)r^3} \beta^{\text{id}} \right] \mathbf{V} \cdot \mathbf{r} & , \text{ for DP.} \end{cases} \quad (5.47b)$$

For $z_+ = 1$ and $z_- = -1$, we obtain equations (5.36), (5.38), and (5.39).

Chapter 6

Conclusion

In this thesis, we have examined the dynamics of electrolyte solutions and colloidal particles immersed within them, in a variety of non-ideal conditions, from dilute solutions subjected to moderate voltages and temperature gradients, to highly concentrated solutions with ion-ion electrostatic and steric interactions. In every case, we have utilized continuum based models to describe the dynamics of the solution or a colloidal particle within it. These models have been analyzed with perturbation methods, and, where possible, direct comparisons to experiments have been attempted.

In chapter 2, we analyzed a simple electrochemical cell subjected to an AC voltage. While the linear response is well known and utilized experimentally to determine physical properties of the charge carriers via a technique called (linear) Electrochemical Impedance Spectroscopy (EIS) [29, 30], the response to voltages just outside the linear regime has not been explored. In order to extend this theory to moderate voltages, where the voltage magnitude, V_o , is on the order of the thermal voltage, $k_B T/e$, we expressed the governing equations as perturbations to the linear theory in terms of the dimensionless applied voltage magnitude, $\mathcal{V}_o = V_o/(k_B T/e)$. We discovered that at even orders of \mathcal{V}_o , there is no net charge motion within the cell; instead, neutral

salt is adsorbed into the diffuse layers. A significant result of this is that the only contributions to the current are from odd orders of \mathcal{V}_o . This salt adsorption leads to an increase in resistance within the cell which is predicted by an increase in the real part of the impedance. We considered only a binary, symmetric electrolyte in this chapter. Future work could consider asymmetric electrolytes in terms of charge number and diffusivities.

In chapter 3, we considered a similar cell, but instead of applying a voltage, we applied a temperature gradient across the device by heating one electrode. In response to the temperature gradient, the charge carriers migrate toward the cold electrode and induce an electric field or thermo-voltage as a result of unequal thermal migration. Our model system of a binary electrolyte represents the simplest possible thermo-electric device. In many respects, this problem is similar to that of a suddenly applied voltage to a previously undisturbed isothermal cell [59]. A primary difference is the timescale over which the diffuse layers charge. For a suddenly applied voltage, the timescale is the RC time, $L/D\kappa$, whereas for a thermo-electric cell, the thermo-voltage and diffuse layers charge on the Debye time, $1/D\kappa^2$. Since many experimental devices [13, 14, 15] are designed to operate in thin-diffuse-layer conditions, $\kappa L \gg 1$, this indicates that the thermo-voltage reaches steady-state relatively quickly compared to the case of a suddenly applied voltage. For example, a 1 mM aqueous solution will have $\kappa^{-1} \approx 10$ nm, then assuming $D = 10^{-5}$ cm²/s, a typical value for aqueous electrolytes [34], the Debye time is then $O(10^{-7}$ s), which is in stark contrast to the observed charging time scales of $O(100 - 1000)$ s in experiments [13, 14, 15]. Given this large discrepancy in charging times, we conclude that the heating rate of the electrodes is the limiting factor and thus suggest that efforts be made to optimize heat transfer to and from the electrodes. The second major finding in chapter 3 is that the steady-state concentration gradient across the cell develops on the diffusion time, L^2/D ,

a much longer timescale than the Debye time, which characterizes thermo-voltage evolution. This indicates that the majority of ion transport occurs after the thermo-voltage and diffuse layers have essentially reached steady state. Future work could include experiments to measure actual electrode temperature during heating to verify our predictions and development of models which include a time-dependent heating rate.

In chapter 4, we began our study of colloid mobility with electrophoresis, i.e., motion of a colloidal particle due to an applied electric field. Motivated by experimental observations that colloids in concentrated electrolyte solutions can move in the direction opposite that predicted by ideal solution theories [35, 36, 37, 38], we used a modified Poisson equation which accounts for direct ion-ion electrostatic interactions [22, 23, 24]. These electrostatic interactions occur within a local area surrounding each ion, over the length scale λ_c , the correlation length. We analyzed the model problem of a single colloidal particle with a low surface potential ($< k_B T/e$) and derived analytic equations for the mobility for both weak and strong correlations. For a colloid with a high surface potential ($> k_B T/e$), we accounted for the deformation of the diffuse charge layer surrounding the particle and used an asymptotic approach to consider the limit of thin diffuse layers, which is the regime where the reversals in mobility have been observed. We find that, in both low and high surface potential theories, electrostatic correlations are sufficient to predict electrophoretic mobility reversals. Although there is no predetermined value for λ_c and it is therefore essentially a fitting parameter, it must lie between the size of the ion and the Bjerrum length. Our results fall within this range.

In chapter 5, we studied diffusiophoresis, the motion of a colloidal particle due to an applied gradient in solute concentration [40, 41], in our case an electrolyte. We focus on non-ideal, concentrated solutions, where it becomes necessary to account for the finite size of the ions. We employed three different

models to incorporate steric repulsion between ions into the equations governing the electrolyte dynamics and ultimately derived an equation for the colloid mobility. We found that at high concentrations, the electric field induced by unequal ion migration increases rapidly with concentration for asymmetric electrolytes. This is due to the rapidly increasing steric repulsion in the large concentration region of the solution and a corresponding increase in a gradient of steric repulsion which acts to enhance the induced electric field. Since this electric field acts on the particle, the diffusiophoretic mobility increases with concentration, a rather surprising result. Future work should include measurements of the diffusion potential, the potential difference which results in the induced electric field. If the electric field does indeed increase with increasing concentration, then the measured diffusion potential should increase. It is expected from our results that a dilute solution theory would not be capable of predicting the observed diffusion potential increase.

There are several ways in which the work presented in this thesis could be improved by further research. For the thermo-electric analysis presented in chapter 2, relaxing the assumption of equal Brownian diffusivities could present a more accurate model of physical devices. In addition, some devices have a species which is relatively immobile [14], hence modeling a limiting case of only one mobile species could also offer critical insights into the charging dynamics of thermo-electric devices. For concentrated electrolyte solutions, we utilized modified PNP equations to describe the system dynamics, specifically the Nernst-Planck equations which consider the Brownian diffusivity of each charged species in isolation and use the average solution velocity as the velocity for each species. This is questionable for concentrated solutions where it becomes important to designate relative diffusivities, i.e., that species diffuse relative to one another. This can be described using Stefan-Maxwell fluxes which also account for the velocities of the individual species, including

the solvent [128]. These fluxes are considerably more mathematically complex than the Nernst-Planck equations, but offer a more accurate representation of the dynamics of non-ideal electrolyte solutions.

Bibliography

- [1] A. Ajdari, “Pumping liquids using asymmetric electrode arrays,” *Phys. Rev. E* **61**, R45 (2000).
- [2] M. Z. Bazant, M. S. Kilic, B. D. Storey, and A. Ajdari, “Towards an understanding of induced-charge electrokinetics at large applied voltages in concentrated solutions,” *Adv. Colloid Interfac.* **152**, 48 (2009).
- [3] N. A. Mishchuk, T. Heldal, T. Volden, J. Auerswald, and H. Knapp, “Microfluidic pump based on the phenomenon of electroosmosis of the second kind,” *Microfluid. Nanofluid.* **11**, 675 (2011).
- [4] C. C. Huang, M. Z. Bazant, and T. Thorsen, “Ultrafast high-pressure AC electro-osmotic pumps for portable biomedical microfluidics,” *Lab Chip* **10**, 80 (2010).
- [5] J. S. Paustian, A. J. Pascall, N. M. Wilson, and T. M. Squires, “Induced charge electroosmosis micropumps using arrays of Janus micropillars,” *Lab Chip* **14**, 3300 (2014).
- [6] H. D. Abruña, Y. Kiya, and J. C. Henderson, “Batteries and electrochemical capacitors,” *Phys. Today* **61**, 43 (2008).
- [7] R. Kötz and M. Carlen, “Principles and applications of electrochemical capacitors,” *Electrochim. Acta* **45**, 2483 (2000).

- [8] H. Keppner, S. Uhl, E. Laux, L. Jeandupeux, J. Tschanz, and T. Journot, "Ionic Liquid-based Thermoelectric Generator: Links between Liquid Data and Generator Characteristics," *Mater. Today: Proceedings*. **2**, 680 (2015).
- [9] M. Bonetti, S. Nakamae, B. T. Huang, T. J. Salez, C. Wiertel-Gasquet, and M. Roger, "Thermoelectric energy recovery at ionic-liquid/electrode interface," *J. Chem. Phys.* **142**, 244708 (2015).
- [10] T. J. Abraham, D. R. MacFarlane, and J. M. Pringle, "Seebeck coefficients in ionic liquids -prospects for thermo-electrochemical cells," *Chem. Commun.* **47**, 6260 (2011).
- [11] O. Bubnova, Z. U. Khan, A. Malti, S. Braun, M. Fahlman, M. Berggren, and X. Crispin, "Optimization of the thermoelectric figure of merit in the conducting polymer poly(3,4-ethylenedioxythiophene)," *Nat. Mater.* **10**, 429 (2011).
- [12] Y. Xuan, X. Liu, S. Desbief, P. Leclère, M. Fahlman, R. Lazzaroni, M. Berggren, J. Cornil, D. Emin, and X. Crispin, "Thermoelectric properties of conducting polymers: The case of poly(3-hexylthiophene)," *Phys. Rev. B* **82**, 115454 (2010).
- [13] W. B. Chang, H. Fang, J. Liu, C. M. Evans, B. Russ, B. C. Popere, S. N. Patel, M. L. Chabinyk, and R. A. Segalman, "Electrochemical Effects in Thermoelectric Polymers," *ACS Macro Lett.* **5**, 455 (2016).
- [14] S. L. Kim, H. T. Lin, and C. Yu, "Thermally Chargeable Solid-State Supercapacitor," *Adv. Energy Mater.* **6**, 1600546 (2016).

- [15] D. Zhao, H. Wang, Z. U. Khan, J. C. Chen, R. Gabrielsson, M. P. Jons-son, M. Berggren, and X. Crispin, “Ionic thermoelectric supercapacitors,” *Energy Environ. Sci.* **9**, 1450 (2016).
- [16] H. G. Bagaria, Z. Xue, B. M. Neilson, A. J. Worthen, K. Y. Yoon, S. Nayak, V. Cheng, J. H. Lee, C. W. Bielawski, and K. P. Johnston, “Iron Oxide Nanoparticles Grafted with Sulfonated Copolymers are Stable in Concentrated Brine at Elevated Temperatures and Weakly Adsorb on Silica,” *ACS Appl. Mater. Interfaces* **5**, 3329 (2013).
- [17] A. Lager, K. J. Webb, I. R. Collins, and D. M. Richmond, “LoSal Enhanced Oil Recovery: Evidence of Enhanced Oil Recovery at the Reser-voir Scale,” *SPE Symposium on Improved Oil Recovery*, Tulsa, OK, USA (2008).
- [18] D. Velegol, A. Garg, R. Guha, A. Kar, and M. Kumar, “Origins of con-centration gradients for diffusiophoresis,” *Soft Matter.* **12**, 4686 (2016).
- [19] W. B. Russel, D. A. Saville, and W. R. Schowalter, *Colloidal Dispersions* (Cambridge University Press, 1989).
- [20] G. Guthrie, J. N. Wilson, and V. Schomaker, “Theory of the Thermal Diffusion of Electrolytes in a Clusius Column,” *J. Chem. Phys.* **17**, 310 (1949).
- [21] J. Newman, “Thermoelectric Effects in Electrochemical Systems,” *Ind. Eng. Chem. Res.* **34**, 3208 (1995).
- [22] B. D. Storey and M. Z. Bazant, “Effects of electrostatic correlations on electrokinetic phenomena,” *Phys. Rev. E* **86**, 056303 (2012).
- [23] C. D. Santangelo, “Computing counterion densities at intermediate cou-pling,” *Phys. Rev. E* **73**, 041512 (2006).

- [24] M. M. Hatlo and L. Lue, “Electrostatic interactions of charged bodies from the weak- to the strong-coupling regime,” *Europhys. Lett.* **89**, 25002 (2010).
- [25] M. Mezger, H. Schröder, H. Reichert, S. Schramm, J. S. Okasinski, S. Schöder, V. Honkimäki, M. Deutsch, B. M. Ocko, J. Ralston, M. Rohwender, M. Stratmann, and H. Dosch, “Molecular Layering of Fluorinated Ionic Liquids at a Charged Sapphire (0001) Surface,” *Science*, **322**, 424 (2008).
- [26] M. S. Kilic, M. Z. Bazant, and A. Ajdari, “Steric effects in the dynamics of electrolytes at large applied voltages. I. Double-layer charging,” *Phys. Rev. E* **75**, 021502 (2007).
- [27] M. S. Kilic, M. Z. Bazant, and A. Ajdari, “Steric effects in the dynamics of electrolytes at large applied voltages. II. Modified Poisson-Nernst-Planck equations,” *Phys. Rev. E* **75**, 021503 (2007).
- [28] A. S. Khair and T. M. Squires, “Ion steric effects on electrophoresis of a colloidal particle,” *J. Fluid Mech.* **640**, 343 (2009).
- [29] A. Lasia, *Electrochemical Impedance Spectroscopy and its Applications*, (Springer, 2014).
- [30] B. A. Yezer, A. S. Khair, P. J. Sides, and D. C. Prieve, “Use of electrochemical impedance spectroscopy to determine double-layer capacitance in doped nonpolar liquids,” *J. Colloid Interf. Sci.* **449**, 2 (2015).
- [31] C. B. Vining, “An inconvenient truth about thermoelectrics,” *Nat. Mater.* **8**, 83 (2009).
- [32] A. Majee and A. Würger, “Collective thermoelectrophoresis of charged colloids,” *Phys. Rev. E* **83**, 061403 (2011).

- [33] S. A. Putnam and D. G. Cahill, "Transport of Nanoscale Latex Spheres in a Temperature Gradient," *Langmuir* **21**, 5317 (2005).
- [34] I. D. Zaytsev and G. G. Aseyev, in *Properties of Aqueous Solutions of Electrolytes*, translated by M. A. Lazarev and V. R. Sorochenko (CRC Press, 1992).
- [35] I. Semenov, S. Raafatnia, M. Sega, V. Lobaskin, C. Holm, and F. Kremer, "Electrophoretic mobility and charge inversion of a colloidal particle studied by single-colloid electrophoresis and molecular dynamics simulations," *Phys. Rev. E* **87**, 022302 (2013).
- [36] U. P. Strauss, N. L. Gershfeld, and H. Spiera, "Charge Reversal of Cationic Poly-4-vinylpyridine Derivatives in KBr Solutions," *J. Am. Chem. Soc.* **76**, 5909 (1954).
- [37] A. Martín-Molina, C. Rodríguez-Beas, R. Hidalgo-Álvarez, and M. Quesada-Pérez, "Effect of Surface Charge on Colloidal Charge Reversal," *J. Phys. Chem. B* **113**, 6834 (2009).
- [38] M. Elimelech and C. R. O'Melia, "Effect of electrolyte type on the electrophoretic mobility of polystyrene latex colloids," *Colloids and Surfaces* **44**, 165 (1990).
- [39] S. Raafatnia, O. A. Hickey, M. Sega, and C. Holm, "Computing the Electrophoretic Mobility of Large Spherical Colloids by Combining Explicit Ion Simulations with the Standard Electrokinetic Model," *Langmuir* **30**, 1758 (2014).
- [40] D. C. Prieve, J. L. Anderson, J. P. Ebel, and M. E. Lowell, "Motion of a particle generated by chemical gradients. Part 2. Electrolytes," *J. Fluid Mech.* **148**, 247 (1984).

- [41] M. M. -J. Lin and D. C. Prieve, “Electromigration of latex induced by a salt gradient,” *J. Coll. Inter. Sci.* **95**, 327 (1983).
- [42] R. F. Stout and A. S. Khair, “Moderately nonlinear diffuse-charge dynamics under an ac voltage,” *Phys. Rev. E* **92**, 032305 (2015).
- [43] R. F. Stout and A. S. Khair, “A continuum approach to predicting electrophoretic mobility reversals,” *J. Fluid Mech.* **752**, R1 (2014).
- [44] R. F. Stout and A. S. Khair, “Influence of ion sterics on diffusiophoresis and electrophoresis in concentrated electrolytes,” *Phys. Rev. Fluids* **2**, 014201 (2017).
- [45] A. Mani and M. Z. Bazant, “Deionization shocks in microstructures,” *Phys. Rev. E* **84**, 061504 (2011).
- [46] Y. Oren, “Capacitive deionization (CDI) for desalination and water treatment - past, present and future (a review),” *Desalination* **228**, 10 (2008).
- [47] P. M. Biesheuvel and M. Z. Bazant, “Nonlinear dynamics of capacitive charging and desalination by porous electrodes,” *Phys. Rev. E* **81**, 031502 (2010).
- [48] M. E. Suss, T. F. Baumann, W. L. Bourcier, C. M. Spadaccini, K. A. Rose, J. G. Santiago, and M. Stadermann, “Capacitive desalination with flow-through electrodes,” *Energy Environ. Sci.* **5**, 9511 (2012).
- [49] T. M. Squires and S. R. Quake, “Microfluidics: Fluid physics at the nanoliter scale,” *Rev. Mod. Phys.* **77**, 977 (2005).
- [50] T. M. Squires and M. Z. Bazant, “Induced-charge electro-osmosis,” *J. Fluid Mech.* **509**, 217 (2004).

- [51] J. A. Levitan, S. Devasenathipathy, V. Studer, Y. Ben, T. Thorsen, T. M. Squires, and M. Z. Bazant, “Experimental observation of induced-charge electro-osmosis around a metal wire in a microchannel,” *Colloids Surf. A* **267**, 122 (2005).
- [52] A. Ramos, H. Morgan, N. G. Green, A. González, and A. Castellanos, “Pumping of liquids with traveling-wave electroosmosis,” *J. Appl. Phys.* **97**, 084906 (2005).
- [53] M. Z. Bazant and T. M. Squires, “Induced-Charge Electrokinetic Phenomena: Theory and Microfluidic Applications,” *Phys. Rev. Lett.* **92**, 066101 (2004).
- [54] T. M. Squires and M. Z. Bazant, “Breaking symmetries in induced-charge electro-osmosis and electrophoresis,” *J. Fluid Mech.* **560**, 65 (2006).
- [55] M. Mittal, P. P. Lele, E. W. Kaler, and E. M. Furst, “Polarization and interactions of colloidal particles in ac electric fields,” *J. Chem. Phys.* **129**, 064513 (2008).
- [56] D. C. Prieve, P. J. Sides, and C. L. Wirth, “2-D assembly of colloidal particles on a planar electrode,” *Curr. Opin. Colloid Interface Sci.* **15**, 160 (2010).
- [57] P. K. Wong, T. H. Wang, J. H. Deval, and C. M. Ho, “Electrokinetics in micro devices for biotechnology applications,” *IEEE/ASME Trans. Mechatron.* **9**, 366 (2004).
- [58] J. Voldman, “ELECTRICAL FORCES FOR MICROSCALE CELL MANIPULATION,” *Annu. Rev. Biomed. Eng.* **8**, 425 (2006).
- [59] M. Z. Bazant, K. Thornton, and A. Ajdari, “Diffuse-charge dynamics in electrochemical systems,” *Phys. Rev. E* **70**, 021506 (2004).

- [60] J. Lyklema, *Fundamentals of Interface and Colloid Science. Volume II: Solid-Liquid Interfaces* (Academic Press, 1995).
- [61] F. C. M. Freire, G. Barbero, and M. Scalerandi, “Electrical impedance for an electrolytic cell,” *Phys. Rev. E* **73**, 051202 (2006).
- [62] O. Schnitzer and E. Yariv, “Nonlinear oscillations in an electrolyte solution under ac voltage,” *Phys. Rev. E* **89**, 032302 (2014).
- [63] L. H. Olesen, M. Z. Bazant, and H. Bruus, “Strongly nonlinear dynamics of electrolytes in large ac voltages,” *Phys. Rev. E* **82**, 011501 (2010).
- [64] L. Fan, Y. Liu, J. Xiong, H. S. White, and S. Chen, “Electron-Transfer Kinetics and Electric Double Layer Effects in Nanometer-Wide Thin-Layer Cells,” *ACS Nano* **8**, 10426 (2014).
- [65] A. Bandopadhyay, V. A. Shaik, and S. Chakraborty, “Effects of finite ionic size and solvent polarization on the dynamics of electrolytes probed through harmonic disturbances,” *Phys. Rev. E* **91**, 042307 (2015).
- [66] R. H. Ewoldt, A. E. Hosoi, and G. H. McKinley, “New measures for characterizing nonlinear viscoelasticity in large amplitude oscillatory shear,” *J. Rheol.* **52**, 1427 (2008).
- [67] M. Z. Bazant, B. D. Storey, and A. A. Kornyshev, “Double Layer in Ionic Liquids: Overscreening versus Crowding,” *Phys. Rev. Lett.* **106**, 046102 (2011).
- [68] S. Duhr and D. Braun, “Why molecules move along a temperature gradient,” *P. Natl. Acad. Sci. USA.* **103**, 19678 (2006).
- [69] H. S. Kim, W. Liu, G. Chen, C. W. Chu, and Z. Ren, “Relationship between thermoelectric figure of merit and energy conversion efficiency,” *Proc. Natl. Acad. Sci.* **112**, 8205 (2015).

- [70] L. E. Bell, "Cooling, Heating, Generating Power, and Recovering Waste Heat with Thermoelectric Systems," *Science* **321**, 1457 (2008).
- [71] A. P. Gonçalves, E. B. Lopes, E. Alves, N. P. Barradas, N. Franco, O. Rouleau, and C. Godart, "New Approaches to Thermoelectric Materials," in *Properties and Applications of Thermoelectric Materials*, edited by V. Zlatic and A. C. Hewson (Springer, 2009).
- [72] W. Fulkerson, J. P. Moore, R. K. Williams, R. S. Graves, and D. L. McElroy, "Thermal Conductivity, Electrical Resistivity, and Seebeck Coefficient of Silicon from 100 to 1300K," *Phys. Rev.* **167**, 765 (1968).
- [73] Y. He, T. Day, T. Zhang, H. Liu, X. Shi, L. Chen, and G. J. Snyder, "High Thermoelectric Performance in Non-Toxic Earth-Abundant Copper Sulfide," *Ad. Mater.* **26**, 3974 (2014).
- [74] M. Bonetti, S. Nakamae, M. Roger, and P. Guenoun, "Huge Seebeck coefficients in nonaqueous electrolytes," *J. Chem. Phys.* **134**, 114513 (2011).
- [75] J. L. Duda, "Molecular diffusion in polymeric systems," *Pure and Appl. Chem.* **57**, 1681 (1985).
- [76] Numeric Laplace transform inversion was performed using the MATLAB function, "INVLAP.m" by Mathworks.
- [77] A. A. Elbashir and H. Y. Aboul-Enein, "Capillary electrophoresis and molecular modeling as a complementary technique for chiral recognition mechanism," *Crit. Rev. Anal. Chem.* **43**, 131 (2013).
- [78] K. D. Dorfman, "DNA electrophoresis in microfabricated devices," *Rev. Mod. Phys.* **82**, 2903 (2010).

- [79] M. von Smoluchowski, "Contribution à la théorie de l'endosmose électrique et de quelques phénomènes corrélatifs," *Bull. Inter. Acad. Sci. Cracovie* **8**, 182 (1903).
- [80] E. Hückel, "Die kataphorese der kugel," *Phys. Z* **25**, 204 (1924).
- [81] D. C. Henry, "The cataphoresis of suspended particles. Part I. The equation of cataphoresis," *P. Roy. Soc. Lond. A Mat.* **133**, 106 (1931).
- [82] R. W. O'Brien and L. R. White, "Electrophoretic mobility of a spherical colloid," *J. Chem. Soc. Farad. T. 2* **74**, 1607 (1978).
- [83] S. S. Dukhin and B. V. Deryaguin, "Electrokinetic phenomena," in *Encyclopedia of Surface and Colloid Science* 7, ser. ed. E. Matijevic. (Wiley, 1974).
- [84] R. W. O'Brien, "The solution of the electrokinetic equations for colloidal particles with thin double layers," *J. Colloid. Interf. Sci.* **92**, 204 (1983).
- [85] O. Schnitzer and E. Yariv, "Macroscale description of electrokinetic flows at large zeta potentials: Nonlinear surface conduction," *Phys. Rev. E* **86**, 021503 (2012).
- [86] J. J. Bikerman, "XXXIX. Structure and capacity of electrical double layer," *Phil. Mag.* **33**, 384 (1942).
- [87] A. Martín-Molina, M. Quesada-Pérez, F. Galisteo-González, and R. Hidalgo-Álvarez, "Looking into overcharging in model colloids through electrophoresis: Asymmetric electrolytes," *J. Chem. Phys.* **118**, 4183 (2003).
- [88] M. Quesada-Pérez, E. González-Tovar, A. Martín-Molina, M. Lozada-Cassou, R. Hidalgo-Álvarez, "Ion size correlations and charge reversal in real colloids," *Colloid Surface A* **267**, 24 (2005).

- [89] A. Y. Grosberg, T. T. Nguyen, and B. I. Shklovskii, "Colloquium: The physics of charge inversion in chemical and biological systems," *Rev. Mod. Phys.* **74**, 329 (2002).
- [90] Y. Levin, "Electrostatic correlations: from plasma to biology," *Rep. Prog. Phys.* **65**, 1577 (2002).
- [91] G. M. Torrie and J. P. Valleau, "Electrical double layers. I. Monte Carlo study of a uniformly charged surface," *J. Chem. Phys.* **73**, 5807 (1980).
- [92] M. V. Fedorov and A. A. Kornyshev, "Ionic liquid near a charged wall: Structure and capacitance of the electrical double-layer," *J. Phys. Chem. B* **112**, 11868 (2008).
- [93] E. Gonzales-Tovar, M. Lozada-Cassou, and D. Henderson, "Hypernetted chain approximation for the distribution of ions around a cylindrical electrode. II. Numerical solution for a model cylindrical polyelectrolyte," *J. Chem. Phys.* **83**, 361 (1985).
- [94] P. Attard, D. J. Mitchell, and B. W. Ninham, "Beyond Poisson-Boltzmann: Images and correlations in the electric double layer. I. Counterions only," *J. Chem. Phys.* **88**, 4987 (1988).
- [95] J. Ennis, S. Marcelja, and R. Kjellander, "Effective surface charge for symmetric electrolytes in the primitive model double layer," *Electrochimica Acta* **41**, 2115 (1996).
- [96] R. Kjellander and S. Marcelja, "Double-layer interaction in the primitive model and the corresponding Poisson-Boltzmann description," *J. Phys. Chem.* **90**, 1230 (1986).

- [97] D. Gillespie, A. S. Khair, J. P. Bardhan, and S. Pennathur, “Efficiently accounting for ion correlations in electrokinetic nanofluidic devices using density functional theory,” *J. Colloid Interf. Sci.* **359**, 520 (2011).
- [98] R. R. Netz and H. Orland, “Beyond Poisson Boltzmann: Fluctuation effects and correlation functions,” *Eur. Phys. J. E.* **1**, 203 (2000).
- [99] A. Martín-Molina, J. A. Maroto-Centeno, R. Hidalgo-Alvarez, and M. Quesada-Pérez, “Charge reversal in real colloids: Experiments, theory and simulations,” *Colloid. Surface. A* **319**, 103 (2008).
- [100] M. Lozada-Cassou, E. González-Tovar, and W. Olivares, “Nonlinear effects in the electrophoresis of a spherical colloidal particle,” *Phys. Rev. E* **60**, R17 (1999).
- [101] M. Z. Bazant, B. D. Storey, and A. A. Kornyshev, “Erratum: Double layer in ionic liquids: Overscreening versus crowding,” *Phys. Rev. Lett.* **109**, 149903 (2012).
- [102] S. Kim and S. J. Karrila, *Microhydrodynamics: Principles and Selected Applications* (Dover, 2005).
- [103] H. Ohtaki and T. Radnai, “Structure and dynamics of hydrated ions,” *Chem. Rev.* **93**, 1157 (1993).
- [104] P. Vanýsek, in *CRC Handbook of Chemistry and Physics* Ed. 93, editor W. M. Hayes. 5-77 (CRC Press, 2012).
- [105] M. M. Hatlo, R. van Roij, and L. Lue, “The electric double layer at high surface potentials: The influence of excess ion polarizability,” *Europhys. Lett.* **89**, 28010 (2012).

- [106] J. L. Anderson, M. E. Lowell, and D. C. Prieve, "Motion of a particle generated by chemical gradients. Part 1. Non-electrolytes," *J. Fluid Mech.* **117**, 107 (1982).
- [107] B. V. Derjaguin, G. P. Sidorenkov, E. A. Zubashchenkov, and E. V. Kiseleva, "Kinetic phenomena in boundary films of liquids," *Kolloidn. Zh.* **9**, 335 (1947).
- [108] J. S. Paustian, C. D. Angulo, R. Nery-Azevedo, N. Shi, A. I. Abdel-Fattah, and T. M. Squires, "Direct Measurements of Colloidal Solvophoresis under Imposed Solvent and Solute Gradients," *Langmuir*, **31**, 4402 (2015).
- [109] J. L. Anderson and D. C. Prieve, "Diffusiophoresis caused by gradients of strongly adsorbing solutes," *Langmuir*. **7**, 403 (1991).
- [110] N. Sharifi-Mood, J. Koplik, and C. Maldarelli, "Molecular Dynamics Simulation of the Motion of Colloidal Nanoparticles in a Solute Concentration Gradient and a Comparison to the Continuum Limit," *Phys. Rev. Lett.* **111**, 184501 (2013).
- [111] N. Sharifi-Mood, J. Koplik, and C. Maldarelli, "Diffusiophoretic self-propulsion of colloids driven by a surface reaction: The sub-micron particle regime for exponential and van der Waals interactions," *Phys. Fluids*. **25**, 012001 (2013).
- [112] R. Guha, X. Shang, A. L. Zydney, D. Velegol, and M. Kumar, "Diffusiophoresis contributes significantly to colloidal fouling in low salinity reverse osmosis systems," *J. Membrane Sci.* **479**, 67 (2015).

- [113] A. Kar, R. Guha, N. Dani, D. Velegol, and M. Kumar, "Particle Deposition on Microporous Membranes Can Be Enhanced or Reduced by Salt Gradients," *Langmuir*. **30**, 793 (2014).
- [114] A. Kar, T. Chiang, I. O. Rivera, A. Sen, and D. Velegol, "Enhanced Transport into and out of Dead-End Pores," *ACS Nano* **9**, 746 (2015).
- [115] B. Abécassis, C. Cottin-Bizonne, C. Ybert, A. Ajdari, and L. Bocquet, "Boosting migration of large particles by solute contrasts," *Nat. Mater.* **7**, 785 (2008).
- [116] V. Yadav, J. D. Freedman, M. Grinstaff, and A. Sen, "Bone-Crack Detection, Targeting, and Repair Using Ion Gradients," *Angew. Chem. - Int. Ed.* **52**, 10997 (2013).
- [117] V. Yadav, R. A. Pavlick, S. M. Meckler, and A. Sen, "Triggered Detection and Deposition: Toward the Repair of Microcracks," *Chem. Mater.* **26**, 4647 (2014).
- [118] B. E. Logan and M. Elimelech, "Membrane-based processes for sustainable power generation using water," *Nature*. **488**, 313 (2012).
- [119] P. M. Biesheuvel and M. van Soestbergen, "Counterion volume effects in mixed electrical double layers," *J. Colloid Inter. Sci.* **316**, 490 (2007).
- [120] M. Manciu and E. Ruckenstein, "Lattice Site Exclusion Effect on the Double Layer Interaction," *Langmuir*. **18**, 5178 (2002).
- [121] N. F. Carnahan and K. E. Starling, "Equation of State for Nonattracting Rigid Spheres," *J. Chem. Phys.* **51**, 635 (1969).
- [122] D. Gillespie, "A review of steric interactions of ions: Why some theories succeed and others fail to account for ion size," *Microfluid Nanofluid*, **18**, 717 (2015).

- [123] B. Giera, N. Henson, E. M. Kober, M. S. Shell, and T. M. Squires, “Electric Double-Layer Structure in Primitive Model Electrolytes: Comparing Molecular Dynamics with Local-Density Approximations,” *Langmuir*, **31**, 3553 (2015).
- [124] R. W. O’Brien and L. R. White, Electrophoretic mobility of a spherical colloidal particle, *J. Chem. Soc. Faraday Trans.* **74**, 1607 (1978).
- [125] A. S. Khair and T. M. Squires, “The influence of hydrodynamic slip on the electrophoretic mobility of a spherical colloidal particle,” *Phys. Fluids*. **21**, 042001 (2009).
- [126] T. Boublik, “Hard-Sphere Equation of State,” *J. Chem. Phys.* **53**, 471 (1970).
- [127] G. A. Mansoori, N. F. Carnahan, K. E. Starling, and T. W. Leland, “Equilibrium Thermodynamic Properties of the Mixture of Hard Spheres,” *J. Chem. Phys.* **54**, 1523 (1971).
- [128] J. Newman and K. E. Thomas-Alyea, *Electrochemical Systems* (Wiley, 2004).
- [129] T. Chiang and D. Velegol, “Multi-ion diffusiophoresis”, *J. Coll. Inter. Sci.* **424**, 120 (2014).
- [130] O. Schnitzer and E. Yariv, “Strong-field electrophoresis,” *J. Fluid Mech.* **701**, 333 (2012).
- [131] E. Yariv, “An Asymptotic Derivation of the Thin-Debye-Layer Limit for Electrokinetic Phenomena,” *Chem. Eng. Comm.* **197**, 3 (2009).
- [132] J. L. Anderson, “Colloid Transport by Interfacial Forces,” *Annu. Rev. Fluid Mech.* **21**, 61 (1989).

- [133] M. Flury and T. F. Gimmi, Solute Diffusion, in *Methods of Soil Analysis, Part 4, Physical Methods*, edited by J. H. Dane and G. C. Topp, 1323, (Soil Science Society of America, 2002).
- [134] T. R. Ferguson and M. Z. Bazant, “Nonequilibrium Thermodynamics of Porus Electrodes,” *J. Electrochem. Soc.* **159**, A1967 (2012).
- [135] H. Ohshima, “Limiting electrophoretic mobility of a highly charged soft particle in an electrolyte solution: Solidification effect,” *J. Coll. Inter. Sci.* **349**, 641 (2010).
- [136] J. C. Berg, *An Introduction to Interfaces and Colloids, The Bridge to Nanoscience* (World Scientific Publishing Co. Pte. Ltd. 2010).
- [137] M. Kosmulski, “Electric Charge Density of Silica, Alumina, and Related Surfaces,” in *Encyclopedia of Surface and Colloid Science, Volume 3*, 2nd edition, edited by P. Somasundaran, (Taylor and Francis Group, 2006).
- [138] S. -L. Tsaur and R. M. Fitch, “Preparation and properties of polystyrene model colloids: II. Effect of surface charge density on coagulation behavior,” *J. Coll. Inter. Sci.* **115**, 463 (1987).
- [139] R. A. Rica and M. Z. Bazant, “Electrodifusiophoresis: Particle motion in electrolytes under direct current,” *Phys. Fluids.* **22**, 112109 (2010).